



UNIVERSITÉ DE STRASBOURG



ÉCOLE DOCTORALE DES SCIENCES DE LA VIE ET DE LA SANTÉ
INSTITUT DE GÉNÉTIQUE ET DE BIOLOGIE MOLÉCULAIRE ET CELLULAIRE
CNRS (UMR 7104) | INSERM (U 964)

THÈSE présentée par :

Salvatore TERROSU

soutenue le : **12 décembre 2022**

pour obtenir le grade de : **Docteur de l'Université de Strasbourg**

Discipline/ Spécialité : **Biologie structurale et biophysique**

Structural and Biophysical characterization of small molecules binding to the Ribosome as a potential anticancer treatment

THÈSE dirigée par :

Dr. YUSUPOV Marat

Directeur de recherche, Université de Strasbourg

RAPPORTEURS :

Pr. SCHMITT Emmanuelle

Directeur de recherche, École polytechnique (Paris)

Pr. GUSKOV Albert

Directeur de recherche, University of Groningen

AUTRES MEMBRES DU JURY :

Dr. LAMOUR Valérie

MCU-PH, IGMBC - Hôpitaux Universitaires de Strasbourg

Acknowledgements

First things first. I would like to thank my jury members, **Pr. Emmanuelle Schmitt**, **Pr. Albert Guskov** and **Dr. Valerie Lamour** for finding time to evaluate and comment my PhD dissertation, in addition I would like to address a particular thank you to **Pr. Benoit Masquida** for being part of my follow-up committee during these years. To my Thesis Supervisor, **Dr. Marat Yusupov**: it is been an honor working under your supervision. Thanks a lot for the trust you showed giving me interesting and challenging projects, I am really grateful. To **Dr. Gulnara Yusupova**, I would like to express my gratitude for the precious advices and for the long discussions about science and not only. To **Dr. Simone Pellegrino**, the first person to introduce me to the fantastic world of ribosome purification and crystallization, and then to the universe of small molecules! I will never forget it. To **Dr. Lasse Bohl Jenner** and **Dr. Alexey Rozov**, thanks for the advices and direction you have been giving during this long journey! I want to express my gratitude to all members of the IGBMC-CBI-BSI platforms for their priceless help in the solution of technical problems and particular issues, everything but not simple to solve. **Dr. Corinne Crucifix** for her patience introducing a “crystallographer” to the world of cryo-electron microscopy. I want to thank as well **Dr. Alexandre Duran**, **Dr. Nils Marechal** and **Dr. Catherine Birk** for the patience shown every time I had a question, and I had a lot! **Dr. Luc Negroni** and **Bastien Morlet**, from the IGBMC proteomic platform goes all my gratitude for their precious contribution. A big thank you to **Dr. Muriel Rhinn** that showed me how to handle a chick embryo during the last part of my PhD, it would have definitely impossible without you. Together with all these people inside the IGBMC I must acknowledge also all staff from the Synchrotron beamlines I used during these four years, **Dr Takashi Tomizaki** from the Swiss Light Source, **Dr Leonard Chavas** from Soleil Synchrotron and last but not least **Dr Daniele De Sanctis** from ESRF. I would like also to thank all the people for the Dubochet Centre of Imaging, in the person of **Dr. Alexander Myasnikov**. A very big thank you everyone that collaborated in this project: **Pr. Christopher VanderWal** and all his lab, **Dr. Gregory Challis** and **Pr. Denis Lafontaine** for providing high quality material for structural studies along with their precious advices and fruitful suggestions.

How to forget all members, actual and former, of the Yusupov Lab: **Yury, Olga, Alexander, Justine, Margarita, Muminjon, Liliia and Bulat**, thank you for all the time spent together. A special thank you to Liliia for being with me all the time during this “chicken adventure”, it has been a lot of fun!!!

Nemanja, I think there are no words in the languages I know for expressing how this journey would have been different without you. Thanks for all moments, for all coffees and the extra food; for all the advices and all the support you have been restlessly giving to me, I will never thank you enough for being there in the darkest and in the brightest moments!

I would also like to thank all the people that during these four years have been there: **To the Student and Post-Doc Board** association goes my warm thank for everything we did together. Only thinking about everything we have been able to do thanks to our tenancy, it makes me smile.

To my family, always supportive and ready to help when help was needed, I love you to the Moon and Back.

To all my friends, the new ones and the old ones for being with me during these four years. I will not mention you all, it will be an incredibly long list and there is a full manuscript to read, so be kind!

To the love of my life, the real hero of this story. Thanks for shaking me when it was needed and for holding me when I was falling, it meant everything to me.

« Nihil sapiens affirmat quod non probet »

Résumé

Du plus petit organisme procaryote aux plus grands eucaryotes comme la baleine à bosse géante, la synthèse des protéines joue un rôle vital dans tous les domaines de la vie. Le ribosome est l'acteur principal de ce processus. Cette énorme machinerie ribonucléoprotéique lit le code génétique, sous forme d'ARN messager, pour synthétiser les protéines au cours d'un processus finement régulé appelé traduction. La taille des ribosomes varie de 2,5 MDa chez les procaryotes à 4,3 MDa chez les eucaryotes supérieurs. Trois types d'ARN ribosomique (ARNr) et 54 protéines ribosomiques (PR) composent le ribosome 70S bactérien. Les ribosomes eucaryotes sont en revanche des machineries beaucoup plus complexes, car leur taille varie au sein du domaine eucaryote. Par exemple, les ribosomes de *Saccharomyces cerevisiae* sont constitués de 4 types d'ARNr et de 79 PR pour une taille de 3,3 MDa, tandis que les ribosomes animaux et végétaux contiennent des ensembles supplémentaires de protéines ribosomales et jusqu'à 1MDa d'extensions d'ARNr appelées segments d'expansion (SE), avec un poids moléculaire de 4,3 MDa dans le cas du ribosome d'*Homo sapiens* (Melnikov et al., 2012; Ramesh and Woolford, 2016). Les SE présentent un haut degré de variabilité : tous les SE ne sont pas présents chez toutes les espèces. Leur longueur et leur séquence diffèrent au sein d'une même espèce, et des différences sont même constatées dans les répétitions d'ARNr d'un même organisme (Gonzalez et al., 1988, 1985; Ramesh and Woolford, 2016). La variabilité intrinsèque des SE et l'absence de systèmes robustes pour étudier la structure des parties flexibles de l'ARNr ont sérieusement entravé la compréhension approfondie de leur fonction. Localisés principalement à la surface du ribosome, les SE sont impliqués dans différents processus cellulaires, comme le suggèrent des expériences de délétion systématique d'SE spécifiques dans différents organismes. De manière intrigante, certaines de ces délétions n'ont aucun effet sur l'organisme étudié. Le mécanisme de traduction est étroitement régulé pour assurer une croissance cellulaire adéquate. En raison du rôle central joué par le ribosome, il n'est pas surprenant que l'arrêt ou l'altération de sa fonction puisse être préjudiciable et incompatible avec la vie. Le ribosome est en effet une cible antibactérienne validée puisqu'environ 40 % des antibiotiques sont des inhibiteurs du ribosome, comme le montre le nombre élevé de petites molécules identifiées pour se lier à la machinerie traductionnelle procaryote.

Suivant cet exemple, de nombreux inhibiteurs eucaryotes ont été identifiés au cours des dernières années. L'idée qui sous-tend l'inhibition des ribosomes eucaryotes est la même : le blocage sélectif de la machinerie de traduction et la modification du destin cellulaire pourraient avoir des effets bénéfiques sur diverses maladies humaines, comme pour les infections parasitaires ou l'évolution du cancer chez les individus (Yusupova et al., 2021). L'inhibition du ribosome a pour but de provoquer l'arrêt de la synthèse des briques nécessaires au maintien de la machinerie proliférative des cellules cancéreuses, ainsi que des champignons ou des parasites pathogènes, entraînant ainsi leur mort. Après la mise sur le marché du premier inhibiteur du ribosome pour le traitement de la leucémie myéloïde chronique en 2012 par la Food and Drug Administration (Kantarjian et al., 2013), le potentiel du ribosome comme cible pertinente pour le développement d'anticancéreux est devenu évident. La complexité du mécanisme de traduction et le nombre de sites fonctionnels sur le ribosome rendent la recherche de nouveaux inhibiteurs intrigante et fascinante. La principale source d'inspiration pour la découverte d'inhibiteurs du ribosome est la nature elle-même. En effet, la majorité des inhibiteurs naturels eucaryotes comme procaryotes sont des métabolites secondaires de champignons, de bactéries, de plantes ou d'éponges. Les développements en chimie médicale ont permis d'améliorer la puissance de ces inhibiteurs et/ou de diminuer la sévérité de leurs effets secondaires en introduisant des modifications rationnelles sur ces molécules sélectionnées par l'évolution. Au cours de mes travaux, j'ai utilisé des techniques structurales et des méthodes biophysiques pour sonder la complexité des interactions moléculaires : au sein des ribosomes avec l'étude de l'inhibition de la machinerie traductionnelle par des métabolites secondaires et des analogues synthétiques, mais aussi entre les ribosomes comme pour les complexes ribosomiques super-moléculaires.

Recherche sur le projet 1 : l'inhibition du ribosome eucaryote comme traitement anticancéreux potentiel

Les métabolites secondaires sont bien connus pour avoir une variété d'applications pharmaceutiques, y compris les voies antiprolifératives. Les diterpénoïdes labdanes contenant du succinimide, appelés lissoclimides, l'inhibiteur de glutarimide Gladiostatine de *B. gladioli* et l'alcaloïde Nitidine Chloride sont des produits naturels présentant un certain niveau d'inhibition de la traduction, y compris l'inhibition de la

croissance de plusieurs lignées cellulaires cancéreuses (Könst et al., 2017; Pellegrino et al., 2019). J'ai utilisé le ribosome de *S. cerevisiae* comme modèle pour étudier la liaison de ces produits naturels et de certains analogues synthétiques comme médicaments anticancéreux potentiels. Des efforts importants ont été consacrés à l'élucidation de la structure des complexes ribosome-inhibiteur afin de comprendre les bases moléculaires de l'inhibition. Cependant, les données structurales ont également été complétées par d'autres techniques biophysiques telles que la nano-fluorimétrie à balayage différentiel, l'ultracentrifugation analytique et la calorimétrie par titrage isotherme.

- Lissoclimides

Au cours des deux dernières décennies, les lissoclimides ont été largement caractérisés et signalés pour arrêter la traduction, montrant une puissante activité cytotoxique (Könst et al., 2017; Pellegrino et al., 2019). La synthèse totale des membres chlorés de cette famille de composés nous a permis d'étudier structurellement un type relativement nouveau d'interaction de dispersion entre les halogènes et les nucléobases (Könst et al., 2017; Pellegrino et al., 2019), ouvrant la voie à différentes substitutions halogènes et non-halogènes (F, Br, CH₃) qui pourraient, en principe, améliorer l'efficacité et réduire l'impact sur les cellules saines. En utilisant la forme cristalline du

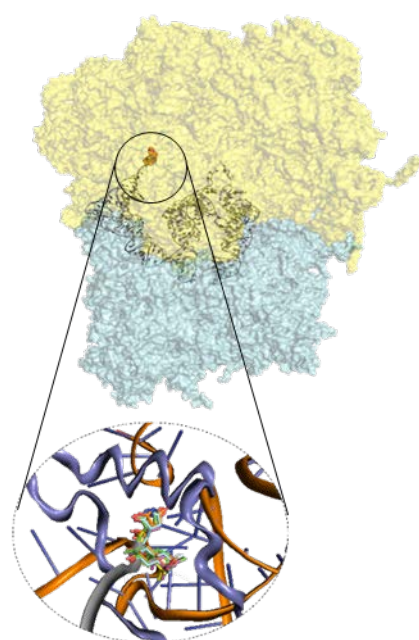


Figure 1 Site de liaison des lissoclimides.

ribosome de *S. cerevisiae*, j'ai résolu par cristallographie aux rayons X six structures du ribosome 80S eucaryote dans un complexe avec des congénères de lissoclimide portant différents groupes fonctionnels à une résolution comprise entre 2,9 et 3,2 Å. En outre, l'évaluation du changement de stabilité thermique induit par la liaison a été quantifiée par fluorimétrie à balayage nano-différentiel, soulignant l'importance primordiale des réseaux de liaisons H établis dans la poche de liaison. La comparaison entre les informations structurales révélées par la cristallographie aux rayons X et les essais de thermo-stabilité suggère une corrélation entre les liaisons H et la stabilité thermique des complexes, plus le réseau d'interaction est dense, plus l'effet sur la stabilité thermique est fort. Les substitutions halogénées jouent un rôle central dans l'ancrage des lissoclimides à leur site de liaison, comme le montre la comparaison entre

les lissoclimides halogénés et non halogénés liés au ribosome 80S. Compte tenu de la présence d'un seul site de liaison pour cette classe de composés, j'ai caractérisé thermodynamiquement la liaison des lissoclimides à l'aide de la calorimétrie par titrage isotherme, en affirmant la nature exergonique de leur interaction avec le site de liaison de l'ARNt du site E dans la grande sous-unité ribosomique.

- Gladiostatine

La Gladiostatine, un nouveau membre de la classe des glutarimides d'antibiotiques polycétides, est le produit métabolique d'une trans-acyltransférase de la bactérie *B. gladioli*. Cette molécule active nouvellement découverte, qui contient un rare 2-acyl-4-hydroxy-3-méthyl buténolide en plus de la 2, 6-pipéridinedione commune à tous les antibiotiques glutarimides, présente une puissance discrète contre *S. cerevisiae* mais une activité prometteuse contre plusieurs lignées cellulaires cancéreuses humaines tant du point de vue prolifératif que migratoire (Nakou et al., 2020). La structure du ribosome 80S en complexe avec la Gladiostatine a été résolue à une résolution moyenne de 3,6 Å par cristallographie aux rayons X, confirmant sa liaison à la poche de liaison de l'ARNt E sur la sous-unité ribosomique 60S. La résolution moyenne couplée à la flexibilité de la queue du polykétide n'a permis d'élucider que partiellement son mode de liaison, suggérant l'interaction directe de l'orbitale π du 2-acétyl-4-hydroxy-3-méthyl buténolide avec la protéine spécifique eL42 des eucaryotes. Malgré la faible résolution obtenue, la forte affinité de la fraction pipéridine dione pour le LSU indique la direction d'autres études pour développer des congénères de la Gladiostatine s'accommodant mieux dans sa poche de liaison.

- Nitidine Chloride

Le Nitidine Chloride (NC) est un alcaloïde d'ammonium quaternaire présentant de multiples activités biologiques. Des études ultérieures ont pointé du doigt le NC comme un composé antitumoral puissant dans une variété de malignités. L'activité antitumorale du NC implique différentes voies, de la suppression de la prolifération cellulaire à la stimulation de l'apoptose (Cui et al., 2020). Il a été démontré que la NC interfère avec la machinerie de traduction, en raison de la partie commune avec plusieurs autres inhibiteurs de traduction, on pensait qu'elle se liait au centre peptidyl transférase sur la grande sous-unité ribosomale. Malgré son influence sur le processus de cristallisation du ribosome, les études structurales avec les cristaux de ribosome de levure n'ont montré aucune liaison dans les conditions testées.

Projet de recherche 2 Analyse structurale des complexes tétramériques ribosomiques

Dès les premiers jours des études structurales des ribosomes, la question de savoir si les particules ribosomiques étaient cristallisables ou non a intrigué la communauté scientifique. Lorsque l'on pense au processus de cristallisation des complexes macromoléculaires, on pense à quelque chose d'artificiel et d'humain, un processus qui implique des étapes de purification et la recherche des bonnes conditions. Une fois de plus, la nature elle-même a aidé les

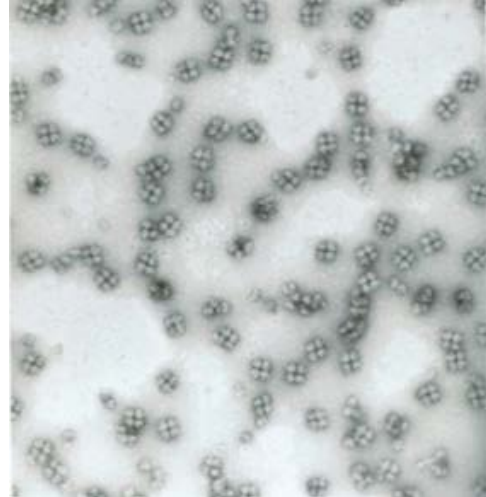


Figure 2 Tétramères des ribosome de poulet.

scientifiques à dévoiler des processus considérés jusqu'alors comme de pures spéculations et fantaisies. Depuis les premiers travaux de Beyer jusqu'aux études ultérieures de Morimoto et Ranieri (Barbieri, 1974; Byers, 1966; Morimoto et al., 1972a), il a été démontré que les ribosomes étaient non seulement des entités capables de cristalliser, mais qu'ils pouvaient le faire dans des conditions de vie. Les études mentionnées ci-dessus avaient montré comment les cellules embryonnaires de *G. gallus* et *L. sicala* étaient capables de former des feuilles bidimensionnelles de ribosomes cristallins appartenant au groupe spatial plan P4, si elles étaient exposées à des températures inférieures à 10°C. (Unwin and Taddei, 1977) Les couches cristallines bidimensionnelles de ribosomes pouvaient être séparées en leurs plus petites unités cristallographiques formées par quatre ribosomes en interaction, désormais appelées tétramères 80S, et purifiées intégralement. Ces agrégats ont confirmé la capacité des ribosomes à subir le processus de cristallisation, ouvrant la voie à l'âge d'or de la cristallographie des ribosomes. À la suite des études pionnières de Spirin et Yonath (Yusupova and Yusupov, 2015), les premiers cristaux tridimensionnels de ribosomes provenant d'organismes modèles "plus faciles à manipuler" ont commencé à apparaître, laissant peu ou pas d'espace pour les ribosomes de poulet. Durant la dernière partie de mon travail, je me suis concentré sur la tâche

d'établir un protocole pour la purification des tétramères et leur caractérisation. L'objectif principal était de comprendre les réarrangements tridimensionnels qui amènent les ribosomes actifs 80S à leur forme tétramérique, la nature des interactions maintenant ces particules ensemble et quels phénomènes biologiques sont à l'origine.

- Protocole de purification des tétramères

À partir de la littérature publiée du début des années 60 au début des années 80, un protocole de purification stable donnant des agrégats tétramériques de ribosomes a été établi dans différentes conditions de purification.

- Caractérisation et composition des tétramères.

L'échantillon obtenu a été caractérisé à l'aide de techniques standard en biologie structurale, leur composition en protéines et en acides nucléiques a été évaluée à l'aide de techniques de spectrométrie de masse et de gels standard SDS-page et gels d'agarose. Des expériences de diffusion dynamique ont été réalisées sur les tétramères déterminant leur rayon hydrodynamique, correspondant aux valeurs attendues de 300 Å. L'échantillon s'est révélé stable dans différentes conditions de force ionique, monodispersé et avec un bon degré de pureté d'abord suggéré par les expériences de DLS, puis confirmé par l'analyse par spectrométrie de masse.

- Cryo-EM sur les tétramères de poussins.

Après la visualisation via des images de coloration négative, des grilles de Cryo-EM de tétramères de ribosomes ont été préparées dans différentes conditions et deux ensembles de données principaux collectés sur différents microscopes. En raison des dimensions physiques des tétramères de ribosomes de poulet, la solution de leur structure tridimensionnelle n'est pas triviale et plusieurs problèmes ont été rencontrés lors du traitement des données qui sont actuellement confrontés à différents niveaux. Les résultats préliminaires à basse résolution montrent quelques caractéristiques intéressantes de ce complexe, à commencer par les interactions inhabituelles impliquant les grandes sous-unités de monomères et la présence d'autres ligands tels que l'ARN de transfert siégeant dans des sites fonctionnels.

Table of contents

Introduction

Ribosome: General Organization.....	15
Protein Synthesis.....	19
Protein Synthesis Regulation in Cancer.....	24
Translation Inhibition	26
Inhibitor targeting the 60S Ribosomal Subunit.....	29
Molecules binding to the A site.....	29
Molecules binding to the Peptide exit tunnel.....	33
Molecules binding to the P-site.....	34
Molecules binding to the E-site.....	36
Inhibitor targeting the 40S Ribosomal Subunit.....	40
Molecules binding to the mRNA path.....	40
Aminoglycosides Bind to helix 44 in the Decoding Site.....	42
Ribosome Tetramers.....	48

Research Project 1

Structural and Biophysical characterization of small molecules binding to the Ribosome as a potential anticancer treatment.

Aim of the project.....	53
Materials and Methods.....	55
Ribosome Purification.....	55
Ribosome Crystallization.....	57
Ribosome Post Crystallization treatments.....	58
Data collection and Data Processing.....	60
Data analysis and Model Building.....	61
Fo-Fo analysis on crystals containing lissoclimides.....	62
Thermal Stability evaluation.....	64
Isothermal Titration Calorimetry.....	68
Results and Discussion.....	72

Structure of Haterumaimide-Q in complex with the yeast Ribosome.....	75
Structure of Haterumaimide-J in complex with the yeast Ribosome.....	78
Structure of Methyllissoclimide in complex with the yeast Ribosome.....	81
Structure of Fluorolissoclimide in complex with the yeast Ribosome.....	84
Structure of Deoxyfluorolissoclimide in complex with the yeast Ribosome.....	87
Structure of Bromolissoclimide in complex with the yeast Ribosome.....	90
Lissoclimides Comparison.....	93
Lissoclimides Thermal Stability evaluation.....	97
Lissoclimides Cytotoxicity assays.....	99
Structure of Gladiostatine in complex with the yeast Ribosome.....	100
Conclusions and Perspectives.....	104

Research Project 2

Structural and Biophysical characterization of ribosome tetramers derived from chicken embryos exposed to hypothermia

Aim of the project.....	107
Materials and Methods.....	108
Chicken Ribosome complexes Purification.....	108
Chicken Ribosome complexes Characterization.....	112
Mass Spectrometry	114
Negative Stain Grids.....	118
Grids Preparation and screening on Glacios IGBMC.....	119
Data Processing data collected on Glacios IGBMC.....	120
Grids Preparation, screening and data collection on Titan Kryos DCI.....	123
Data Processing data collected on Titan Kryos DCI	124
Preliminary Results and Perspectives.....	131
Appendix.....	135
Bibliography.....	142

List of figures

Figure 1.....	Site de liaison des lissoclimides.
Figure 2.....	Tétramères des ribosome de poulet.
Figure 3.....	Prokaryotic and Eukaryotic ribosome comparison.
Figure 4.....	The ribosome common core.
Figure 5.....	Translation in Prokaryotes and Eukatyotes.
Figure 6.....	Protein synthesis inhibitors cluster to ribosomal functional sites.
Figure 7.....	Protein synthesis inhibitors target several steps of translation.
Figure 8.....	Inhibitors binding to the A-site cleft impede the binding of the aa-tRNA during elongation.
Figure 9...	Inhibitors binding to the PTC impair elongation of the nascent chain and can be sequence specific.
Figure 10.....	Inhibitors binding to the E-site of the LSU impair the translocation process.
Figure 11.....	The SSU can be targeted by protein synthesis inhibitors at two main regions.
Figure 12.....	Aminoglycosides bind preferentially to the DC of the eukaryotic ribosome.
Figure 13.....	Ribosome sucrose gradient profiles.
Figure 14	30-10 % sucrose gradient profile of <i>Saccharomyces cerevisiae</i> ribosomes measured on Nanodrop
Figure 15.....	Cryoprotection dehydration and soaking scheme for 80S yeast ribosome crystals.
Figure 16.....	80S yeast ribosome crystals mounted in SLS PX1-X06SA goniometer.
Figure 17.....	Cell parameters percentual difference plot.
Figure 18...	Superimposition of thermal stability profiles of 80S ribosomes in complex with different lissoclimides.
Figure 19.....	Comparison between thermal stability profiles of lissoclimides and the DMSO control.
Figure 20.....	Workflow of Isothermal Titration Calorimetry data processing.
Figure 21.....	Thermogram of the replicate of the Isothermal Titration Calorimetry experiment of Haterumaimide J binding the yeast 80S ribosome.
Figure 22.....	2D representation of lissoclimides.
Figure 23.....	Lissoclimides binding site in a yeast silico model of the 80S ribosome.
Figure 24.....	Haterumaimide Q Overview.
Figure 25.....	Haterumaimide Q binding site.
Figure 26.....	Haterumaimide Q vs Chlorolissoclimide.
Figure 27.....	Haterumaimide-J Overview.
Figure 28.....	Haterumaimide-J binding site.
Figure 29.....	Haterumaimide-Q vs Haterumaimide-J.
Figure 30	Methylissoclimide Overview.
Figure 31.....	Methylissoclimide binding site.
Figure 32.....	Haterumaimide-Q vs Methylissoclimide.
Figure 33.....	Fluorolissoclimide overview.
Figure 34.....	Fluorolissoclimide binding site.
Figure 35.....	Haterumaimide-Q vs Fluorolissoclimide.

Figure 36.....	Deoxyfluorolissoclimide overview.
Figure 37.....	Deoxyfluorolissoclimide binding site.
Figure 38.....	Haterumaimide-Q vs Deoxyfluorolissoclimide.
Figure 39.....	Bromolissoclimide Overview.
Figure 40.....	Bromolissoclimide binding site.
Figure 41.....	Haterumaimide-Q vs Bromolissoclimide.
Figure 42.....	BrL-vs-CL-vs-FL.
Figure 43.....	Residual density Fo-Fo calculation on Hat-Q.
Figure 44.....	FL vs DFL.
Figure 45.....	Residual density Fo-Fo calculation with Hat-J.
Figure 46.....	FL vs DFL.
Figure 47.....	Residual density Fo-Fo calculation on FL-DFL.
Figure 48.....	Lissoclimide thermostabilizing effect on the eukaryotic yeast 80S ribosomes.
Figure 49.....	Lissoclimide cytotoxicity values.
Figure 50.....	Overview of Gladiostatine.
Figure 51.....	Gladiostatine (GLD) network of interactions within the 60S E-site pocket.
Figure 52.....	Gladiostatine network of interactions.
Figure 53.....	Structural superimposition of glutarimide inhibitors.
Figure 54.....	40-20% sucrose gradient profiles of concentrated S30 fraction.
Figure 55.....	40-20 % sucrose gradient profiles of pulled and concentrated tetrameric peaks in figure 52.
Figure 56.....	40-20% sucrose gradient profiles of pulled and concentrated monomeric peaks in figure 52.
Figure 57.....	40-20% sucrose gradient profile of dissolved ribosomal pellet recovered after sucrose cushion.
Figure 58.....	Chick ribosome gels.
Figure 59.....	Dynamic Light Scattering (DLS) plot of chicken tetramers and monomers at 2 mg/ml.
Figure 60.....	Negative stain micrographs of chick tetrameric complexes.
Figure 61.....	Micrographs collected on Glacios at IGBMC.
Figure 62.....	Work flow of data processing performed on the dataset collected on Glacios at IGBMC.
Figure 63.....	Tetramers homogeneous refinement workflow.
Figure 64.....	Micrographs collected on Glacios at DCI.
Figure 65.....	Volume determination procedure.
Figure 66.....	First attempt of chick ribosome tetramers reconstruction.
Figure 67.....	Ab initio reconstruction behavior as a function of particle number.
Figure 68.....	Ab initio reconstructed volumes.
Figure 69.....	Tetramers homogeneous refinement workflow.
Figure 70.....	3D Variability results for tetramers and monomers extracted from tetramers.
Figure 71.....	80S monomer isolated from tetramers homogeneous refinement workflow.
Figure 72.....	Cryo-EM reconstructions of tetramers and monomer from tetramers.
Figure 73.....	80S monomer isolated from the tetramer's assembly.

Introduction

Ribosomes: General organization

From the smallest prokaryotic organism to the giant humpback whale, protein synthesis plays a vital role across all life domains. The main actor in this process is the ribosome. This massive ribonucleoprotein machinery reads the genetic code, in the form of messenger RNA, to synthesize proteins during a finely tuned process called translation. Ribosome sizes range from 2.5 MDa in prokaryotes to 4.3 MDa in higher eukaryotes. Three types of ribosomal RNA (rRNA) and 54 ribosomal proteins (RPs) make up the bacterial 70S ribosome. Eukaryotic ribosomes are instead much more complex machinery as their size varies within the eukaryotic domain. For instance, *Saccharomyces cerevisiae* ribosomes are made of 4 types of rRNA and 79 RPs, reaching the size of 3.3 MDa while animal and plant ribosomes contain additional sets of ribosomal proteins and up to 1MDa of rRNA, extensions called expansion segments (ESs) with a molecular weight of 4.3 MDa in case of *Homo sapiens* (Melnikov et al., 2012; Ramesh and Woolford, 2016).

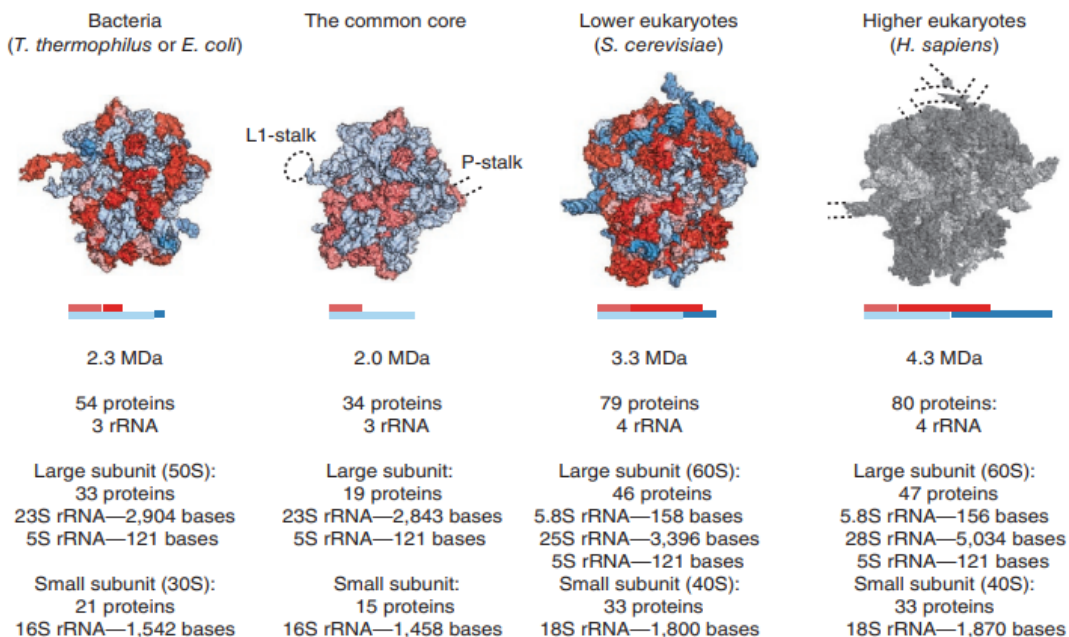


Figure 3 Prokaryotic and Eukaryotic ribosome comparison. Adapted from One core two shells Prokaryotic and Eukaryotic ribosomes. Prokaryotic and Eukaryotic ribosomes have in common a core composed of RNA (light blue) and proteins (light red). Additionally, ribosomes in each domain of life have their specific set of proteins. Extensions and insertions can be observed in conserved proteins (in red), and expansion segments in ribosomal RNA (in blue). 5.8S and 25S–28S rRNA are both homologous to 23S rRNA in bacteria. Flexible stalks of the ribosome are indicated with dashed lines around the core. Hence, the yeast 80S structure is shown in color and in gray. The grey structure has dashed lines indicating human-specific long RNA expansion segments.

Ribosomes are made of two different subunits, the Large Subunit 60S in eukaryotes (50S in prokaryotes) and the Small Subunit 40S in eukaryotes (30S in prokaryotes), these two subunits join together during translation to form the 80S ribosome in eukaryotes (70S in prokaryotes). Ribosomal RNA accounts for 80% of the total cellular RNA fraction in the cell (Warner, 1999). Different rRNA molecules compose the ribosome. They differ in their Svedberg coefficient. The small subunit is constituted of only one ribosomal RNA molecule denoted as 16S in bacteria and 18S in eukaryotes. In eukaryotes the large subunit is formed by three different sizes and shapes of rRNA molecules (5S, 5.8S, and 25S) while two are observed in prokaryotes. The three-dimensional arrangement of RNA is achieved in sequential steps. Ribosome biogenesis starts in the nucleolus of the eukaryotic cell. In this cellular compartment proteins and ions (K^+ , Mg^{2+}) participate in a fascinating lock and key mechanism of construction to shape the folding of rRNA. ((Klein et al., 2004; Rozov et al., 2019). Driven by base-pairing interaction, the assembly of different secondary structure elements takes place at the first stages of folding, originating a wide group of different secondary motifs. Three-dimensional folding brings distant secondary elements (even those far in the 2D fold) together to form a solid rearrangement. As for the secondary structure also in the three-dimensional fold, we can appreciate conserved structures. To mention the most frequently found in rRNA: ribose zipper, A-minor motif, and helices coaxial stacking (Cate and Doudna, 1996; Nissen et al., 2001). The role of rRNA in the three-dimensional organization of all ribosome functional sites is of paramount importance. rRNA shapes the mRNA channel, the peptide exit tunnel, and sites where tRNA are accommodated and reoriented to perform their biochemical role. The catalytic nature of RNA makes it a central player in ribosome function. From the central reaction of peptide bond formation within the large subunit to the selection of the right aminoacyl-tRNA during decoding the role of rRNA residues is often conserved through evolution (Demeshkina et al., 2012; Ogle et al., 2001). It has been proposed that the whole ribosome has evolved around a quasi-symmetric core capable of carrying the translation central reaction. This central core situated within the large subunits is constituted of two loops, respectively the A and the P-loop. It has been shown that this element alone is capable of performing the reaction mentioned above (Bose et al., 2022). As mentioned before, one of the causes of the difference in ribosome sizes across different domains is the length of the rRNA primary structure. Insertions and deletion of rRNA are trackable on the evolutionary tree of life and are

broadly used in phylogenetic comparison studies (Olsen and Woese, 1993). The previously introduced ESs show a high degree of variability: not all ESs are found in all species. Their length and sequence differ within the individuals of the same species, and differences are even found in rRNA repeats of the same organism (Fujii et al., 2018; Ramesh and Woolford, 2016). An impressive example is given by the large expansion segment named ES27L (Figure 4). It is constituted of about 150 nt in yeast and 700 nt in mammals with a high level of variability ref. The highest number of variations in the eukaryotic rRNA is found in the LSU (Cannone et al., 2002). The LSU of some protozoan members is characterized by a secondary shell of RNA and protein encircling the common core. *H. sapiens* and other homeothermic vertebrates possess rRNA “tentacles” (or long ESs), visualized as helical structures extending for hundreds of Angstroms from the ribosome. These tentacles are not packed on the ribosomal surface in standard conditions and they show a high degree of dynamicity appearing most often disordered within the cytosol. The intrinsic variability of ES and the lack of a robust system to structurally study flexible parts of rRNA have seriously impaired the deep understanding of their function. ES are involved in different cellular processes as suggested by systematic deletion experiments of specific ES in different organisms. For instance, the deletion of ES27L in the large subunit of *Tetrahymena* was found to be lethal thus supporting a functional role (Sweeney et al., 1994). Intriguingly, some of these deletions do not affect the studied model. Ribosomes are protein-RNA complexes capable of catalytic activity. The protein composition of ribosomes has a crucial role in their structure and function. RPs are among the most abundant proteins in the cell and they accomplish fundamental tasks during translation, for example, proteins from the ribosomal stalk, P1/P2 in eukaryotes (L7/L12 in bacteria) participate in and coordinate the recruitment of translation factors at the ribosomal A-site (Gao et al., 2009). The role of ribosomal proteins in the functioning of the translational machinery has been for a long time a topic of discussion. Originally thought to have the role of principal actors, with rRNA relegated to the role of the simple scaffold, nowadays a solid corpus of evidence has changed this first model completely. The dual contribution of both proteins and rRNA in the translation process is now widely accepted. Several important roles are fulfilled by ribosomal proteins. Some of them sit in the free space left by rRNA three-dimensional fold, snaking between rRNA elements and stabilizing the whole assembly. Others, as already mentioned actively participate in the translation process. They interact with ligands

and play a role in translation fidelity (Schmeing and Ramakrishnan, 2009; Steitz, 2008))

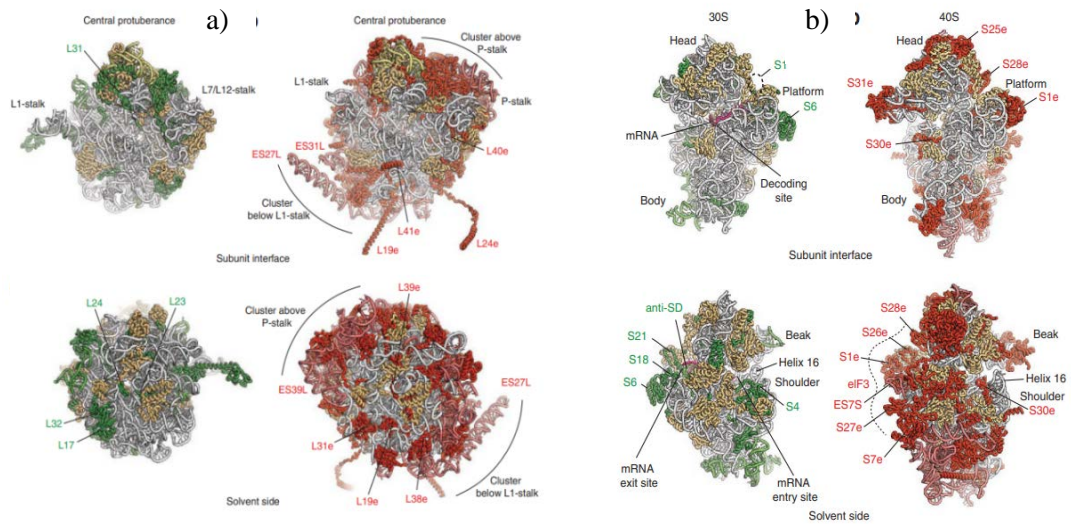


Figure 4 The ribosome common core. Adapted from One core, two shells: bacterial and eukaryotic ribosome. The conserved core of both subunits is represented in grey (rRNA) and ochre (proteins). a) In green are indicated the prokaryotic-specific moieties of the 50S subunit and in red the eukaryote-specific moieties of the 60S subunit. The principal expansions segments in the eukaryotic large subunit are also labelled. b) In green are indicated the prokaryotic-specific moieties of the 30S subunit and in red the eukaryote-specific moieties of the 40S subunit.

A considerable number of ribosomal proteins exhibit functions that are not directly connected with translation, having as well a role in the regulation of transcription and translation and cell signaling (Warner and McIntosh, 2009; Wool, 1996). A striking example is given by the S3 protein in *Homo sapiens*, where the immune response activating lymphocytes cause the translocation of S3. This ribosomal protein after moving inside the nucleus plays the role of one of the subunits of NF- κ B complexes (Wan et al., 2007). Many other examples of ribosomal proteins involved in different cellular processes can be listed, and the experimental shreds of evidence are growing every year.

Protein synthesis

Protein synthesis is characterized by four main steps: initiation, elongation, termination and recycling. Despite the fact that differences are present between eukaryotes and prokaryote, in this section the process in eukaryotes will be discussed emphasizing when necessary the differences with the prokaryotic counterpart.

- Initiation,

where mRNA is recruited to the 40S ribosome; the initiator tRNA and the 60S ribosome join to form an elongation-competent 80S ribosome. When the 80S ribosome is functionally assembled on mRNA the elongation phase can properly start. The 43S pre-initiation complex (PIC) is constituted by the ternary complex (TC) (eIF2-GTP-Met-tRNAⁱMet), eIF1, eIF1A, eIF3, eIF5 and small ribosomal subunit 40S. Each factor in this complex plays a vital role in translation initiation; eIF1 and eIF1A along with the massive eIF3 are involved in the mRNA scanning process that will lead to the right positioning of the first start codon (AUG)(Aitken and Lorsch, 2012). Conformational changes in the RNA-binding cleft support the scanning procedure. Start codon recognition triggers eIF1 release and conversion of eIF2 to its GDP-bound state, hindering the scanning process. eIF2•GDP and eIF5 dissociate, leaving the stage to eIF5B that will mediate the joining of the 60S subunit. The later steps of initiation are followed by eIF5B-GTP hydrolysis and factor dissociation to finally assemble the 80S initiation complex (IC) (figure 5)(Aitken and Lorsch, 2012).

- Elongation,

where the decoding of mRNA drives the consecutive incorporation of amino acids carried by the tRNAs in a process called peptide bond formation occurring in one of the main functional sites on the ribosome: the peptidyl transferase centre (PTC). The elongation step of translation is mechanistically conserved in all kingdoms of life with little differences in the factor composition pool. Following the formation of the 80S initiation complex in which Met-tRNAⁱMet is located in the P (peptidyl) site of the ribosome, the anticodon of the Met-tRNAⁱMet is base-paired with the start codon of the messenger RNA (mRNA), and the second codon of the open reading frame (ORF) seats in the A (aminoacyl) site of the ribosome. Elongation commences with delivery of the cognate elongating aminoacyl-tRNA (transfer RNA) to the A site of the ribosome (figure 5). The eukaryotic translation elongation factor eEF1A, activated

upon binding guanosine triphosphate (GTP) recruits the aminoacyl-tRNA furtherly forming the elongation ternary complex. The network of interactions formed between the anticodon of the aminoacyl-tRNA and the A-site codon trigger GTP hydrolysis and the EF1A-GDP complex is released leading to the proper accommodation of the into the A site. During the last decade, the intricate network of interaction governing the decoding step of translation has been partially elucidated. An ensemble of transversally conserved residues form helix h44 in the small ribosomal subunit interacts with the minor groove of the codon-anticodon helix formed by mRNA and tRNA. Residues from h44, both in prokaryotes and eukaryotes, can flip in and out from the helix, establishing connection with the near-cognate tRNAs in the A site inducing tRNA rejection if the base pair condition is not fulfilled assuring a certain level of translation fidelity (Demeshkina et al., 2012). Additionally to the rRNA contribution, it has been proposed (Shao et al., 2016) that the amino terminus of the eukaryote specific ribosomal protein eS30, normally disordered, becomes structured upon cognate codon–anticodon interaction in the A site, enabling the conserved histidine residue to form potentially stabilizing contacts (Dever et al., 2018). The core reaction of translation is indisputably the peptide bond formation. It takes place in the peptidyl transferase centre (PTC) within the large ribosomal subunit. All the translational machinery has evolved around this common core, most likely a vestige of an ancient RNA world (Ben-Shem et al., 2011; Bose et al., 2022; Klinge et al., 2011). All the molecular movements described until now evolved to bring in the right conformation all different substrate involved in this process. Once the aminoacyl-tRNA is correctly positioned into the A site and all readthrough controls have been executed, peptide bond formation with the peptidyl-tRNA in the P site occurs quickly. The contribution of translation factors in this process is thought to be crucial, in fact the factor eIF5A, bound to the E site, establishes contacts with the acceptor arm of the peptidyl-tRNA, triggering the peptide bond formation by inducing a favorable rearrangement of the substrates (Gutierrez et al., 2013; Melnikov et al., 2016, 2016; Schmidt et al., 2016; Shin et al., 2017). In an almost simultaneous way, the peptide bond is formed, IF5A dissociates and the nascent chain is moved from the peptidyl-tRNA in the P site to the amino group of the acylated transfer RNA in the A site, yielding a longer peptidyl-tRNA that will later sit within the previously occupied P site. At this particular point, the positioning of transfer RNA molecules within the 80S assumes different positions known as hybrid states. Parallely the rotation of subunits occurs as extensively described (Moazed and Noller, 1989). Thanks to the advances in Cryo-electron

microscopy it has been possible to further shed light on the movements of transfer molecules during translation. It has been possible to identify different states of rotation during the elongation phase.

- The fully unrotated state where the freshly formed peptidyl-tRNA is in the A site and deacylated tRNA stays in the P site. (Behrmann et al., 2015)
- The class 1 rotated complexes, where the deacylated tRNA assumes the so-called hybrid P/E position with the anticodon interacting with the mRNA in the P site and the acceptor arm of the tRNA moving towards the E site. Meanwhile the peptidyl-tRNA stays in the classic A site (Behrmann et al., 2015; Budkevich et al., 2011)
- The class 2 rotated complexes in which the deacylated tRNA is in the hybrid P/E state and the peptidyl-tRNA has moved into a hybrid A/P state with the anticodon stem loop still anchored with mRNA in the A site and the nascent polypeptide chain attached to the acceptor arm in the P site (Behrmann et al., 2015)

At this point, the ribosomal A site needs to be freed in order to allow the accommodation of the next aminoacyl-tRNA. This process is known as translocation and it will bring tRNAs to the canonical E/E and P/P states. This rearrangement of transfer molecules within the ribosome is promoted by the elongation factor eEF2. Early structural studies unveiled the position of this factor, placing its binding site within the A site, its role involved the unlock of the decoding interaction previously established in the A site thus allowing the movement of peptidyl-tRNA to the P/P state, along with the mRNA template (Murray et al., 2016; Spahn et al., 2004; Taylor et al., 2007). Structural studies have revealed that eEF2 binds in the A site where it unlocks the decoding interaction of the helix h44 nucleotides with the codon-anticodon duplex in the A site. When eEF2 accommodates in its pocket several events occur in the 40S subunit. The head domain swivelling and the anti-clockwise rotation of the small subunit relative to the large subunit accompanies the displacement of tRNAs into the canonical P and E sites (P/P and E/E states) (Djumagulov et al., 2021; Dn and Hf, 2011; Ramrath et al., 2013; Ratje et al., 2010) allowing eEF2•GDP dissociation from the post translocation ribosome. Following translocation, a deacylated tRNA occupies the E site and peptidyl-tRNA is positioned in the P site, leaving the A site free and ready to accommodate another aminoacyl-tRNA for another elongation round (figure 5).

- Termination and recycling,
where the ribosome encounters a stop codon and triggers release of the nascent polypeptide chains and subunits dissociation. Termination of mRNA translation starts when one of the possible stop codons enters the A site of the ribosome, and in the eukaryote domain is mediated by two release factors eRF1 and eRF3. These two proteins form along with GTP the so-called eRF1/eRF3–guanosine triphosphate (GTP) complex. eRF1 following the recognition of the stop codon, and the immediately after hydrolysis of GTP by eRF3, mediates the release of the formed polypeptide chain (Alkalaeva et al., 2006; Bertram et al., 2000; Jackson et al., 2012). The post-termination complex is then disassembled, allowing its constituents to participate in more rounds of translation. Ribosome recycling involves splitting of the 80S ribosome by the ATP-binding cassette protein ABCE1 to release the 60S subunit (Mantsyzov et al., 2010). Subsequent dissociation of deacylated transfer RNA (tRNA) and messenger RNA (mRNA) from the 40S subunit may be mediated by initiation factors (priming the 40S subunit for initiation), by ligatin (eIF2D) or by density-regulated protein (DENR) .These events may be subverted by suppression of termination (yielding carboxy-terminally extended read-through polypeptides) or by interruption of recycling, leading to re-initiation of translation near the stop codon (Hellen, 2018; Weisser et al., 2017) (figure 5)

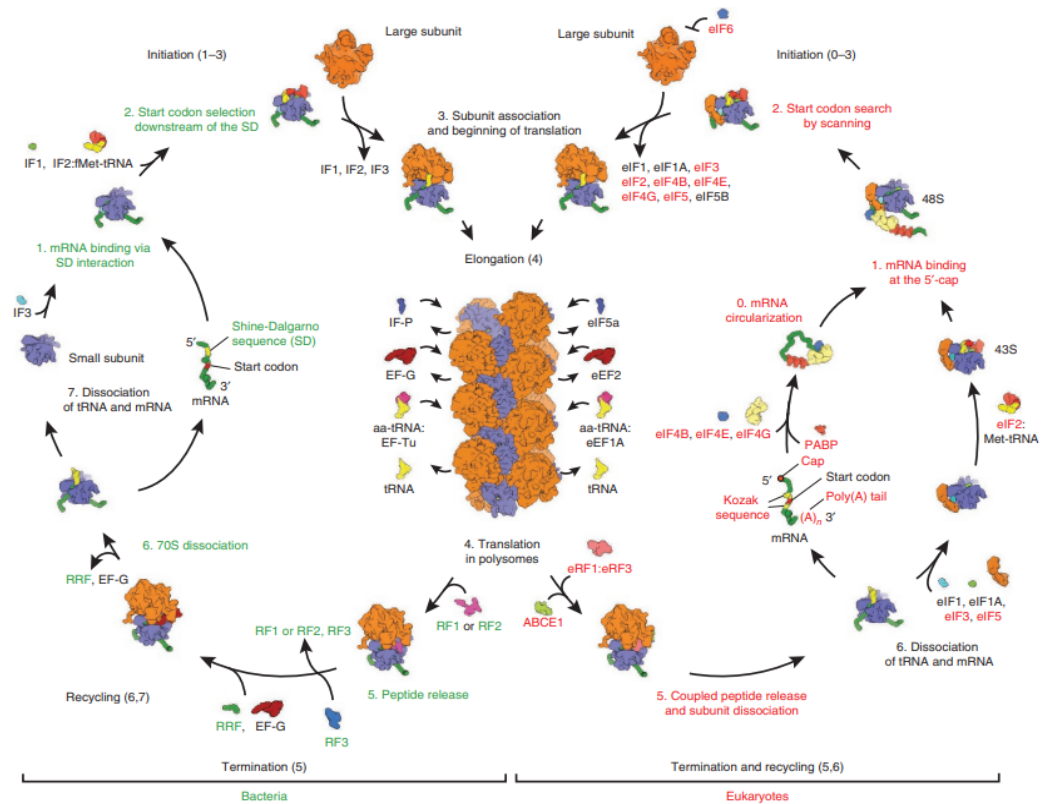


Figure 5 Translation in Prokaryotes and Eukaryotes. Adapted from One core, two shells: bacterial and eukaryotic ribosome. Translation is a process composed of four main steps. It includes the steps of initiation, elongation of the polypeptide chain, termination and recycling. Protein factors named initiation factors (IFs in bacteria or eIFs in eukaryotes), elongation factors (EFs or eEFs), release factors (RFs or eRFs) and recycling factors assist each step of this process. Elongation is the most conserved step among kingdoms of life and it is assisted by homologous elongation factors. During this step, ribosomes gather together in large helical complexes, known as polysomes, in which the inner region is occupied by the small ribosomal subunits and mRNA and the outer one is composed by the large ribosomal subunits from which the nascent peptide is gradually extruded. The other steps of the translation cycle account more differences and possess several stages (numbered in figure) that are different between prokaryotes (green) and eukaryotes (red). The initiation, termination and release factors catalysing these steps have a lower level of homology among different kingdoms and many proteins specific to either prokaryotes (green) or eukaryotes (red) act during these phases.

Protein synthesis regulation in cancer

When a cell undergoes the process that will lead to malignant transformation, levels and rates of protein translation appear to be affected in different ways (Robichaud et al., 2019; Silvera et al., 2010). Mis-regulation can appear at any time during protein synthesis. In the last years several studies have described in details how cancer can affect all steps of translation the initiation step in translation has been reported to be implicated in cancer genesis and cell transformation. The transcribed material, as stated before, is translated by ribosome into polypeptide chains. The analysis of mRNA translation rates by the ribonucleic machinery revealed that the cell proliferation controlling process is maintained by protein synthesis, highlighting how translation heavily contributes to overall gene expression (Silvera et al., 2010). In the translation process, regulation is often performed during the initiation phase, as this particular checkpoint possesses some rate-limiting features (Robichaud et al., 2019). Initiation rate can be altered either by variations in initiation factors availability or activity regulation by key signalling pathways, such as phosphatidylinositol-3-OH kinase (PI3K)/AKT, mammalian target of rapamycin (mTOR), and mitogen-activated protein kinase (MAPK) pathways (Ma and Blenis, 2009; Pyronnet et al., 1999; Waskiewicz et al., 1997). Eukaryotic translation initiation factors (eIFs) are proteins that help in stabilizing the formation of the functional ribosomal complex around the start codon and provide the quality control apparatus in translation initiation. Currently, there are six eIFs reported to be involved in translation initiation, and most of the eIFs are a protein complex of several subunits, and dysregulations in their expression by overexpression, downregulation, or phosphorylation lead to oncogenic progression (Robichaud et al., 2019; Silvera et al., 2010). Data have recently shown how important is the elongation stage of protein synthesis for translational control in health and disease. Remarkably, the central role played by the dysregulation of elongation control is has been pointed as a mechanisms triggering tumorigenesis and neurodegeneration (Knight et al., 2020). The variate group of factors individually controlling the global rate of translation can act in different ways. The influence of tRNA and eukaryotic eEF1A-dependent codon decoding has been observed. Additionally, eEF2-dependent ribosome translocation along the mRNA seems to be negatively regulated by a phosphorylation on threonine 56 carried by an eEF2 kinase.

The downregulation of translocation rates has been linked to the survival increase of rapidly proliferating solid tumours, where, due to the poor vascular structure, cancer cells have to adapt to prolonged nutrient deprivation (Leprivier et al., 2013; Liao et al., 2016). For instance, the energy conservation derived by slower rates of translocation has positive effects on survival of oncogene-transformed fibroblasts (Leprivier et al., 2013). Several other factors can contribute to controlling the elongation rate, epigenetic modification of the mRNA to mention one (Knight et al., 2020). Accurate termination of mRNA translation is essential to produce a fully functional protein (Dabrowski et al., 2018; Hellen, 2018). Consequently, termination and ribosome recycling are highly dynamic processes regulated by a multitude of ribosome binding proteins and dysregulation of these pathways leads to disease, including cancers. Defects in termination can result in stop codon readthrough, where the ribosome fails to terminate at the stop codon and continues to translate the 3' UTR of the mRNA. Readthrough can lead to a loss in the production of functional protein as well as disrupting ribosome subunit recycling and subsequent rounds of translation. The production of truncated polypeptides usually leads to their loss of functionality, involved in oncogenesis along with other diseases. (Dabrowski et al., 2018; Hellen, 2018; Jackson et al., 2012).

Translation inhibition

As it has been just described, translation mechanism is tightly regulated to ensure proper cell growth. Dis-regulation of the translation process in its different steps might lead to oncogenesis and cellular degeneration. Because of the central role played by the ribosome, it is not surprising that cessation or alteration of its function can be detrimental and incompatible with life. Ribosome is indeed a validated antibacterial drug target since about 40% of antibiotics are ribosome inhibitors, as highlighted by

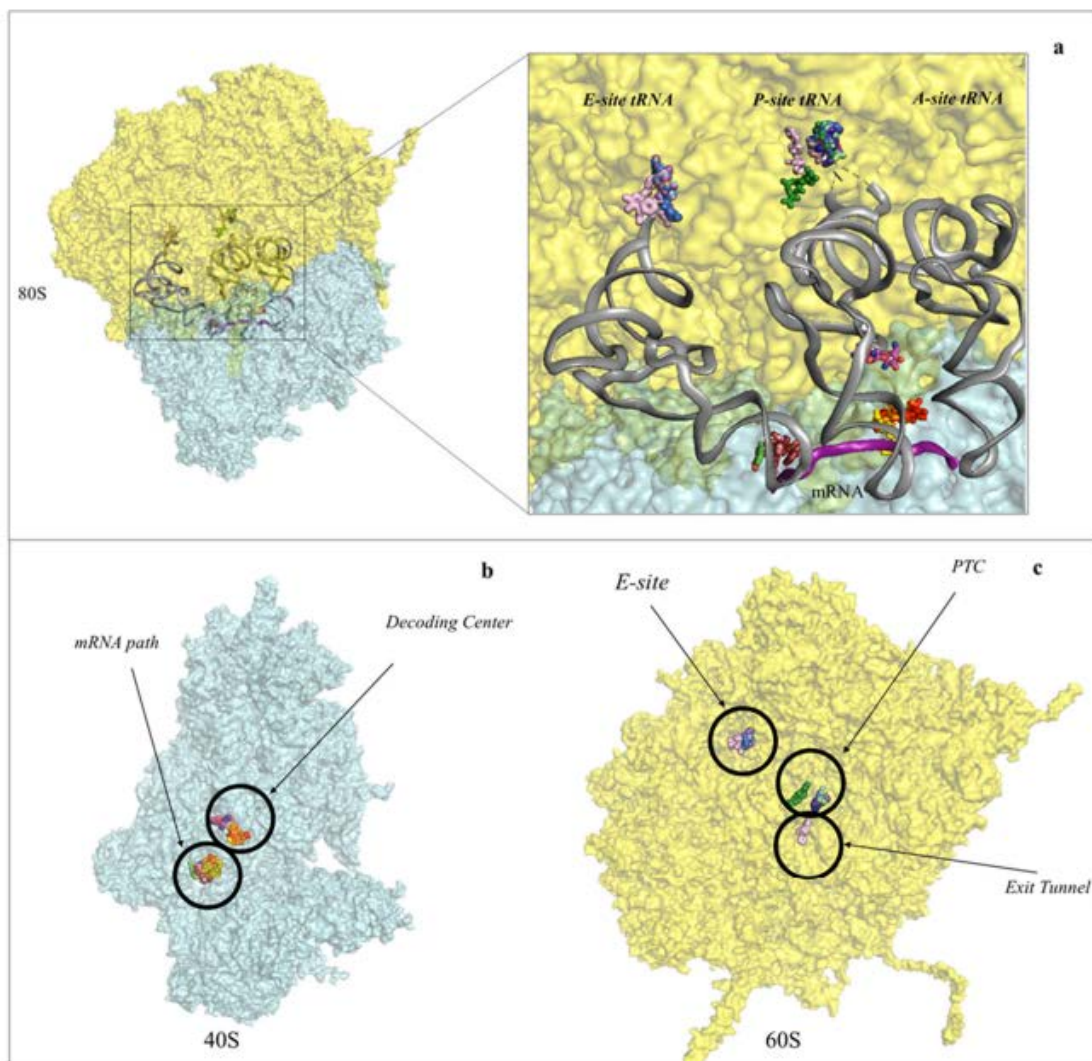


Figure 6 Protein synthesis inhibitors cluster to ribosomal functional sites. Adapted from Pellegrino et al a) Left-hand side, overview of the eukaryotic 80S ribosome, shown as surface representation. LSU is coloured in cyan, SSU in pale yellow. The three tRNAs and mRNA have been modelled in silico after superposition of the *Thermus thermophilus* elongating complex (PDB: 4V5D) to the yeast vacant 80S model (PDB: 4V88). Right-hand side, zoom-in of the regions where inhibitors bind within the ribosome. For clarity the functional sites are labelled. PTC: peptidyl-transferase centre; PET: peptide exit tunnel; DC: decoding centre. b) Binding of small molecule inhibitors to the eukaryotic SSU. Drugs are represented as spheres, SSU as surface. The functional sites targeted are displayed. c) Binding of small molecule inhibitors to the eukaryotic LSU. Drugs are represented as spheres, SSU as surface.

the high number of small molecules identified to bind the prokaryotic translational machinery (A, 2005; Blair et al., 2015). Following this example, many eukaryotic inhibitors have been identified during the last years (Garreau de Loubresse et al., 2014; Pellegrino et al., 2019; Prokhorova et al., 2017)(figure 6). The idea behind eukaryotic ribosome inhibition is the same: selectively blocking the translation machinery and altering the cell fate might bring positive effects on a variety of human diseases, from parasite infections to cancer evolution in individuals. With an inhibited translation machinery, cancer cells along with pathogenic fungi or parasites will not be able to synthesize all bricks needed to sustain their proliferative machinery, encountering death (Gilles et al., 2020; Yusupova et al., 2021). Starting from the approval of the first ribosome inhibitor for the treatment of cancer resistant to first line treatments, the potential of ribosome as a relevant target for the development of anti-cancer drugs became clear. The complexity of translation mechanism and the number of functional sites on the ribosome makes the research of new inhibitors intriguing and fascinating. The main source of inspiration in the quest of ribosome inhibition is nature itself. As for the prokaryotic counterpart, the majority of eukaryotic inhibitors come from natural sources, from fungi to bacteria including plants, sponges or other animals(Brönstrup and Sasse, 2020; Burgers and Fürst, 2021; Trendowski, 2015). Developments in Medical Chemistry allowed to widen the range of possibilities, introducing rational changes on evolutionarily selected molecules, improving their potency and/or decreasing the severity of their side effects. Structural works focused on unravelling the binding mode of these molecules within the ribosome have been, and yet are, of paramount importance for understanding the molecular basis of inhibition in all organisms and guide drug design strategies to develop novel molecules able to elude resistance mechanisms (Osterman et al., 2020). The eukaryotic ribosome is the target of naturally derived small molecule inhibitors (figure 6, 7). Several compounds are known to hinder translation at different steps (figure 7), as suggested by extensive functional works (Barbacid et al., 1975; Chan et al., 2004; Matzov et al., 2017; Svetlov et al., 2021). Inhibitors of eukaryotic protein synthesis, besides being routinely used for research purposes, hold great potential as anti-cancer therapeutics and to correct for genetic disorders (Chan et al., 2004; Schneider-Poetsch et al., 2010). A striking example is represented by the drug omacetaxine mepesuccinate (also called Homoharringtonine (HHT)) used for treatment of chronic myeloid leukaemia (CML) (figure 6, figure 8). Homoharringtonine represents the first protein synthesis' inhibitor approved by the Food and Drug Administration to be prescribed to individuals that

develop resistance towards tyrosine kinase inhibitors, commonly used as first line in chronic myeloid leukaemia treatment (Kantarjian et al., 2013). The majority of cancers are caused by a hyper-proliferative phenotype that is responsible for an indefinite growth. Fine-tuning the activity of translation inhibitors would likely represent a promising way to counteract the rapid growth of cancer cells, but thorough optimisation is needed to avoid secondary effects. Furthermore, the use of ribosome inhibitors to treat human diseases has also received particular attention to promote premature termination codon (PTeC) read-through in rare genetic disorders (Dmitriev et al., 2020; Mattis et al., 2006; Prokhorova et al., 2017). Furthermore, there is increasing evidence that rRNA modifications and pervasive sequence variation in rRNA can be related to differential expression in human cells and tissues to originate “specialised” ribosomes, suggesting also a possible link with cancer onset (Burgers and Fürst, 2021; Gilles et al., 2020). Different patterns of rRNA modifications expand further the complexity of designing more potent and highly specific anti-cancer drugs. Visualising these “specialised” ribosomes will provide new understanding at functional level but, more importantly, will serve to gather a much more refined structural interpretation of the ribosomal druggable sites.

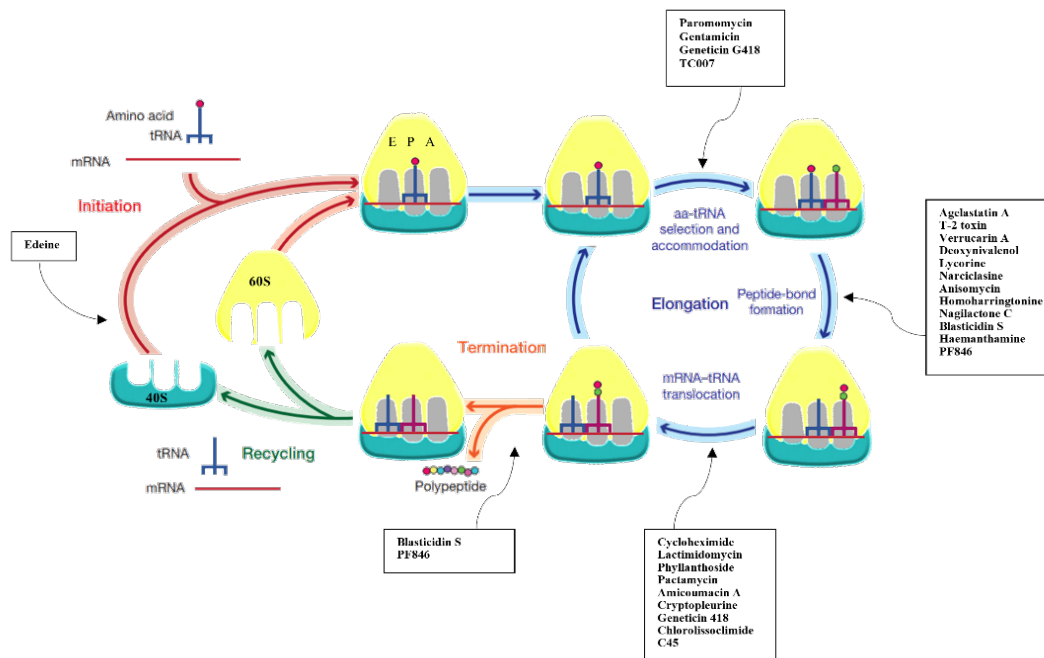


Figure 7 Protein synthesis inhibitors target several steps of translation. Adapted from Pellegrino et al Scheme reporting the different phases of protein synthesis: 1) initiation, where initiator tRNA (tRNA-i) binds to the 40S subunit upon start AUG codon recognition; 2) elongation, where peptide bond formation occurs upon selection of the correct cognate tRNA; 3) termination, which triggers the nascent chain release upon encountering the stop codon; 4) recycling, where 80S splits up to deliver individual subunits back into the cycle. Overview of the pathways that are inhibited upon binding of small molecule drugs presented in this review.

Inhibitors targeting the 60S ribosomal subunit.

The Large Ribosomal Subunit is the site of peptide bond formation. This reaction happens in the peptidyl transferase centre (PTC) and it requires the aminoacyl-tRNA and peptidyl-tRNA to be properly accommodated in the A- and P-sites. Upon peptide bond formation, the newly polypeptide chain elongates and finally protrudes out from the peptide exit tunnel (PET). Once discharged, the deacylated tRNA moves further towards the E-site and, through concerted movements of the L1-stalk, it is allowed to exit the ribosome. Interfering with the rearrangement of the Large Ribosomal Subunit can lead to the arrest of its catalytic effect, thus blocking protein synthesis.

Molecules binding to the A-site

Inhibitors targeting the LSU A-site are responsible of structural rearrangements in their vicinity propagating up to 15 Å away from their binding site (Yusupova and Yusupov, 2017). Once bound, these molecules impede the entrance of the upcoming aminoacyl-tRNA into the A-site. This mechanism involves the steric encumbrance between the amino acid moiety of the charged tRNA and the molecule itself (figure 8). Alkaloids are a broad class of compounds binding to the A-site cleft of the PTC of ribosomes in a life domain-independent manner (Garreau de Loubresse et al., 2014). Despite the common binding pocket on the LSU, molecules belonging to the Alkaloids family of compound differ in their interaction within the A-site pocket rising differences in their kinetic behaviour and in translation inhibition (figure 8). The secondary metabolite from vegetal origins HHT is of particular interest not only for its recent approval in the treatment of myeloid chronic leukaemia resistant to tyrosine kinase inhibitors, but also for its impact on the growth of triple negative breast cancer (TNBC). The antiproliferative pathway involves a strong reduction of TNBC survival factor and the anti-apoptotic protein Mcl-1 levels. The down regulation of several other anti-apoptotic proteins, Bcl-2, survivin and XIAP, was also reported in TNBC cell lines. Weaker evidences to be further investigated suggest the efficacy of this molecule also in vivo mice models, making the search of new congeners of vital importance for the survival rate of patient with this diagnosis (Pak et al., 2021). The first crystal structure of the eukaryotic 80S ribosome in complex with HHT was solved in 2014, revealing that the Homoharringtonine cephalotaxine scaffold, different from the more usual methylenedioxy-phenanthridine skeleton found in other alkaloids, interacts with the 25S rRNA, specifically with the conserved residues A2820 and C2821 (A4366 and C4368 in Homo Sapiens) (figure 8). HHT possesses an ester substitution that points

towards the P-site, creating an electrostatic interaction with the “flipped-up” conserved rRNA residue U2875 in human C4452. (Figure 8). The binding mode of several different *Amaryllidaceae* alkaloids (AA) have been discovered by Garreau de Loubresse and Pellegrino and co-workers. Molecules such as narciclasine (NAR), lycorine (LYC), Agelastine A (AglA) and haemantamine (HAE) have been solved. AAs are natural occurring molecules extractable from different *Amaryllidaceae* species. These compounds share a common chemical core and have been shown to inhibit cancer cell growth by halting protein synthesis (Evidente et al., 2009; Nair and van Staden, 2021; Pellegrino et al., 2018). Narciclasine (NAR), was first characterized as a secondary metabolite extracted from bulbs of several *Narcissus* species and it has been studied for its antitumor, anti-inflammatory, and several other therapeutical activities (Fuchs et al., 2015; Julien et al., 2017). Narciclasine has proven its value in the fight against cancer displaying a broad cytotoxicity activity against multiple cancer cell lines in the NCI-60 (US National Cancer Institute) human tumour cell lines database. In several previous works NAR has been shown not only to inhibit protein synthesis targeting the PTC but as well interacting with eEF1A in melanoma cells, activating Rho pathways, provoking stress fibers in degenerated cerebral glia cells, and regulating the AMPK-ULK1 axis in TNBC cells (Fürst, 2016; Gopalakrishnan et al., 2020; Lefranc et al., 2009). The beautiful bush *Clivia Miniata* studied during the sixties by Jimenez and colleagues is one of the sources of Lycorine, alkaloid carrying several different anti-tumour activities (Roy et al., 2018). Starting from that pioneer work several other studies have been conducted discovering anti-neoplastic pathways in which LYC is involved. Notably Lycorine is active against tumour xenograft and it inhibits the tumour proliferation in B16F10 melanoma-bearing mice, HL-60 xenografted SCID mice, ovarian cancer Hey1B bearing nude mice, and multiple myeloma (MM) cell xenografted NOD/SCID mice (Kim et al., 2015; Roy et al., 2018). In the last years Haementamine (HAE), another natural AA product has ignited the interest spark for its anti-cancer activity (figure 8). It has been firstly show by Pellegrino and colleagues that this natural extract is not only active against several cancer cell lines thanks to its translation inhibition properties, but also via stabilization of the tumour suppressor p53 protein in solid tumour as the colorectal carcinoma (Pellegrino et al., 2018). Further studies focused on chemical modifications of the Haementamine scaffold, showing how we can target different tumour cell types with HAE congeners. From plants to animals’ alkaloids are a big basin of inspiration for anticancer research. The case of Agelastine A (AglA) shows us how evolution can

select and modify molecules that can be of enormous help in medical chemistry. Isolated from the sea sponge *Agelas dendromorpha*, AglA is a brominated member of the pyrrole-2-aminoimidazole alkaloid family active against a number of cancer cell lines. It is important to mention its good permeability for the blood-brain barrier spotting the possible use against cerebral tumours particularly difficult to reach in pharmacological ways (McClary et al., 2017). Its molecular mechanism of binding along with its function was successfully elucidated only in the last years (McClary et al., 2017). In vitro studies demonstrate the ability of AglA to repress cancer proliferation and it has been biochemically proven that it does so by interfering with the elongation step of translation. Upon binding AglA promotes the slight rotation of the rRNA residue A2820 towards the B ring of the drug to form another π - π stacking interaction (figure 8). In addition to π -stacking interactions AglA is furtherly anchored to the A site cleft of the LSU via a poorly characterized halogen- π interaction established between its bromide group and the nucleobase of U2875 (figure 8). As already introduced previously, alkaloids interact directly with the PTC within the LSU, despite this fact some remarkable differences in the position of the dioxolan moiety with regard to the A-site cleft can be highlighted. HHT and NAR have their dioxolan moiety facing the rRNA residue C2821 allowing the connected six membered aromatic ring to engage in a π -stacking interaction with the nucleobase, in the case of LYC the main scaffold assumes a 90 degrees rotate conformation establishing a different hydrogen bond pattern losing the dispersion interaction (figure 8). Haementhamine binds the yeast 80S ribosome in closely related way to Narciclasine. The two compounds provoke a similar movement of A2820 and C2821 toward the inner part of the pocket, allowing the methylenedioxy-phenanthridine moiety to interact with the rRNA residue C2821. In spite of their different origin HAE, AglA and Anisomycin (a translation inhibitor from bacterial origin showing synergic effects if couple with other cancer treatments) induce the same conformational rearrangement of a conserved rRNA residue, U2875 (U4452 Homo Sapiens), which adopts an extended “flip-up” position. Once inhibitors bind the PTC, the formation of π -stacking interactions between their aromatic ring and U2875 is transversal. The intermediate rearrangements of U2875, as well observed with other alkaloids targeting this pocket, suggest the stabilising role of such nucleobase in the accommodation of different molecules within the binding site (figure 8). The A-site cleft is not only known to accommodate alkaloids members, but also some members of the mycotoxin’s family, like Verrucarin A, deoxynivalenol and T2-toxin. These metabolites of fungal origin sit

in a very similar way as the previously described inhibitors (figure 6, figure 8). Similarly, to members of alkaloids, these toxins promote the displacement of U2875 residue, although not as dramatic as HAE and AglA, preparing the pocket to new compound-specific interactions. As suggested by their names, this class of molecules is extremely toxic and dangerous for humans and animals to the extent that their interest in oncological research does not involve their activity against cancer proliferation but rather their ability of favouring its development. The specificity of these inhibitors towards eukaryotic ribosomes most probably rises from the very minor, yet indispensable, differences in sequence with bacterial ribosomes on which they bind with a lower efficacy. This effect seems to be caused by the steric clashes between the rRNA in the bacterial peptidyl transferase centre and the mycotoxins' scaffold. Their hazardous nature must not discourage the research about their structure that could, with the rational design of functional groups, become a valid platform for drug development.

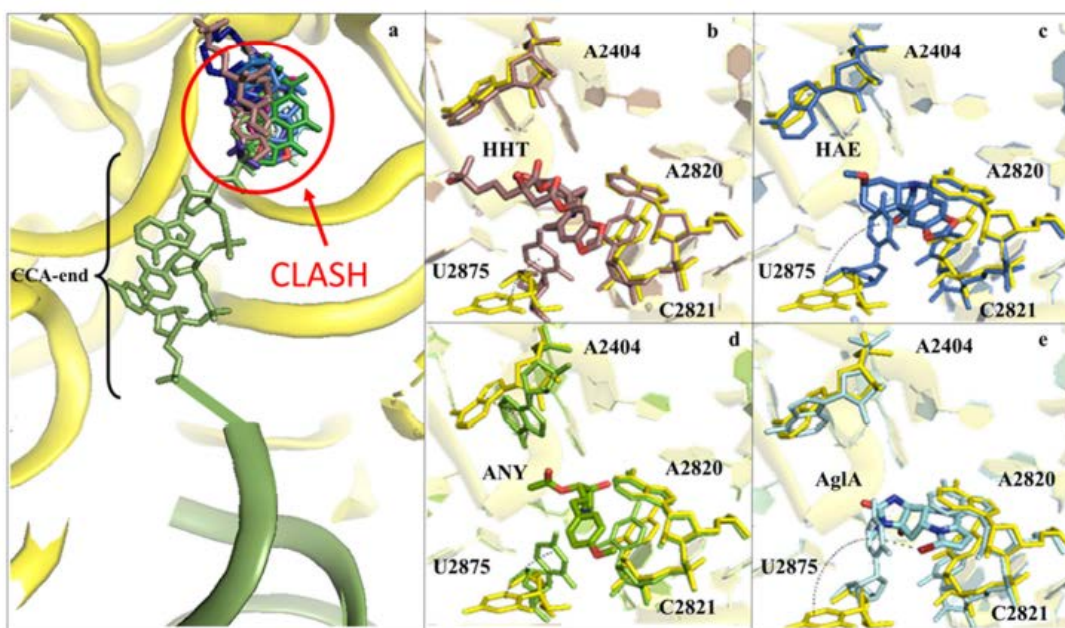


Figure 8 Inhibitors binding to the A-site cleft impede the binding of the aa-tRNA during elongation. Adapted from Pellegrino et al a) Overview of the inhibitors that bind to the A-site cleft. All compounds would sterically clash with the incoming charged acylated A-site tRNA, thus impairing accommodation of the correct amino acid within the pocket and therefore halting the elongation phase of translation. Anisomycin (ANI) in lemon (PDB: 4U3M), Agelastatin (AglA) in cyan (PDB: 5MEI), Deoxyvalenol in fuchsia (PDB: 4U53), Haemanthamine (HAE) in blue (PDB: 5ON6), Homoharringtonine (HHT) in brown (PDB: 4U4Q), Lycorine (LYC) in light blue (PDB: 4U4U), Nagilactone C in aquamarine (PDB: 4U52), Narciclasine (NAR) in green forest (PDB: 4U51), T2-toxin in purple (PDB: 4U6F) and Verrucaric acid (V) in blue navy. b) Zoom-in and details of interaction for HHT within the A-site cleft. Proximal rRNA residues are shown as sticks. c) Zoom-in and details of interaction for HAE within the A-site cleft. d) Zoom-in and details of interaction for ANI within the A-site cleft. e) Zoom-in and details of interaction for AglA within the A-site cleft. The rRNA residues that adopt different conformations upon binding of the inhibitors, A2404 and U2875, are shown for clarity. The peculiar halogen- π interaction established between the pyrimidine ring of U2875 and the bromine atom of AglA is also highlighted.

Molecules binding to the Peptide exit tunnel

A very well-known class of bacterial translation inhibitors is the macrolide class of compounds. They are known to stall translation by obtruding the peptide exit tunnel and they have been used for decades in the fight against bacterial infections. Recent studies underlined not only their action as a plug-in-the-bottle tool, but also their ability to selectively stall specific nascent chain sequences (Vázquez-Laslop and Mankin, 2018). The needed revision of macrolide mode of action suggested that the selective inhibition of a certain pool of proteins was achievable as well for eukaryotic systems (Li et al., 2020). The beneficial effect of such an inhibition pathway in the fight against malignant cellular hyperproliferation had just started to be explored. A recently identified compound named PF846 has been shown, using a library-based randomization, to perform such task. This compound has the capability of specifically inhibit the translation of a protein convertase called subtilisin/kexin type 9 (PCSK9). This protein has been hypothesized to be involved in several types of solid tumours thanks to its action on anti-apoptosis pathways (Bhattacharya et al., 2021). The PF846 mode of action involves the stalling of actively translating human 80S ribosomes almost immediately after the PCSK9 signal sequence recognition (figure 9) (Li et al., 2020, 2019; Liaud et al., 2019; Petersen et al., 2016). The hypothesis is that PF846, upon the recognition of sequence-specific motifs, successively binds them altering their structural arrangement within the nascent chain (NC) of specific proteins. The blockage of the ribosome in a conformational state would inhibit the function of the eukaryotic elongation factor 2 (eEF2) along with mRNA and tRNA translocation. The cascade of conformational changes induced in the PTC and PET regions seems to also affect the release of the polypeptide chain, interfering as well with the translation termination step. PF846 establishes a dense network of interactions with the rRNA environment in the peptide exit tunnel. Notably, it gets in touch with the universally conserved residue A1588 with which interacts via the peculiar halogen- π stacking interaction that the chlorine atom of PF846 bears on its six membered aromatic moiety. This rather uncommon chemical bonding, already observed in case of the bromide bearing AglA, has recently rise interest for its promising implications in drug functionalization (figure 9). The upper mentioned aromatic ring forms an additional π - π dispersion interaction with the universally conserved uracil 4525 (U2609 in bacteria) (figure 9). Despite the rather complex chemical structure of PF846, only its pyrimidine group seems to interact with the NC. The peptide exit tunnel possesses

some features in common between eukaryotes and prokaryotes, in spite of this evidence, the 6-members cyclic ring of PF846 would sterically clash with the bacterial post-translational modified G745, residue that in eukaryotes is mutated and conserved in the form of a cytosine (C1581 specifically in humans). In addition to this guanosine 1582 in the human is replaced by and adenosine in bacteria. The adopted conformation of this particular residue would make the binding of PF846 unfavourable in the bacterial PET. These crucial differences in nucleotide identity and orientation are a probable explanation of PF846's specificity for eukaryotic translational machinery (Li et al., 2019).

Molecules binding to the P-site

The binding into the P-site within the large ribosomal subunit is not a common mode of function of small molecules targeting the protein synthesis machinery, only one class of antibiotics active against gram positive bacteria showed such behaviour : the group A streptogramins. They have the tendency to occupy both the A-site cleft and the P-site within the PTC impairing the peptidyl transferase reaction (Lin et al., 2018).. The ranks of molecules showing this behaviour are fleshed out by the broad-spectrum protein synthesis inhibitor Blasticidin S (BlaS). Contrarily to the previously described inhibitors, BlaS integrally interacts with-in the P-site of the LSU, contacting important residues known to be involved in the establishment of the peptide bond (figure 9) (Arenz and Wilson, 2016; Garreau de Loubresse et al., 2014; Powers et al., 2021). BlaS binds in a very similar manner both to eukaryotic and prokaryotic ribosomes putting in place a very well conserved network of interactions within the P-site, for this reason a shared mechanism of translation inhibition among different kingdoms of life is hence suggested. BlaS is not studied as intensively as alkaloids as a potential cancer treatment. Nevertheless, Blasticidin is broadly implied in cancer research, particularly in the selection of cells carrying genes that give resistance to this particular antibiotic. Evidences coming from the analysis of the BlaS in complex with the yeast 80S ribosome from Garreau de Loubresse and colleagues, show how the BlaS pyrimidine moiety engages in a base pairing interaction with respect of the facing G2619 residue, while the β -arginine peptide moiety gets in touch directly the phosphate backbone of residues A2969 and C2970 (figure 9) (Garreau de Loubresse

et al., 2014). These evidences have been complemented with recent knowledge coming from cryo-EM reconstructions of *in vitro* reconstituted pre-termination 80S complexes in which the presence of BlaS shed light on its inhibitory action in mammals. The reconstructions spotted important differences on the binding of BlaS in higher eukaryotes compared to bacteria counterpart. In fact this molecule induces a more considerable displacement of the CCA-tail of the tRNA accommodated into the P-site (PDB: 4L6J-K-L-M (T. Thermophilus) vs 7NWI (Oryctolagus cuniculus), (Powers et al., 2021; Svidritskiy et al., 2013)) (figure 9). The displacement of the CCA-tail is likely followed by several steric collisions with the incoming substrates into the A-site, notably the amino acylated transfer RNA (during elongation) and eukaryotic release factor 1 (during termination), therefore synergically interfering with both steps of translation. In the stalled pre-termination 80S complex the base pair interaction between G2619 and BlaS is not occurring as in the yeast 80S ribosome, in fact the pyrimidine moiety only partially maintains its hydrogen bond network with G2619.

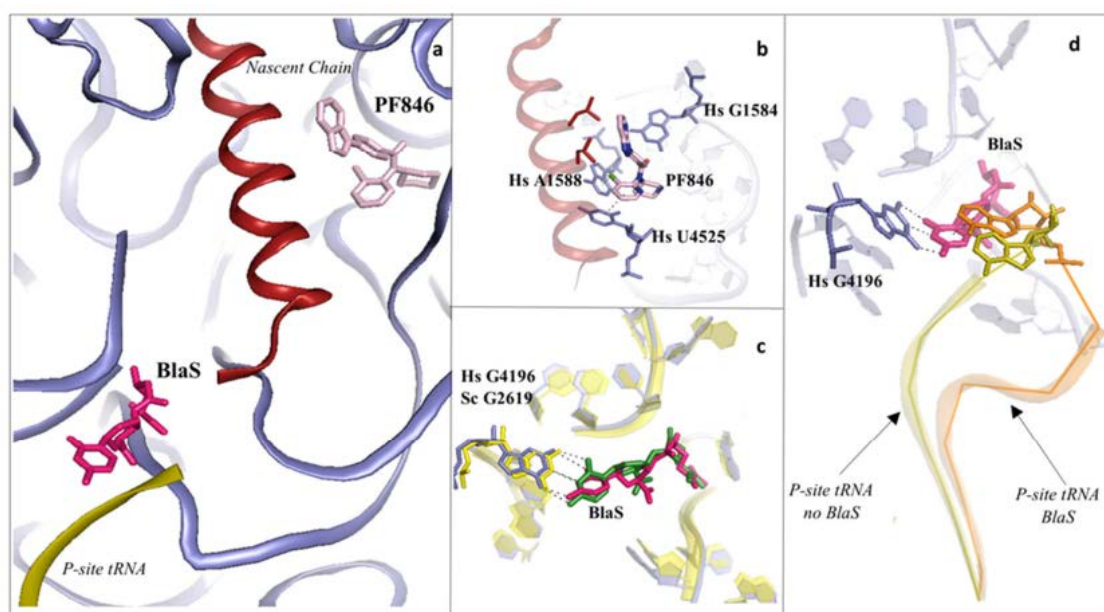


Figure 9 Inhibitors binding to the PTC impair elongation of the nascent chain and can be sequence specific. Adapted from Pellegrino et al a) Overview of the PTC and peptide exit tunnel (PET) of the human ribosome. Blasticidin S (BlaS) in green and hot pink (PDB: 4U56 Sc/7NWI Hs) and PF846 in light pink (PDB: 6XA1) bind within the PTC where the P-site tRNA and nascent chain, respectively, interact with the ribosome. b) PF846 binds to the PET and contacts residues A1588 and U4525 by establishing two different types of interactions, halogen- π and π - π stacking respectively, mediated by the chloride atom. c) Structural superimposition of human and yeast ribosomes solved in complex with BlaS. The conserved residue G4196 (G2619 yeast numbering) establishes a similar hydrogen bonding network with the compound in both organisms. d) Superimposition of translating human ribosome complexes in presence (PDB: 7NWI) and absence of BlaS (PDB: 6XA1). Detail of the displacement of the CCA-end of the P-site tRNA upon binding of the drug, which further promotes an additional π - π stacking with A76, likely preventing the correct accommodation of the tRNA into the PTC. P-site tRNA in absence of BlaS is coloured in olive, while the P-site tRNA in presence of BlaS in orange. Hs: *H. sapiens*.

The induced tilt due to the hydrogen bond lacune favours π -stacking interactions the pyrimidine moiety and the nucleobases A76 of the P-site tRNA offering another stabilization interaction prone to even more strongly impair translocation (Powers et al., 2021).

Molecules binding to the E-site

One of the most known translation inhibitors is Cycloheximide (CHX), broadly used in molecular biology is it often employed to stop translation in several types of eukaryotic cells, from yeast to higher eukaryotes. Unfortunately, due to its low bioavailability and high transversal toxicity towards human cell lines it cannot be directly applied in the fight against cancer. First discovered by Alma Joslyn Whiffen-Barksdale in 1946 and implied as anti-fungal and anti-bacterial it has been furtherly characterized along with another glutarimide compound Lactimidomycin showing their ability to protect specific residues within the E-site pocket in the human embryonic kidney cell line (Schneider-Poetsch et al., 2010). It has been lately proven that the binding site is conserved among eukaryotic kingdom from *S. Cerevisiae* to *H. Sapiens* (Garreau de Loubresse et al., 2014; Myasnikov et al., 2016) with some exceptions in *C. albicans* on which has been lately reported a lower affinity due to punctual modification in the protein environment within the E-site pocket. In this rather recent work, Zgadzay and colleagues attribute the lower affinity of CHX for the 80S ribosome of *C. albicans* to the P-Q mutation in the eL42 known to accompany the exit of the deacyl tRNA from the ribosome (Zgadzay et al., 2022). The E-site is known to accommodate not only glutarimide inhibitors, in the work of Garreau de Loubresse and colleagues along with CHX and LTM also a rather branched molecule called Phyllanthoside has been located with-in the pocket (Garreau de Loubresse et al., 2014) (figure 10). As previously stated, both CHX and LTM carry a common glutarimide moiety establishing the same network of interaction with the 25S rRNA residues, in particular set of hydrogen bonds with the phosphate backbone of G92 and C93 and an additional electrostatic interaction with the nucleobase of U2763 (figure 10), the polyketide linker furtherly interacts with the hydroxyl group with the 25S rRNA (Garreau de Loubresse et al., 2014; Myasnikov et al., 2016). Structurally similar in parts of its structure, LTM possesses an additional 12-membered lactone ring at the extremity of the polyketide tail, LTM is thus considered as member of macrolides. Its lactone ring plays a crucial role in binding affinity of the compound, further establishing interactions with the environment of the pocket (Garreau de Loubresse et

al., 2014). (figure 10). The third compound introduced at the beginning of this paragraph Phyllantoside (PHY), despite no chemical relations to glutarimides, it is shown to bind within the same pocket establishing a network of interactions similar to CHX and LTM. In addition to this behaviour, an interesting interaction between the backbone of the eukaryotic-specific eL42 and PHY is observed (figure 10) (Garreau de Loubresse et al., 2014). The mechanism of action of these three translation inhibitors intimately related to their location on the LSU. In fact, all three molecules sit in a place that in actively translating ribosomes is normally occupied by the deacyl tRNA that during the translocation step of elongation moves from the P- to the E-site. The steric clash between different compounds and the upcoming E-site t-RNA is not eukaryotic specific, it has been already proposed in 2009, when the structure of the 50S subunit of *Haloarcula marismortui* has been solved in complex with the protein synthesis inhibitor mycalamide A, a secondary metabolite from a marine sponge with some growth inhibition effects on eukaryotic cells (Gürel et al., 2009). Despite the intuitive explanation due to their binding sites, CHX and LMT have been proven to show some differences in their inhibition mechanism (Schneider-Poetsch et al., 2010). As already underlined several times during this introduction, nature offers us a wide pool of molecules of enormous interest for their possible applications. A great contribution in this search has been provided by Biard and colleagues that in 1994 published a report in which a new class of molecules from Neo-Caledonian sponges *Lissoclinum voeltzkowi* was identified and chemically characterized (Biard et al., 1994). These molecules were named after the organism that produces them: Lissoclimides. More than a decade after, Robert and colleagues identified the same molecules coming from a different animal, the shell-less molluscs *Pleurobranchus forskalii* able to secrete Lissoclimides to deter predators. In this pioneering work it was demonstrated that these compounds inhibit protein synthesis in vitro and as well as in vivo against mammalian cells. The results from this first assays suggest that Lissoclimides block translation elongation interfering with translocation, forcing an accumulation of ribosomes on mRNA. Mass spectrometry analysis and NMR spectroscopic studies permitted to identify their structural arrangement, underling the presence of chlorine atom borne on the decalin central ring. Advances in chemical synthesis and a renewed interest in natural products interfering with the protein synthesis pushed the VanderWal laboratory to investigate the possibility of obtaining Lissoclimides via total synthesis approaches. Finally, almost thirty years after the first report on this class of molecules the total synthesis approach gave access to the so

called natural occurring Chloro-lissoclimide (CL) and to several of related molecules whose complexes with ribosomes have been biochemically and structurally characterized and their cytotoxic activity assessed against murine leukaemia P388 cell cancer lines (Könst et al., 2017; Pellegrino et al., 2019). The crystallographic structure of the 80S ribosome in complex with CL allowed to decipher the details of interaction of lissoclimides within the E-site binding pocket. As shown in figure 10 lissoclimides possesses a succinimide moiety linked via a small linker bearing an hydroxylic group to the decalin ring. The succinimide ring has the imide scaffold in common with glutarimide inhibitors CHX and LTM, it is not surprising that CL establishes an almost identical network of interactions with the 25S rRNA (figure 10). The hydroxylic group on the linker between the two circular moieties tighten even more the compound within the binding site with an extra hydrogen bond established with the rRNA elements (A2802) and with the backbone of the eukaryotic specific eL42, similarly to PHY (Garreau de Loubresse et al., 2014; Könst et al., 2017). The exciting findings about this new inhibitor are not over yet, the chloride atom identified in the first studies clearly engages in a peculiar and rather interesting halogen- π face on dispersion interaction with the aromatic system of a nucleobase in the 25S ribosomal RNA (figure 10). This kind of interaction has been only recently described for eukaryotic specific ribosome inhibitors, such as the drugs AglA (McClary et al., 2017) and PF846 (Li et al., 2019), while for the prokaryotic system the first report dates several decades ago, in any case none of the reports described this interaction in great details. The total synthesis established in (Könst et al., 2017; Pellegrino et al., 2019) gave access to a wide pool of congeners lissoclimides allowing further investigation of the halogen- π interaction potential, with the ultimate goal of generating more efficient and specific drugs. In vitro studies pointed to a new lissoclimide congeners having a rather low IC₅₀ value ranking it as the second most potent lissoclimide tested: C45, which contains an additional halogen group in its decalin ring. C45/80S complex has been solved with the help of X-ray crystallography, and the contribution of its structure was of enormous help in the validation process of previous *ab initio* docking studies. The theoretical calculations suggested a conformational change in the decalin ring of the compound to better fit into the E-site pocket, which was latterly confirmed by the structural (figure 10). After the decalin ring has adopted a twist-boat conformation, the two chloride atoms on C45 establish a double halogen- π interactions with consecutive nucleobases G2793 and G2794. Conclusions stated the possible influence of the second halogen- π interaction in compensating the loss of other types of contacts,

notably the H-bond pattern established with eL42 observed CL (figure 10). Exploring the role of eL42 in the pocket stabilization process would provide further details and indications on the chemical substitution replacing chloride atoms. The imide containing moieties of CL and CHX constitute a solid platform for drug design and in general a good support for different functional groups that would impede the entrance of the CCA-end of the deacylated tRNA in the E-site (Könst et al., 2017; Myasnikov et al., 2016; Pellegrino et al., 2019).

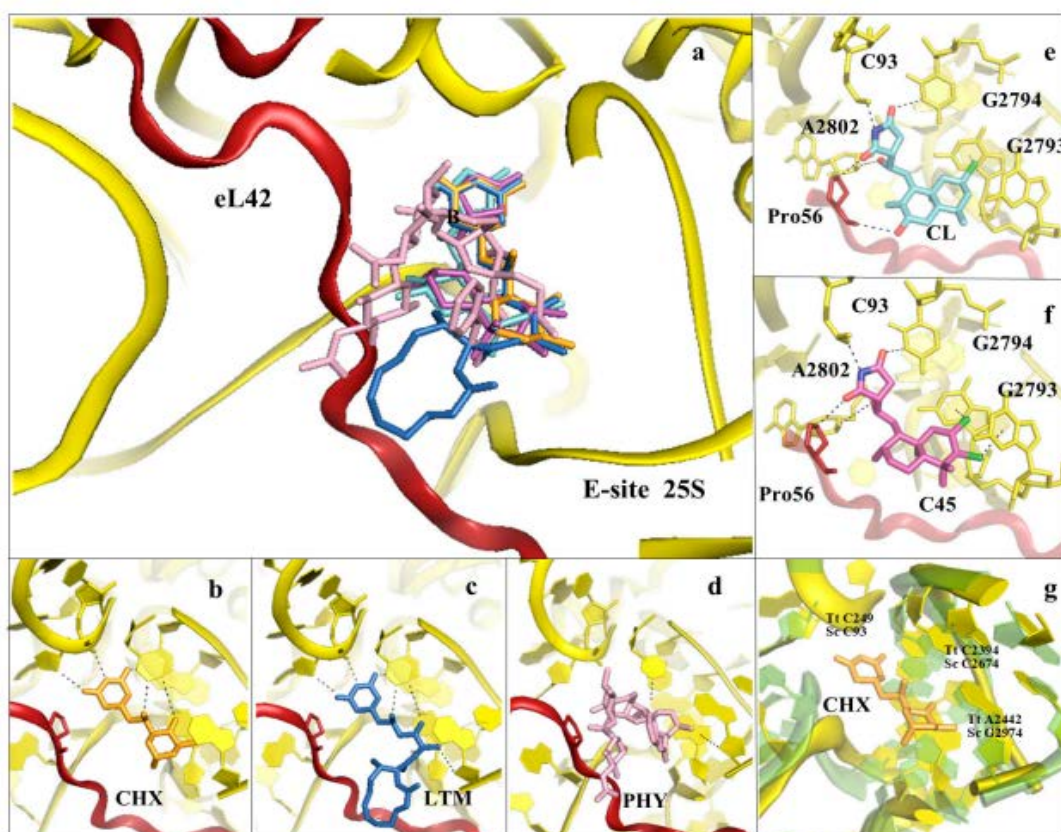


Figure 10 Inhibitors binding to the E-site of the LSU impair the translocation process. Adapted from Pellegrino et al a) Overview of the inhibitors targeting specifically the eukaryotic E-site. Cycloheximide (CHX) (PDB: 4U43) in orange, Lactimidomycin (LTM) in blue (PDB: 4U4R), Phyllantoside (PHY) in pink (PDB: 4U4Z), Chlorolissoclimide (CL) in light cyan (PDB: 5TBW) and the synthetic analogue C45 in magenta (PDB: 6HHQ). b) Zoom-in and details of interaction for CHX within the E-site binding pocket. c) Zoom-in and details of interaction for LTM within the E-site binding pocket. d) Zoom-in and details of interaction for PHY within the E-site binding pocket. PHY, in contrast to CHX and LTM, is reported to interact directly with the eukaryotic specific ribosomal protein eL42. eL42 is colored in red for clarity. e) Zoom-in of CL interaction network within the E-site, with details of the hydrogen bonding and the peculiar halogen- π interaction that lissoclimides establish with rRNA residues. Additionally, CL interacts with the backbone of eL42. F) Same view for C45, which highlighted the second halogen- π interaction that the drug establishes with the rRNA. This additional bond might compensate for the lack of the hydrogen bond with eL42, as it occurs with CL. In both images the type of bonding established between the drug and the ribosome is marked. g) Structural superimposition of the *S. cerevisiae* LSU (coloured in yellow) with the LSU of *T. thermophilus* (coloured in light green) (PDB: 4V5D) (rmsd 4.5 Å). Number of residues for the two organisms are shown (Sc: *S. cerevisiae*, Tt: *T. thermophilus*).

Inhibitors targeting the 40S ribosomal subunit

The role of the SSU in translation initiation and mRNA scanning is very well known and nowadays object of accurate studies, both from the structural and the biochemical point of view. The 40S subunit ensures the appropriate decoding of the genetic information throughout the elongation phase. Being a such important part of the translational machinery, different regions where inhibitors have been identified and explored. To summarise the discussion on molecules targeting the LSU will be divided in two: those binding to the mRNA path and those binding to the decoding centre (DC) (Figure 6).

Molecules binding to the mRNA path.

In the last decade several small molecules involved in translation inhibition have been found to bind the mRNA path, it is worth to mention them and explain their binding mode within the SSU. The X-ray structures of cryptopleurine (CRY), pactamycin (PAC), edeine (EDE) and Amicoumycin (AMA) in complex with the 80S ribosome revealed that these drugs bind to the 18S rRNA. They all bind to a conserved part on helix h23 within the SSU E-site (Garreau de Loubresse et al., 2014) (figure 11), this structural component of the 40S is known to contact the mRNA and tRNA during elongation. The molecular basis of inhibition triggered by Edeine, Pactamycin and Cryptopleurine has not been fully explained yet. Some clues on their mechanism, especially for Cryptopleurine and Pactamycin, come from biochemical characterization demonstrating that PAC and the eukaryotic specific CRY both hamper translocation during the elongation step of translation (figure 11) (Bucher and Skogerson, 1976; Dinos et al., 2004; Dölz et al., 1982). The specificity of Cryptopleurine for the eukaryotic ribosome might be due to the extensions present on the eukaryotic, but universally found uS11. In the yeast ribosome models this protein protrudes within the binding site of CRY and PAC, participating in the binding of the inhibitors. Early crystal structures of the bacterial translational machinery placed the broad spectrum Edeine within the small subunit, this feature is conserved in eukaryotes as well with a shift in the position of the compound within the 40S. In structures derived from the bacteria system, Edeine is found to accommodate in a region between the P- and E-site of the 30S subunit impairing the binding of the initiator tRNA and thus interfering with translation initiation (Dinos et al., 2004; Pioletti et al., 2001). Differently, when visualized on eukaryotic models' organisms, Edeine binding site has

been found to be located the E-site region in the small subunit. The compound interacts with rRNA residues within the mRNA pathway in its final region (figure 11). Biochemical evaluation of Edeine behaviour in actively translating systems indicates that Edeine interaction might provoke continuous scanning and consequently interfering with subunit association (Pioletti et al., 2001). Differences between the prokaryotic and the eukaryotic Edeine mode of binding suggest that their inhibition mechanism could differ to some extent. The biochemistry, on the other hand confirms that this compound indeed impairs translation initiation in the two domains (Kozak and Shatkin, 1978). In the sake understanding and exploring the potential use of inhibitors binding the small subunit with the prospective of future anticancer applications, is fundamental to discuss about Amicoumacin A (AMA). Amicoumacin A interacts with 18S rRNA residues in h23-24 and shown to hinder cancer cell growth slightly more than what it does in healthy cells. Its cytotoxicity has been determined against the MCF-7 breast cancer cells, the A549 lung cancer cells, and two cell lines

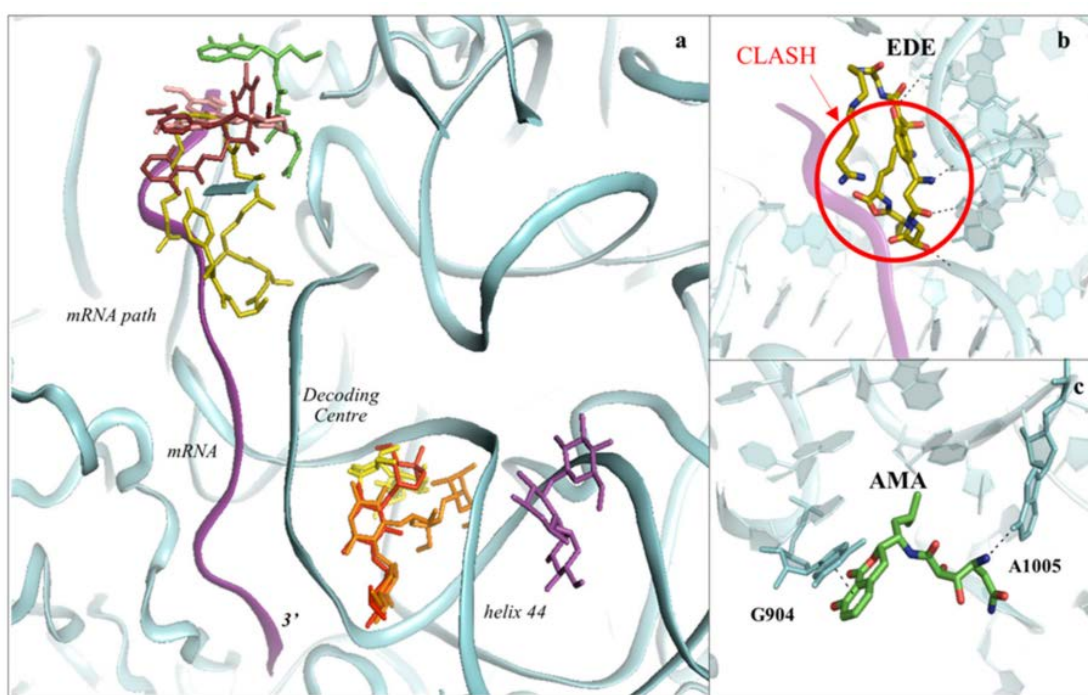


Figure 11 The SSU can be targeted by protein synthesis inhibitors at two main regions. Adapted from Pellegrino et al a) Overview of the binding sites for small molecules binding to the 40S subunit. Amicoumacin A (AMA) in green (PDB: 5I4L), Cryptopleurine in salmon (PDB: 4U55), Edeine (EDE) in olive-green (PDB: 4U4N) and Pactamycin (PAC) in ruby (PDB: 4U4Y). mRNA is also shown as a ribbon and colored in purple. Inhibitors have been shown to bind with high specificity to the mRNA path and the decoding center (DC), thus impairing tRNA-mRNA translocation and altering the translation fidelity process. b) Zoom-in and details of interaction for EDE within the mRNA path in correspondence of where the E-site tRNA should interact. The clash with mRNA (shown in red) would prevent the formation of the pre-initiation complex. c) Zoom-in and details of interaction for AMA within the mRNA path. AMA forms π - π stacking interaction with the conserved rRNA residue G904, while hydrogen bonding with the conserved A1005 (shown as dashed lines).

of non-cancerous (HEK293T embryonic kidney and VA13 lung fibroblast cell lines). Despite its effectiveness against cancer proliferation and the find of its binding site on the 40S ribosome small subunit, it has been postulated that the translational machinery is not the primary target of Amicoumacin A in mammalian cells (Prokhorova et al., 2016). The selectivity of AMA is not very high but, once more, its properties as an anti-cancer chemical might be a good starting point for further developments of new more effective congeners.

Aminoglycosides bind to helix 44 in the Decoding Site.

The decoding centre is the pocket designed by evolution to ensure translation accuracy. It does so via the inspection of the correct pairing of codon-anticodon interaction to allow accommodation of the cognate aminoacyl-tRNA into the SSU A-site. The role in translation fidelity played by the decoding centre makes it one of the main sites where

small molecules inhibiting translation can effectively bind. Aminoglycosides are an example of paramount importance because of their wide use in the treatment of bacterial infections. (figure 6-11-12) (Krause et al., 2016). In prokaryotes, this class of antibiotics binds with high affinity to the decoding centre, influencing translation accuracy at both sense and stop codons, yielding to an extensive translational misreading; furthermore they perturb tRNA translocation by inducing conformational changes in the conserved nucleotides of the decoding centre (Dabrowski et al., 2018; Feldman et al., 2010; Prokhorova et al., 2017; Tsai et al., 2013). Aminoglycosides possesses different affinities for ribosomes belonging to different domains of life. Notably, they are more affine to the procaryotic ribosome than to the eukaryotic cytosolic one. The situation is different for the mitochondrial and chloroplast ribosomes due to the similarity with their bacterial counterpart. The question whether or not aminoglycosides could effectively bind the eukaryotic decoding centre had multiple step in its answer. In the pioneering work on translation inhibitors from Garreau de Loubresse and colleagues a first clue of their presences in the decoding centre was discovered, but due to the competition between this class of antibiotics and the Osmium Hexamine present in post crystallization treatment it was not possible to fully characterize their binding mode. Three years after the first hint, thanks to a scrupulous optimisation of post-crystallisation conditions, Prokhorova and colleagues unveiled for the first time the molecular details of four aminoglycosides binding mode,

respectively G418 (geneticin), paromomycin (PAR), gentamicin (GENT) and TC007 (figure 12) (Prokhorova et al., 2017). The brilliant idea consisted in the exchange of the heavy metals present in the post crystallization treatment with the aminoglycosides object of the study, with the hope that the similar unspecific affinity of osmium hexamine and aminoglycosides for the phosphate backbone of rRNA would have provoked the same subunit rotations that allowed the vacant yeast 80S crystal form to diffract at high resolution. The idea was successful. In the crystal structure of the 4,6-linked aminoglycoside G418 in complex with the *S. cerevisiae* 80S ribosome, this particular aminoglycoside has been shown canonically accommodate within the h44 decoding site, as it previously shown in presence of heavy scatterers (Garreau de Loubresse et al., 2014). Ring I of G418 directly contacts the eukaryote-specific residues G1645 and A1754 forcing the conserved nucleotides A1755 and A1756 to “flip-out” the internal loop of h44 (Prokhorova et al., 2017). The authors of this work solved as well the 4,5-linked aminoglycoside paromomycin spotting out a similar behaviour of rings I and II when compared to the same rings of G418 (figure 12). However, when compared with the prokaryotic counterpart differences in the orientation of the third ring can be observed. This moiety results rotated, probably to prevent the steric hindrance with the residue A1754 common to eukaryotes. Ring IV reorients within the major groove of h44 (Prokhorova et al., 2017). In addition to the usual network of interaction another difference compared to the prokaryotic system was observed. In fact, ring I of PAR seems to engage in a hydrogen bond with lysine-3 of eS30, which comes near h44 from the minor its groove. Authors stated that this extra bridge with eS30, not observed when G418 binds to the same pocket, could in principle compensate for the lower affinity for the eukaryotic h44 decoding site, thus maintaining the levels of miscoding low (Prokhorova et al., 2017). A broadly used aminoglycoside to fight bacterial infection is Gentamycin, this three-ring membered 4,6-linked aminoglycoside has been shown to bind the eukaryotic 80S yeast ribosome in addition to the prokaryotic counterpart. The structural studies conducted on GENT/80S complexes place the functional binding site of this small molecule within helix44, similarly to the already described aminoglycoside molecules but showing instead a peculiar mode of interaction not common to the aminoglycosides previously described (figure 12). Contrarily to ring I of Paromomycin and G418, ring I of gentamicin does not interact with the conserved residue A1754, in addition the two decoding nucleotides A1755-A1756 adopt a not fully flipped conformation with respect the axis of h44 (figure 12). Remarkable interactions of rings I–III of gentamicin

with U1758 and G1642 were also reported. In the workflow of deciphering the binding of aminoglycosides on the eukaryotic ribosome using the yeast 80S as a model, the structure of TC007 has been solved unveiling that this other three ring membered aminoglycoside does not lay on the decoding site on h44. Surprisingly, the binding site was identified above h44, in a region in proximity of the joints between the small and the big subunit where an inter-subunit bridge is formed with h71 from the LSU. Another curious fact about this molecule is the difference between its binding site on the prokaryotic ribosome and the previously discussed eukaryotic. TC007 sits in the canonical aminoglycoside pocket when in complex with the bacterial ribosome, the tip h44. Ring I and II adopt a pose close to the paromomycin one (figure 12) (Prokhorova et al., 2017). This last comparison between prokaryotic and eukaryotic aminoglycoside mode of binding allowed the authors to hypothesise the reason why aminoglycosides show domain specific features for their binding on ribosomes. In close proximity to these two conserved adenines involved in the decoding process, evolution has diverged and as a result position A1408 and G1491 in bacteria are replaced into, respectively, G1645 and A1754 in *S. Cerevisiae* (conserved also in humans). Probably, the change of an adenosine for a guanosine at position 1754 would not allow the Watson–Crick base pairing with C1646, fundamental interactions for aminoglycoside binding to the 80S ribosome (Garreau de Loubresse et al., 2014). These sticking dissimilarities can be crucial for accommodation of aminoglycosides within the DC, giving a possible explanation for the discrepancy in binding affinity between domains of life. Furthermore, TC007 has been shown to play an active role in the dynamics of subunit rotation as an alternative mechanism of inhibition (Prokhorova et al., 2017). A plethora of terrible medical conditions including cystic fibrosis, Duchenne muscular dystrophy, β -thalassemia, and many types of cancers are caused by the encounter of premature stop codons in messenger RNA. The presence of premature stop codon can be due to different causes, as result of mutations within germline or somatic DNA, inaccurate or inefficient pre-mRNA splicing, or improper RNA post translational modifications. Around 10-12 % of mutations involved in these medical conditions arise from single point mutations finally resulting in a premature stop codon. If we consider the other sources of premature termination codon encountering, we can estimate that almost 30% of genetically transmitted disorders are caused by this translation failure, cancer included. When a premature stop codon is encountered, the growing polypeptide chain is released without part of the amino acids supposed to be in its primary structure, with catastrophic consequences of the three-dimensional rearrangement of the protein.

Usually these kind of conditions have a worse prognosis than other genetical diseases, because they lead to the complete loss of function of the protein synthesized (Popp and Maquat, 2018; Wagner et al., 2001). Aminoglycosides are studied for their ability to partially re-establish normal rates of protein synthesis in models carrying genotypes associated to PTeC diseases. Several practical examples can be given. Spinal muscular atrophy (SMA) is a genetic disease associated with the loss of full-length Survival Motoneuron proteins causing different medical conditions in new-borns a children (Mattis et al., 2012). Early screenings for drug-induced suppression therapies identified in TC007 a promising hit (Mattis et al., 2006). Tests in SMA mouse models showed a prolonged lifespan accompanied by tolerable toxicity profiles (Mattis et al., 2012; Prokhorova et al., 2017). Other aminoglycosides along with TC007 have been shown to promote misincorporation of near-cognate aminoacyl-tRNAs in case of premature termination codons encounter (Chowdhury et al., 2018). For this reason, treatments designed to force the ribosome to ‘read-through’ a when a premature stop codon enters the mRNA path seems to be a valid tool to alleviate these medical conditions. Unfortunately, aminoglycosides possess high toxicity levels for eukaryotic specific cells. They are known to be ototoxic and nephrotoxic potentially leading to harmful side effects (Chowdhury et al., 2018; Dabrowski et al., 2018). Their side effects do not appear to be directly linked to their repercussion on translation but rather to their association with different cellular targets. Within the cell, aminoglycosides bind iron, forming complexes capable of generating reactive oxygen species. These molecular species are highly reactive toward cellular membrane lipids and capable of reaching the nucleus. Once there, they trigger the activation of genes responsible for apoptosis yielding to irreversible cellular damage (Alharazneh et al., 2011). The arrest of the mitochondrial ribosomes is known to be another cause of aminoglycosides side effect. Given the similarities between bacterial and mitochondrial ribosomes, aminoglycosides bind with higher affinity to these last ones rather than to the cytosolic ones. Despite all the upper-mentioned side effects, aminoglycosides have an enormous potential in different applications related to human pathologies. This potential needs to be further explored, and the structural studies performed on this class of molecules are an excellent platform for further improvements (Dabrowski et al., 2018; Keeling et al., 2014).

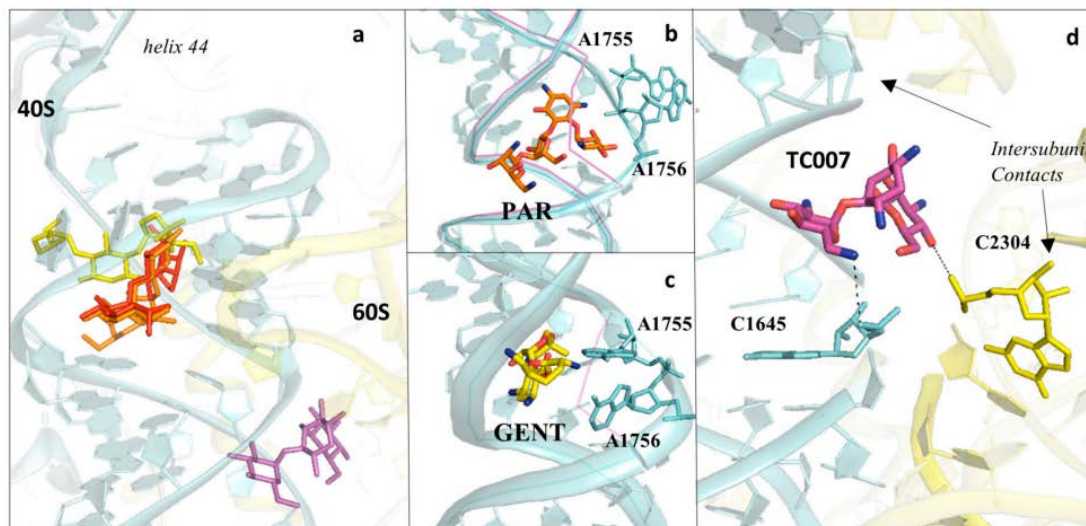


Figure 12 Aminoglycosides bind preferentially to the DC of the eukaryotic ribosome. Adapted from Pellegrino et al. a) Overview of aminoglycosides binding in correspondence of helix 44 (h44) of the eukaryotic SSU. Paromomycin (PAR) in orange (PDB: 5NDV), Geneticin (G418) in yellow (PDB: 5NDG), Gentamicin (GENT) in red (PDB: 5OBM), TC007 in violet (PDB: 5NDJ). b) PAR binds within the minor groove of h44, and promotes “flip-out” of the two conserved adenines (A1755/A1756) towards the mRNA channel. c) GEN binds to h44, but docks in a different way compared to PAR, and induces only partial extrusion of the decoding residues. Vacant ribosome (PDB: 4V88) aligned and shown as a purple line for evidencing the conformational change of the minor groove of h44 upon drug binding. d) Zoom-in and details of interaction for the aminoglycoside TC007. TC007 contacts directly both LSU and SSU, establishing hydrogen bonds with rRNA residues of the 25S and 18S at a specific Intersubunit bridge (B3).

Ribosome Tetramers

From the first days of ribosome structural studies, the question whether or not ribosome particles were crystallizable intrigued the scientific community. When we think about the crystallization process of macromolecular complexes, we think about something artificial and human driven, a process that involves purification steps and the search for the right conditions. Once more, nature itself helped scientists to unveil processes considered as pure speculation and fantasy until that moment. Pioneer studies on the hypothermic effects of low temperatures on chicken embryos, firstly designed to address questions about the behaviour of cytoplasmatic microtubules (Byers, 1966), showed the presence of ordered aggregates of ribosome in the fiber cells of developing chicken embryos. More extensive electron microscope studies revealed that these aggregates had a crystal-like morphology and more precisely identified as thin-sheet of one ribosome thickness. Extensive characterization of embryos exposed to cold stress at different stages of their development showed how in young embryos,

where the rates of translation are enormously elevated (Byers, 1971), the presence of such aggregates was extensive and cell type independent (epidermal and neural ectoderm, mesoderm, and endoderm were characterized by the presence of crystalline sheets). Interestingly, aggregates of just four ribosomes in a square array were discovered and considered to be the unit cell of such para-crystalline aggregates. Fast cooling of explanted embryos yielded no crystals in interphase cells, but stacked crystals were found in mitotic cells, indicating a certain

dependency on the cell cycles. Authors at that time postulated a necessary dissociation from translating polysome prior bidimensional sheet formation (Unwin and Taddei, 1977). Despite the unfavourable conditions coming from cold exposure, eggs undergone this treatment showed a certain level of hatchability with variations

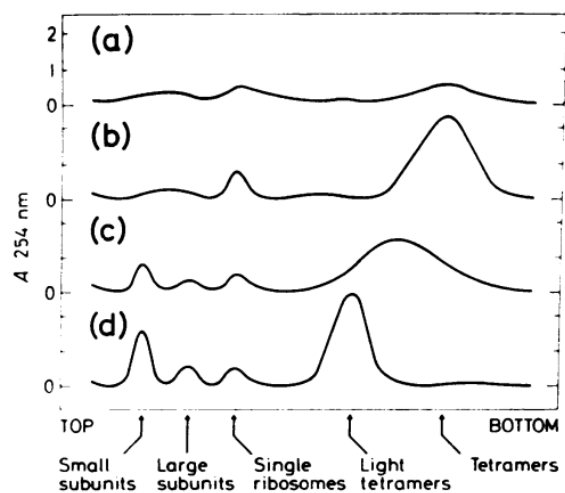


Figure 13 Ribosome sucrose gradient profiles. a) at less than 0.1 M KCl, few tetramers appeared on the gradients. b-c) from 0.15 to 0.25 M KCl, there were significant numbers of tetramers present. d) At 0.30 M KCl and above the presence of a peak of lighter particles can be observed, parallelly a peak in correspondence of the 40S appeared.

depending of the developmental stage the embryos (from 80% in 5 days old eggs cooled for 24h to 60% in 10 days old eggs cooled for 24h). After the first report from Byer, describing this new ribosomal aggregate found in living cells, different groups started to work on this particular issue providing a solid biochemical and biophysical background for further studies. The dependency of tetramers formation on ionic strength condition was extensively assessed in the perspective of recreating in vitro the conditions of ribosome tetramerization. Chicken tetramers proved their resistance to high concentration levels of monovalent cations such as K^+ , and low levels of divalent cations like Mg^{2+} . It has been demonstrated in an elegant experiment that the rise of potassium ions concentration was not the cause of tetramers dissociation. It instead yielded to an accumulation of particles lighter than the standard tetramers but heavier than single monosomes. An increase of the total intensity of 40S particle peak followed the shift in the Svedberg coefficient as shown in figure 13 was reported. Agarose gel analysis of rRNA material extracted from different peaks revealed the presence of the all ribosomal RNA in the standard tetramer and monosome peak, while no 18S was found in the so called 'light tetramer' peak. This result suggested that tetrameric particles were mainly kept together by interactions involving the large ribosomal subunit or a factor binding to it. During these years several biochemical evidences supported the hypothesis that tetramers were formed by standard ribosomes and that it was possible to reconstitute their tetrameric features starting from both ribosomes coming from tetramers dissociation and ribosomes from the 80S gradient peak. The high viability of fertilized eggs after 24 hr of cooling and the fact that degradation products of ribosomes were not detected upon rewarming while polysomes reappeared, suggested that ribosomes within tetramers could reinitiate protein synthesis and, although inactive, were potentially functional (Byers, 1966; Morimoto et al., 1972a). The biological activity of ribosome tetramers was furtherly investigated to determine whether or not these assemblies were capable of active aminoacid incorporation and messenger RNA accommodation. Results from Morimoto and Sabatini highlighted how levels of aminoacid incorporation in tetramers were risible compared to the efficiency of polysomes. The characterization of the effect of different translation inhibitors on ribosome tetramerization was extensively tested. Embryos cooled "in ovo" were treated before cooling with cycloheximide and puromycin in the attempt of understand the levels of protein translation during the cooling event. For this reason, leucine-3H was also added in vivo and the different conditions analysed via sucrose gradient centrifugation. The consequences of RNA-se treatment were also

investigated. Morimoto and colleagues discovered several different characteristics about ribosomal tetrameric aggregates behaviour:

- Cycloheximide administered before cooling hindered tetramer formation almost completely.
- Puromycin added before cooling did not alter the tetramerization process.
- RNA-se treatment did not affect tetramers, while the polysome pick was converted to single monosomes after the treatment.
- Tetrameric particles did not contain nascent polypeptides labelled during cooling..

All these evidences combined made the authors hypothesise that the completion and release of nascent chains during cooling was a needed step for tetramers assembly (Morimoto et al., 1972a, 1972b). The fact that puromycin did not affect the tetramerization process was interpreted as an evidence that protein synthesis was needed only to terminate nascent chains and to release monomers from polysomes, since ribosomes stripped of nascent chains by puromycin and artificially released from polysomes could also form tetramers in vitro (Morimoto et al., 1972a, 1972b). Not all the scientific community agreed with these conclusions, in fact studies from different groups gathered a corpus of evidences concerning the cell cycle dependency of tetramers aggregation, not in agreement with the model proposed by Morimoto and colleagues. In a critic review on the chick tetramer issue, Barbieri and colleagues proposed a different scenario deeply connecting the tetramerization process to the proliferative state in which the cells of a particular tissue were found. In support of this theory, bidimensional sheets of ribosomes were found in chick bone marrow of adult animals. All the hypothesis connected to this evidence were systematically analysed reaching some conclusions: ribosomes able to crystallize were not normal ribosomes but what Barbieri called “primitive ribosomes”. This definition was mainly due to the experimental evidence that microcrystals appeared in the nucleolus as well. This part of the nucleus is the sub-cellular compartment where the pre-r-RNA is transcribed and the subunits start to be assembled with ribosomal proteins. Furthermore a considerable increase of these particles was observed in the nucleoli of cells infected with the Herpes Simplex virus 2, known to induce cellular degeneration in epithelial cells (Barbieri, 1979; Brunelli et al., 1977). If these microcrystals were present in the nucleolus, then also not fully mature ribosome could undergo the tetramerization. Under the light of the almost total absence of tetramers in fully differentiated tissues,

the conclusion was quickly drawn: Ribosome constituting tetramers are in somehow different from those present in fully differentiated cells (Barbieri, 1979; Brunelli et al., 1977).

The success of Morimoto and colleagues in producing planar crystallographic assembly suitable for low resolution analysis moved the research in the direction of in vitro tetramer production. This search finally gave results with the work of Unwin and colleagues. The production of ribosome chick crystals able to diffract up to 50 Å allowed a partial reconstruction of ribosome internal organization and the confirmation the position of the peptide exit tunnel within the LSU as previously suggested by immunofluorescence studies (Milligan and Unwin, 1986).

Research Project 1

*Structural and Biophysical
characterization of small molecules
binding to the Ribosome as a potential
anticancer treatment*

Aim of the project

The interest in the quest of finding inhibitors impairing the translational machinery has risen during these last years. This interest needs to be supported by structural data able to elucidate the molecular mechanism of protein synthesis inhibition (Garreau de Loubresse et al., 2014; Yusupova et al., 2021). The mode of action of different molecules has been proven to influence their selectivity towards certain types of cells. A big part of molecules hindering translation comes from natural sources or it has been synthesized using natural molecules as a starting point. It is the case of lissoclimides, naturally occurring molecules discovered almost thirty years ago and now extensively studied for their chemical and biological characteristics (Biard et al., 1994; Robert et al., 2006). Thanks to the total synthesis approaches developed in the VanderWal laboratory it has been possible to produce congener molecules having the same scaffold of the natural occurring lissoclimide, but carrying different functional groups at different positions (Michalak et al., 2019). The majority of substitutions are halogen atoms replacing the natural occurring chloride, but a C3-methylated lissoclimide has been also produced. The stress will be put on how different halogens influence their binding pockets, providing a structural framework that can be used to explain the observed *in vitro* and *in vivo* effects of these molecules. In the previous chapters we introduced how the lissoclimide binding site is also shared by another class of compounds: glutarimide inhibitors. Gladiostatine is a protein inhibitor produced by a soil bacteria and it has been shown to have an effect on protein synthesis (Nakou et al., 2020). The final aim of this project is to provide structural insights on the different molecules binding the translational machinery, highlighting the differences and describing their similarities. Using biophysical and biochemical approaches this issue has been addressed from several points of view. In the past years the only tool able to decipher the three-dimensional organization of macromolecular complexes at the atomic level was X-ray crystallography. During the last two decades this method allowed the scientific community to make progress in the solution of the bacterial drug resistance issue, a global problem for public health (Blair et al., 2015). The high throughput power of this technique makes it a fast and reliable method even nowadays for drug discovery and design purposes. This well-established method carries many other advantages, for example, the possibility of discerning atoms thanks to their anomalous signature, unveiling their nature otherwise unknown (Rozov et al., 2019).

Furthermore, the solid theoretical background in X-ray makes it a more reliable tool in the discovery of previously unknown binding pockets in macromolecular druggable targets (Yusupova et al., 2021).

Materials and Methods Project 1

Ribosome purification

After synchronizing single colonies of yeast via precultures, the effective biomass was produced overnight in 5L flasks containing 1L of YPDA + Kanamycin at 30°C with constant shaking. The following day the optical density at 600 nm was measured and cells harvested when the value of 1 OD₆₀₀ was reached. In the following step, the cellular pellet is resuspended in the same medium lacking glucose and incubated for ten minutes at

<i>Buffer M</i>	
Compound	Concentration
Hepes (free acid) / KOH	30 mM pH 7.5
KCl	50 mM
MgCl ₂	10 mM
Mannitol	8.5 % (w/V)
EDTA	0.5 mM
DTT	2 mM

the same temperature. The stress triggered by the absence of glucose will induce reversible translation stalling with the consequent release of non-translating 80S ribosomes from translating polysomes. Such treatment allows us to reach the high homogeneity needed for ribosome crystallization. Yeast cells are then recovered by centrifugation and put on ice, ready for the following steps. Collected cells were extensively washed with buffer M in order to remove all media. Clean sample was then resuspended in the same buffer supplied with protease and RNA-se inhibitors. Three grams of glass beads per gram of cells were used in the lysis step performed with the help of a vortex operating at 40 Hz. The Nalgene tube containing cells and glass beads was shaken seven times for one minute with one-minute break on ice to avoid temperature rising. The cell lysate was then centrifugated at 13000 rpm for 10 minutes, separating cell walls and glass bead from the cellular fraction containing ribosomes. The obtained solution was spun for ten minutes at 16000 rpm in order to obtain the S30 fraction. The lipid phase and the debris were carefully discarded and the S30 fraction recovered in a new, clean tube. Ribosomes were purified via several differential PEG precipitations. In the first one the concentration of the precipitant agent was increased to 4.5%, the sample incubated for five minutes and Then clarified at 13000 rpm for five minutes more. The supernatant was recovered in a new tube and the pellet was discarded. The potassium chloride concentration was subsequently adjusted to 130 mM adding the solution very slowly in order to avoid subunit dissociation due to the high local salt concentration.

The second PEG precipitation involved ramp up of its concentration to 8.5%, followed by clarification performed via centrifugation at 12000 rpm for ten minutes. The supernatant was discarded, and the pellet washed and re-dissolved in buffer M+, with the same composition as buffer M but increased potassium chloride concentration (150 mM) and the supplement of protease and RNA-se inhibitors. Ribosome concentration has then been spectrophotometrically measured in triplicates using UV-1900 SHIMADZU spectrophotometer. At this step usually between 45 and 30 mg of ribosomes were obtained (monosomes and dissociated subunits). In order to further purify our 80S ribosome the resuspended pellet was layered onto 10-30% sucrose gradients (composition shown in table 3) and spun for fifteen hours at 18000 rpm. The gradients were fractionated in

<u>Sucrose Gradient Solutions</u>	
Compound	Concentration
Hepes (F.A) / KOH	30 mM pH 7.5
KCl	150 mM
MgCl ₂	10 mM
Sucrose	10%-30% (w/V)
EDTA	0.5 mM
DTT	2 mM
<u>Buffer G</u>	
Compound	Concentration
Hepes KOH, pH 7.5	10 mM
KOAc	50 mM
NH ₄ Cl	10 mM
Mg(OAc) ₂	5 mM
DTT	2 mM

Sucrose Gradient Profile 30%-10%

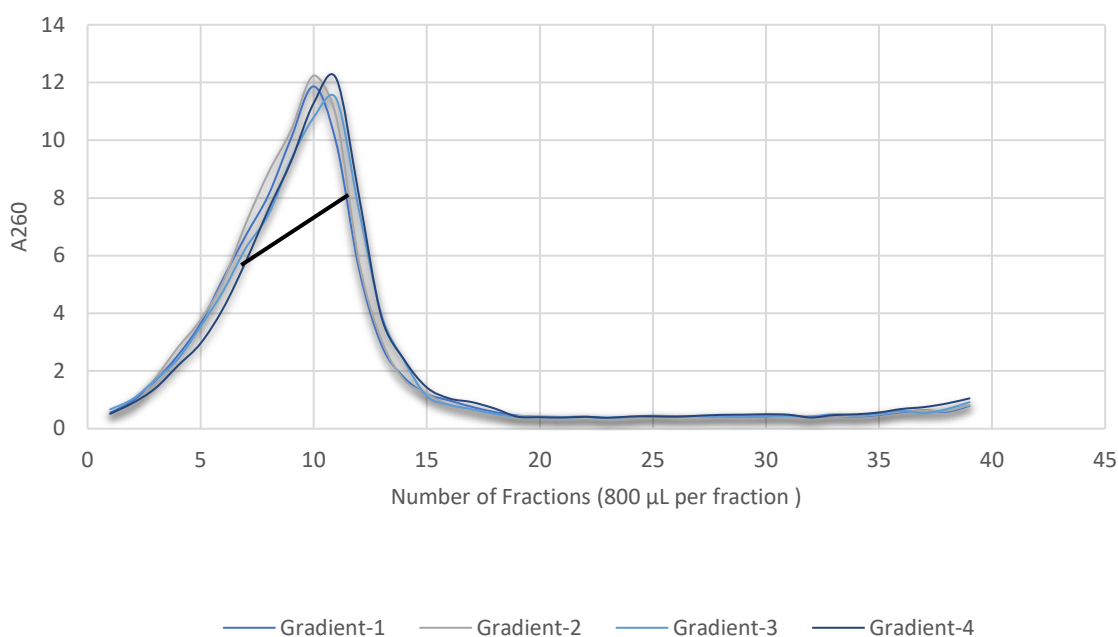


Figure 14 30-10 % sucrose gradient profile of *Saccharomyces cerevisiae* ribosomes measured on Nanodrop. All superimposed gradients have the same features. The black line represents the pooled fractions used in the next purification steps.

forty fractions and the gradient profile measured on Nano-Drop previously blanked with milli-Q water. Selected fractions containing 80S ribosomes were pulled together and the concentration estimated on Nano-Drop (figure 14). The ionic strength was then adjusted to 150/10 mM of KCl/MgCl₂. Ribosomes were ready for the last PEG precipitation. The precipitant agent concentration was brought up from zero to 7% and the sample incubated 10 minutes at 4°C. Ribosomes were then pelleted by centrifugation at 12000 rpm for ten minutes. The pellet was gently re-suspended in buffer G, filtered in 0.22 µm filters and the concentration measured in triplicates on SHIMADZU UV-1900. For crystallization purposes the sample concentration was adjusted with buffer G to 24 mg/ml, aliquoted, flash frozen in liquid nitrogen and stored at -80°C until further use. Protein and RNA contents have been checked with under denaturation conditions using respectively SDS page gel for proteins and agarose gel for RNA (not shown) .

Ribosome crystallization

For crystallization, ribosomes previously stored in buffer G at -80° C were slowly de-frozen and the crystallization mix prepared as follows: Ribosomes in buffer G, were diluted in buffer CD to reach the final concentration of 1.55µM, 2.5 mM Hepes-K pH 7.5, 2.5 mM NH₄Cl, 3.33 mM Mg(OAc)₂, 1.6 mM DTT, 0.055 mM EDTA , 40 mM K(OAc), 5.5 mM NH₄OAc, 5.5 mM Tris-Acetate pH 7.0. According to the co-crystallization protocol, translation inhibitors previously dissolved in DMSO were added to the mix in different ratio as described in the following paragraphs. The ribosome solution was incubated at 30° C for 10 min after which Deoxy Big Chap at 2.8

<u>Buffer CD</u>	
Compound	Concentration
Tris/OAc pH 7.0	20 mM
K(OAc) pH 7.2	100 mM
NH ₄ (OAc)	20 mM
MgOAc	8 mM
DTT	5 mM
<u>Well Solutions</u>	
Compound	Concentration
Tris/OAc pH 7.0	100 mM
KSCN	100 mM
MgOAc	3 mM
PEG20K	3.8-4.4%
Glycerol	20%
Spermidine	5 mM

mM was added and incubated for 10 minutes more at the same temperature. The mix was left to cool down in the cold room prior crystallization. Ribosomes were crystallized in hanging drop plates from Hampton. Drops of 2-2.4 µL of ribosome were mixed with 1.6 µL of the correspondent reservoir solution. Crystals appeared within the first 5 days in the higher 20K PEG range and reached their full size in drops with lower nucleation spots after 20 additional days. Crystals with a minimum size of 200 µm in length were used for soaking and dehydration experiments.

Ribosome Post-crystallization treatments

Crystals of macromolecular complexes carry a significant amount of solvent, enormously affecting the diffraction quality and thus the resolution limit. This intrinsic property has its own advantages. The presence of solvent channels allows small molecules and low molecular weight factors to diffuse into the crystal and interact with the molecular target. An improvement of the resolution limit has been achieved using a modified version of the published protocol (Ben-Shem et

<i><u>Cryo-protection Solutions</u></i>	
Compound	S _n
Tris pH 7.0	80mM
K(SCN)	70 mM
K(OAc)	40 mM
NH ₄ (OAc)	7.5 mM
Mg(OAc) ₂	10 mM
Spermidine	6.5mM
PEG 20000	5%
PEG 6000	1-20 %
Glycerol	20 %
Os(NH ₃) ₆	0-2mM
Inhibitor	-

al., 2011; Garreau de Loubresse et al., 2014). Cover slides were placed in a small Petri dish and ten microliters of the first of four solutions containing 1% of PEG6000 was added to the drop, incubated for ten minutes and removed. Solutions with higher concentrations of PEG6000 were subsequently added, incubated and removed from the drop. The final solution containing 2mM osmium hexamine and different concentrations of different compound was added and removed three times, increasing the incubation period in steps: ten, twenty and sixty minutes. The presence of Os(NH₃)₆, initially intended to be the anomalous scatter used for phasing, showed its crucial role in the achievement of high-resolution structures with this particular crystal form. Its high affinity for rRNA backbone phosphates plays a crucial role in stabilizing the small subunit and allowing a better crystal packing and thus higher diffraction power. From two to five crystals per drop were fished and flash frozen in liquid nitrogen for further diffraction experiments. Crystals were treated under the assumption “one-drop-one-condition”, important for the further step of structure determination (figure 15).

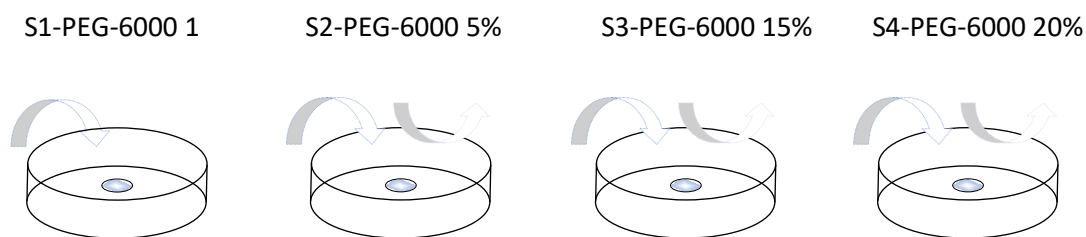


Figure 15 Cryoprotection dehydration and soaking scheme for 80S yeast ribosome crystals.

Slightly different approaches were implemented for different molecules:

- Lissoclimides

80S ribosome crystals in complex with lissoclimides were prepared following the previously described protocol. The dehydration protocol was adjusted according to the methods already applied for this particular class of compounds (Könst et al., 2017; Pellegrino et al., 2019): Different excess of inhibitors was used in the co-crystallization process in order to be able to work with the lowest concentration of compound possible, the maximal tolerated concentration of compound was also reached leading to inhibition of crystallization. Crystallization solutions with an excess of 15 μM , 30 μM , 45 μM , 60 μM and 1000 μM of all six lissoclimides were prepared. Crystals appeared in all condition with a significant decrease in the solution with the highest concentration of lissoclimides. Crystals showing the best morphological appearance were selected for the dehydration experiment. All concentration used in the co-crystallization experiment were kept during the cryoprotection steps.

- Gladiostatine

The strategy for Gladiostatine was different, at first crystals containing an excess of Gladiostatine of 60 μM showed a partially occupied binding site. To solve the structure of the complex, the concentration of GLD was stepwise increased in the cryoprotection step, reaching the final concentration of 1000 μM , crystals at different final concentrations of the inhibitor were fished to find the best condition of Gladiostatine binding, respectively 60 μM , 120 μM , 250 μM , 500 μM , 1000 μM . Crystals appeared to suffer during the hard soaking experiment showing cracks and fissures on their surface in an higher percentage compared with the lissoclimide behaviour.

- Niditine Chloride

Nitidine chloride crystals coming from co-crystallization trials appeared morphologically different from the upper mentioned cases. Lacking sharp edges their stability under dehydration condition was an issue for the success of the experiments.

The most stable crystals were treated until the maximal concentration of Nitidine chloride in the cryoprotection steps of 150 μM . Conditions containing and lacking osmium hexamine were tested, leading to poorly diffracting crystals. Consequently, the binding site of this molecule has not been found. Nitidine Chloride will not be furtherly discussed in the next sessions.

Data-collection and Data Processing

Data on inhibitors were entirely collected at the Swiss Light Source Synchrotron at the beamline PX1-X06SA under the supervision of the beamline staff. After an accurate screening procedure, highly redundant datasets were collected under different co-crystallization and treatment conditions. Up to five datasets per crystal were measured

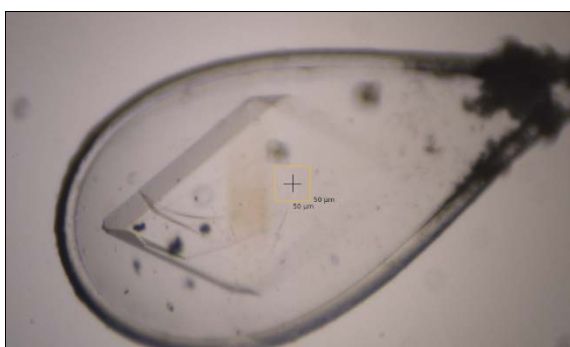


Figure 16 80S yeast ribosome crystals mounted in SLS PX1-X06SA goniometer. The radiation damage dealt by the first data collection left a burn on the crystal visible in figure.

using an ultra-fine-phi-slice approach on EIGER 16M detector. The association of fast frame rates and a micro-second dead time allows EIGER 16M detector to acquire high-quality data in a reasonable short time, from fifteen to thirty minutes for ribosome crystals. The ultrafine- ϕ -slicing data-collection method was introduced and validated in PX1-X06SA in 2016 (Casanas et al., 2016). The comparison with previous data collection strategies (Ben-Shem et al., 2011, p. 3) showed an improvement in the data quality up to slicing at one-tenth of the mosaicity. Due to the number of unit cells per unit of volume, the beam size is regulated to $50 \times 50 \mu\text{m}^2$. Beam transmission ranged from 0.25 to 1 according to the theoretical absorbed dose during the data collection. Data quality and crystal degradation were monitored after every collected dataset, deciding whether or not to record the next one (figure 16). Data were integrated and scaled using the XDS software package. Background calculation was extended to all images in the dataset to increase the noise-to-signal ratio. All statistics increased their quality; the observed R-factors decrease coupled with the high redundancy allowed us to scale several complete datasets together. Friedel's law was rigorously kept as false

in all calculations as the presence of anomalous scatters implied the intrinsic difference of Bijvoet pairs. The relatively new ultrafine- ϕ -slicing/low dose data collection yielded datasets carrying less bias coming from the number of crystals merged. The assumption considering all crystals grown in the same conditions as the same needs to be heavily reconsidered in light of the new detector technology (Casanas et al., 2016). Obtaining complete datasets from one to a maximum of three crystals, especially in the case of small molecule binding sites, is of crucial importance in further steps of structure determination. After single integration, datasets were scaled using XSCALE package contained in XDS suite (Kabsch, 2010; Zander et al., 2016). A file containing the scaled intensity was generated and used in the further step of molecular replacement. Phases were generated using Phenix (Liebschner et al., 2019) applying several cycles of rigid body refinement using the vacant ribosome model (PDB: 4V88), the newly generated .mtz file containing phases information and the .pdb file containing coordinates were used to unambiguously place every compound in their binding pockets.

Data analysis and Model Building

Models and electron density maps were opened in Coot (Emsley and Cowtan, 2004) and positive density peaks in the Fo-Fc map manually inspected. The known nature of lissoclimides and glutarimide binding sites allowed a fast check of such densities placing them unambiguously in the E-site t-RNA binding pocket in the large ribosomal subunit. Anomalous maps generated on Phenix (Liebschner et al., 2019) were as well inspected and osmium hexamine molecules contained in 4V88 removed in case of signal absence or added in case of its presence. In case of low anomalous signal, occupancy of these molecules was set to values ranging from 0.3 to 0.5. Modified ribosome models underwent several cycles of real and reciprocal space refinement along with single and group B-factors after which different inhibitors were placed in their binding pockets. Geometry restrains for all molecules were generated on Grade-Server, stereochemistry and chirality manually inspected and eventually corrected. Compounds were placed in Fo-Fc density refined and merged into the vacant ribosome model. This model was then further refined on Phenix not applying any rigid body refinement but refining single and group B-factors. Several rounds of phenix.refine were performed and the final model of every complex obtained. Despite the quality of

2Fc-Fo maps, some parts stayed poorly defined and noisy. Improving the map is always a process that involves careful manipulation of data to avoid overinterpretation or, in some extreme cases, mis interpretation. To avoid this issue feature enhanced maps (FEM) were calculated also (Afonine et al., 2015). Final models have been used for FEM jobs of Phenix giving as results unbiased maps used for interpretation.

Fo-Fo analysis on ribosome crystals containing lissoclimides

Fo-Fo difference maps are a powerful tool when a deeper understanding of small differences in Fo-Fc is needed. The use of Fo-Fo maps has to undergo a careful check of the isomorphous behavior of datasets involved in the calculation (ref). Datasets have been truncated at the same resolution in both directions, using the highest value (in resolution) for the low-resolution cutoff and the lower value for the high-resolution one. This step guarantees that the information contained in the difference map is not biased by the information coming from higher resolution reflections that might be present in one of the datasets. Unit cell parameters along with unit cell volumes of all datasets have been compared, and percental differences calculated as reported in table. All possible, non-redundant different combinations have been generated. Every group of differences has a reference dataset according to the particular comparison desired. For the first group the reference dataset is Haterumaimide-Q, for the second Bromolissoclimide, for the third Haterumaimide-J and for the fourth Fluorolissoclimide. Isomorphous difference jobs needs three files in Phenix, the reference reflection dataset, the dataset containing reflections that will be subtracted and the reference model for phasing. The outcome of this job is a single .mtz file containing the binary differences calculated from the two given datasets. This mtz file, once properly opened in Coot, will show positive (color code shown in figures when needed) density when present in the reference but not in the comparison. Vice versa, it will show negative density (color code shown in figure when needed) when absent in the reference but present in the comparison. To verify the isomorphous behavior of lissoclimides datasets, the unit cell parameters of datasets used to calculate differences have been subtracted and the percental variation plotted in the diagram in figure n°. The maximum difference between the reference dataset and the others is below 1.5 % in case of cell axes and below 2.5% in case of the cell volume, which is reasonably low to consider this procedure valid (figure 17).

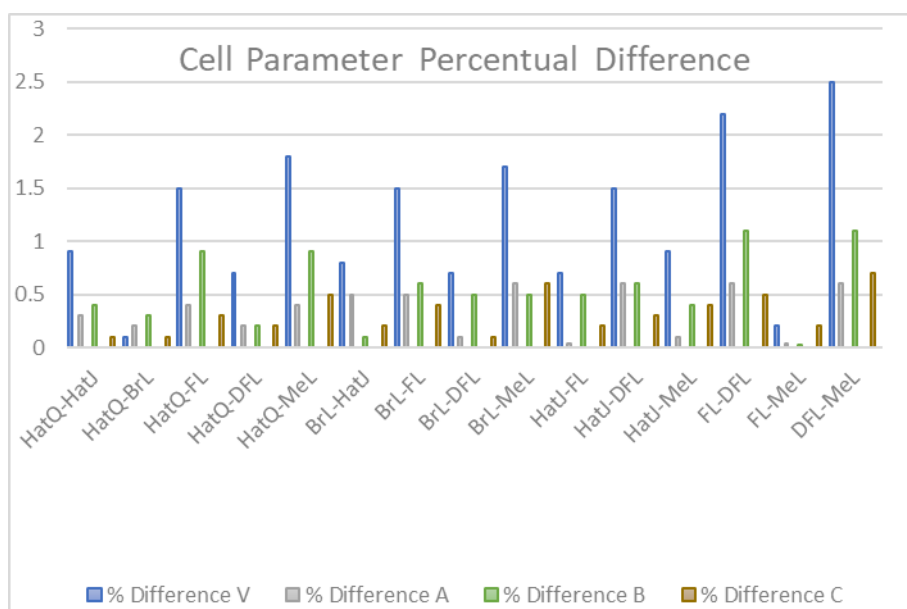


Figure 17 Cell parameters percentual difference plot. Percent values of differences in the unit cell parameter are plotted for each calculated Fo-Fo map. In order: Cell difference volume, difference in a, b and c axes.

Compound	a (Å)	b (Å)	c (Å)	α°	β°	γ°	Cell Volume (Å ³)
HatQ	302.58	285.05	433.72	90	99	90	37408536
HatJ	303.55	286.28	434.22	90	99	90	37733846
BrL	302.09	285.96	433.31	90	99	90	37431769
FL	303.68	287.58	435.09	90	99	90	37997408
DFL	301.85	284.49	432.74	90	99	90	37160815
MeL	303.81	287.52	435.86	90	99	90	38073003

Thermal stability evaluation

Stability of macromolecular complexes is typically investigated by altering thermal or chemical features of the environment in which complexes are placed (reference). In thermal unfolding experiments, a linear increasing gradient of temperature is applied to unfold the specimen under investigation. The thermal stability of a complex is investigated via a parameter known as melting temperature or T_m . This value corresponds to the state at which 50% of the complex population is unfolded, corresponding to the midpoint of the transition from the two states. Both the fluorescence intensity and the fluorescence maximum have a strong dependence on the close surroundings of two aromatic residues, tyrosine and tryptophan. Differences in the ratio of the fluorescence intensities at 350 nm and 330 nm are a suitable tool for detection of even small changes in complex structure, for example due to complex-dissociation Nano Differential Scanning Fluorimetry (nanoDSF) uses the principle described above (Ahmad et al., 2021; “Nano differential scanning fluorimetry (nanoDSF / nDSF),” n.d.; Wen et al., 2020). This technique is often used to evaluate the stability of macromolecular complexes upon binding of small inhibitors or to evaluate their stability under a certain range of buffer conditions. Lissoclimides have all been shown to bind the E-site t-RNA pocket in the large ribosomal subunit establishing different network of interactions according to functional groups borne by these molecules. This experiment is designed to prove whether or not different lissoclimides influence ribosome stability, and in case of positive answer, which is the level of stabilization they induce. The higher the temperature required to denature the complex the bigger is the lissoclimide effect on ribosome stability. Ribosomes were filtered and diluted in buffer CD reaching the final concentration of 8 mg/ml (2.5 μ M), then incubated for 15 min at 30°C with a final concentration of every lissoclimide equal to 75 μ M, these values have been chosen to be the balance between crystallization conditions and fluorescence detectability. As previously said, stocks of compounds were prepared in DMSO, for this reason two different controls were prepared: 80S ribosomes diluted to the final concentration in buffer CD and 80S ribosomes diluted in the same buffer with the addition of DMSO. All conditions were prepared in triplicates and the same experiment has been repeated twice using ribosomes from different purifications. Despite the differences between samples, results show a common trend in the stabilization profile. The NanoDSF experiment was conducted with Prometheus NT.48 equipped with back reflection mirror to enhance the signal

threshold (NanoTemper Technologies, München, Germany) to simultaneously record parameters such as fluorescence at 330-350 nm and the light scattering variation. Samples were loaded in nanoDSF grade standard capillaries (NanoTemper Technologies GmbH, München, Germany) and exposed at thermal stress using $T_1 = 15^\circ\text{C}$ as starting temperature with a ramp of $1^\circ\text{C}/\text{s}$ up to the final temperature of $T_2 = 95^\circ\text{C}$. Denaturation profiles were analyzed using PR.ThermControl software (NanoTemper Technologies, München, Germany). Replicates of the same condition merged and statistical errors calculated. Data have been further analyzed choosing 80S ribosomes with the addition of DMSO as a reference (figure 18, figure 19). Values of inversion points and onset points and their differences are reported in table along with their errors.

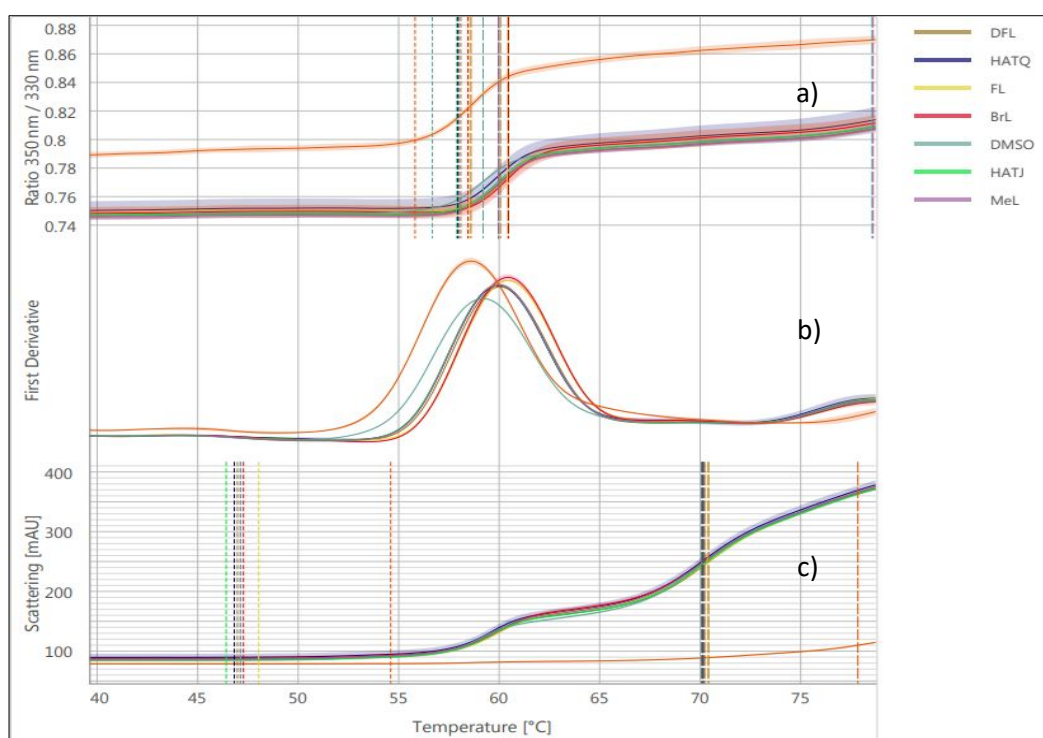


Figure 18 Superimposition of thermal stability profiles of 80S ribosomes in complex with different lissoclimides. Ribosomes incubated with DMSO have been used as a control. a) Ratio between fluorescence at 330 nm and 350 nm for ribosomes in complex with lissoclimides plotted versus the temperature. b) First derivative of the ratio between 330 nm and 350 nm plotted against the temperature, furtherly used for extrapolation of inversion and onset points. c) Scattering counts plotted against the temperature ramp.

<i>Inversion points, onset points and differences Table 2</i>				
	Inversion Point °C ^a	Difference Inversion Point °C ^a	Onset Point °C	Difference Onset Point °C
<i>Vacant</i>	58.62 ± 0.02	-0.60 ± 0.05	55.8 ± 0.2	-0.9 ± 0.2
<i>Vacant + DMSO</i>	59.22 ± 0.05	<i>Reference</i>	56.7 ± 0.1	<i>Reference</i>
<i>BrL</i>	60.46 ± 0.04	1.24 ± 0.05	58.45 ± 0.02	1.7 ± 0.1
<i>FL</i>	60.45 ± 0.06	1.2 ± 0.1	58.5 ± 0.1	1.8 ± 0.1
<i>DFL</i>	60.08 ± 0.01	0.86 ± 0.05	58.12 ± 0.02	1.4 ± 0.1
<i>HatQ</i>	59.97 ± 0.04	0.7 ± 0.1	58.0 ± 0.1	1.3 ± 0.2
<i>HatJ</i>	59.97 ± 0.01	0.75 ± 0.02	57.92 ± 0.02	1.2 ± 0.1
MeL	59.99 ± 0.02	0.77 ± 0.02	58.0 ± 0.1	1.3 ± 0.1

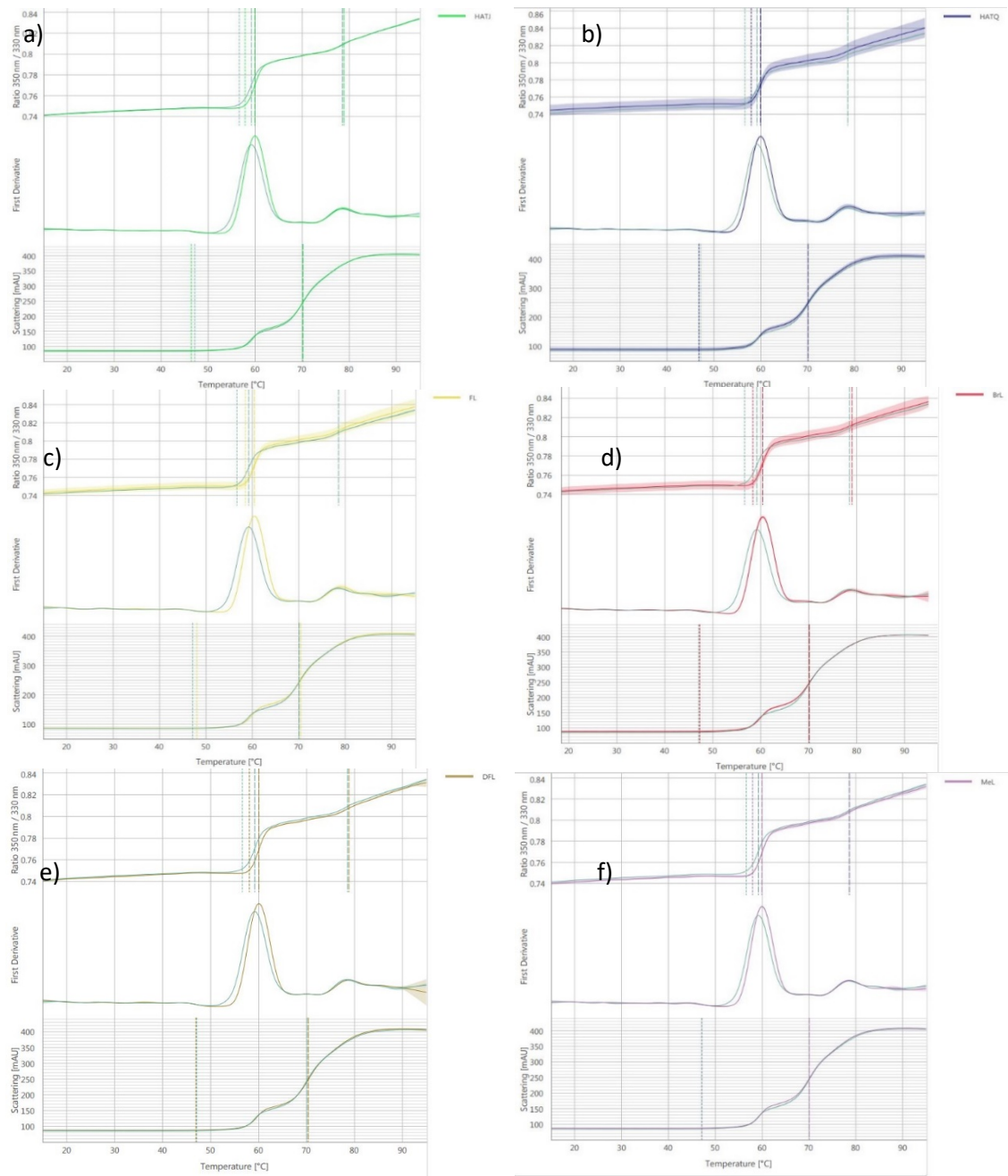


Figure 195 Comparison between thermal stability profiles of lissoclimides and the DMSO control.
 a) HatJ in fluo-green vs DMSO control. b) HatQ in blue vs DMSO control. c) FL in yellow vs DMSO control. d) BrL in red vs DMSO control. e) DFL in ocher vs DMSO control. f) MeL in purple vs DMSO control.

Isothermal Titrations Calorimetry

Ribosomes have been purified according to the protocol previously describe and after gradient fractionation, fractions have been pulled and dialyzed against the ITC buffer as described in the table. Due to the high amount of material needed, different ribosome preparations have been used for one single experiment paying particular attention to using the same stock ITC

<i>Buffer ITC</i>	
Compound	Concentration
MOPS/KOH-pH 7.5-RT	50 mM
KOAc	50 mM
NH ₄ Cl	10 mM
MgOAc ₂	5 mM
DTT	0.95 mM
Glycerol	5%

buffer previously prepared, frozen and kept at -20 °C. Ribosomes were firstly slowly de-frozen and subsequently mixed. The concentration estimated on SHIMADZU-UV (3.8µM) and the sample concentrated until 11.8 µM, due to the high concentration reached, sample has been checked in two different conditions for aggregation using DLS, Dynamic light scattering, showing the absence of aggregates. Due to the enormous quantity of sample needed the experiment has been performed only for one of lissoclimide in duplicate. Haterumaimide-J stock prepared in DMSO was diluted in ITC buffer until the concentration of 162 µM, reaching fifteen times ribosome concentration. This decision was made in order to have enough signal after every injection. The same percentage of DMSO present in Haterumaimide-J solution has been added to ribosomes in order to do not introduce any dilution effect while recording the thermogram. A theoretical C-value for the experiment has been calculated on the basis of previous affinity experiments performed on this class of compounds using different techniques (Pellegrino et al., 2019).

$$C = \frac{[Complex]}{K_D} \times N_{B_{sites}}$$

A value between $0.1 < C < 1$ was expected. The only parameter controllable in this formula is the protein/complex concentration that has been kept as high as possible. A value between $0.1 < C < 1$ was expected. The only parameter controllable in this formula is the protein/complex concentration that has been kept as high as possible. Ribosomes were placed in the experimental chamber and the dilution blank recorded with buffer ITC containing DMSO, dilution signal was at the level of the background.

50 μ L of solution containing Haterumaimide-J were then placed in the syringe connected to the experimental chamber. Nineteen injections were considered enough to fit the integrated final data. The speed of injection was set to 0.5 μ L/s to keep any eventual perturbation of the system away. Temperature at which Isothermal titration calorimetry is performed can make the difference between a success or a failure. Temperature was set at $T = 30^{\circ}$ C, using the same condition as in crystal complex formation. The stirrer angular speed was fixed at $\omega=750$ rpm in order to keep sample and ligand homogeneously distributed in the experimental chamber. Thermograms have been integrated using NitPic applying a baseline manually adjusted with forty points between each injection, this procedure is not common, but the noisy nature of ribosome thermograms made this choice necessary. Integrated peaks have been loaded in SedPhat for further analysis (Scheuermann and Brautigam, 2015; Zhao et al., 2015) (figure 20, figure 21).

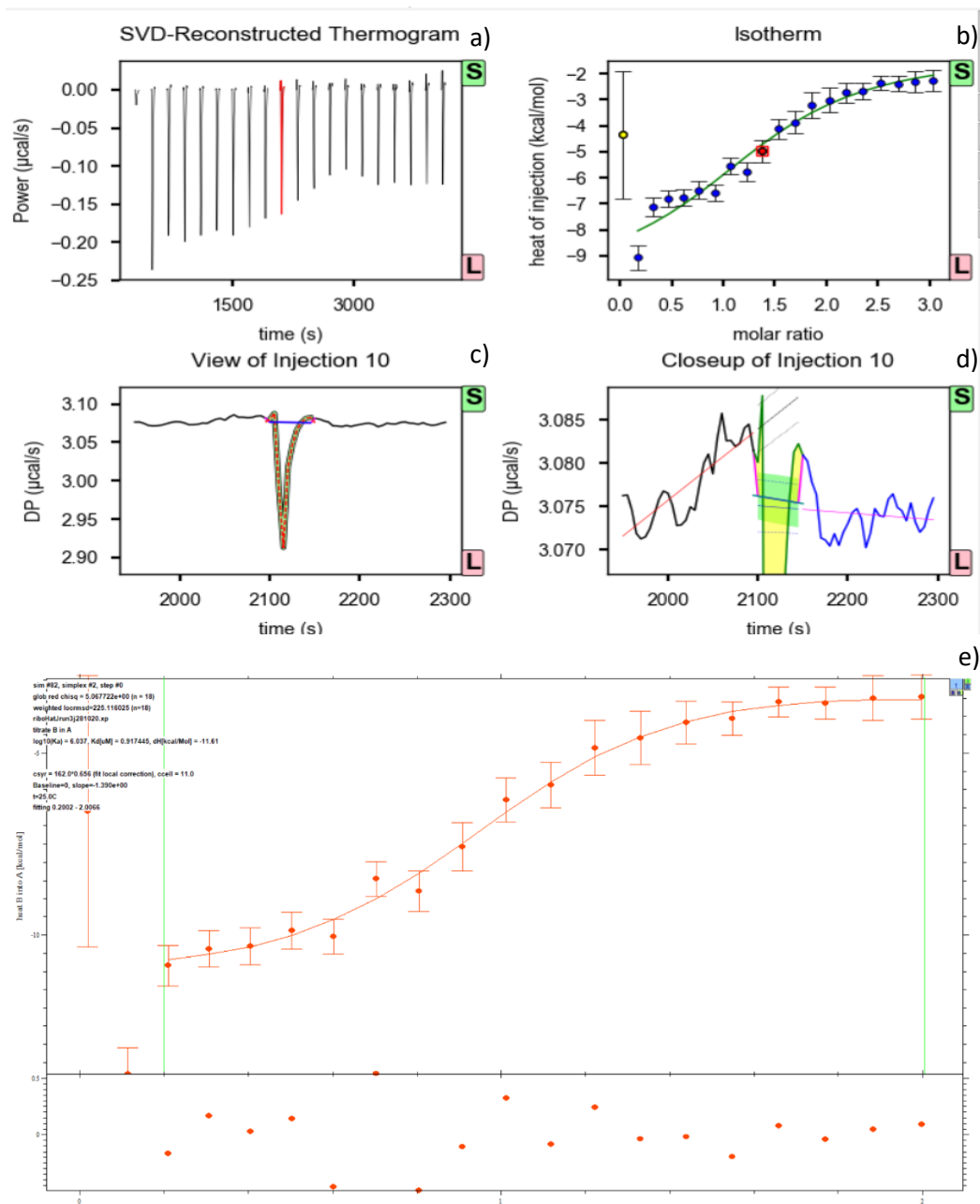


Figure 20 Workflow of Isothermal Titration Calorimetry data processing. a) injection profiles after baseline subtraction, on the x-axis the time expressed in seconds and on the y-axis the power in $\mu\text{cal/mol}$. b) Roughly integrated peaks return the isothermal plot shown in figure. c) Zoon in on injection 10. d) Close up of injection 10, green lines represent the limits for the integration steps, the red lines the roughly calculated baseline. e) Isothermal curve fitting the experimental points obtained after integration of the thermogram shown in figure 8a. The fit has been implemented using a A+B non-cooperative model considering a single binding site. The first two experimental points have been excluded from the interpolation, as shown by the vertical green line.

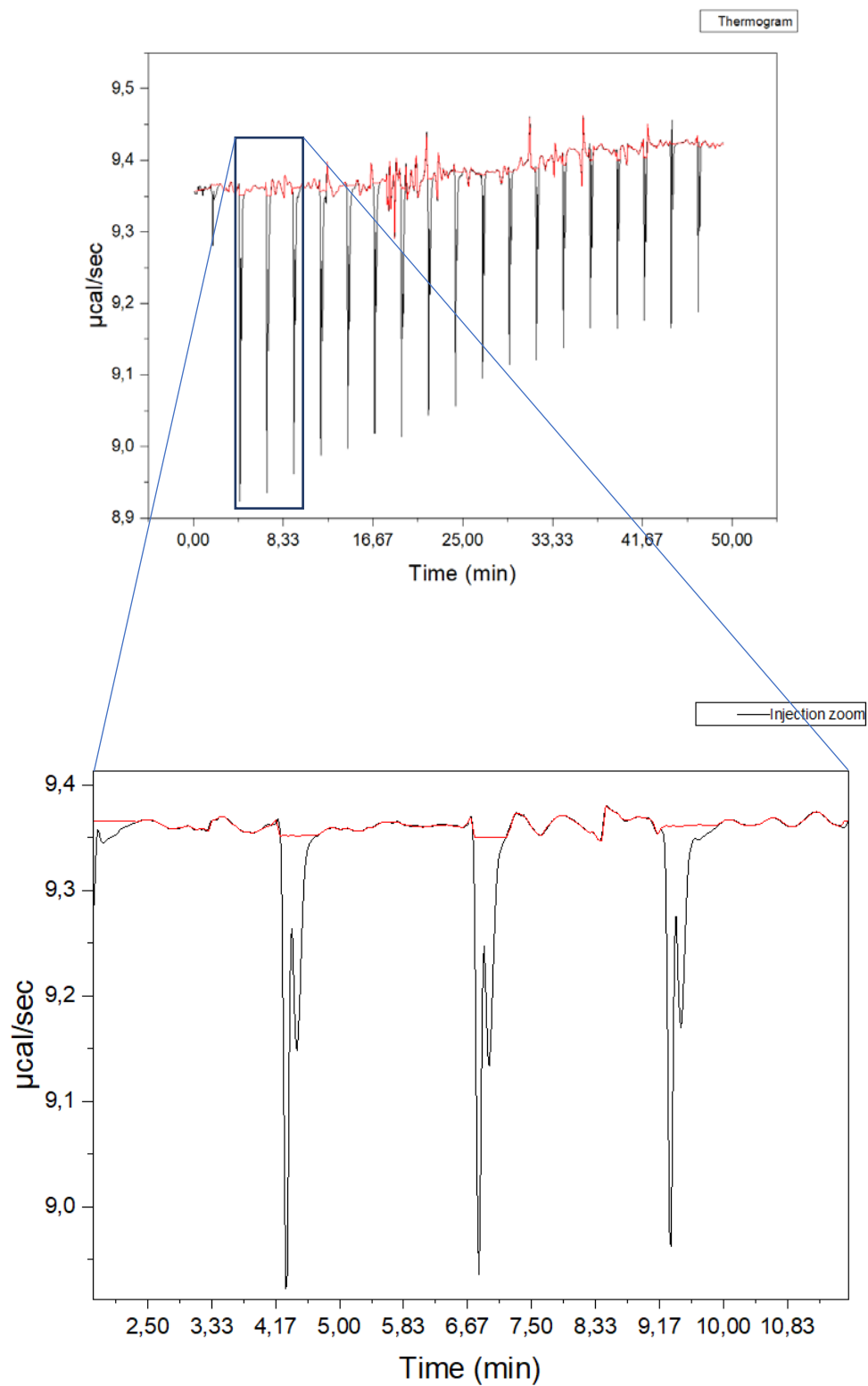


Figure 21 Thermogram of the replicate of the Isothermal Titration Calorimetry experiment of Haterumaimide J binding the yeast 80S ribosome.

Results and discussion

Using *S. cerevisiae* ribosome crystal form, six structures of the eukaryotic 80S ribosome in a complex with lissoclimide congeners bearing different functional groups have been solved at a resolution between 2.9 and 3.2 Å by X-ray crystallography (tables 1, 2, 3, 4, 5 and 6 Appendix). As previously shown for other congener members of this family (Könst et al., 2017; Pellegrino et al.,

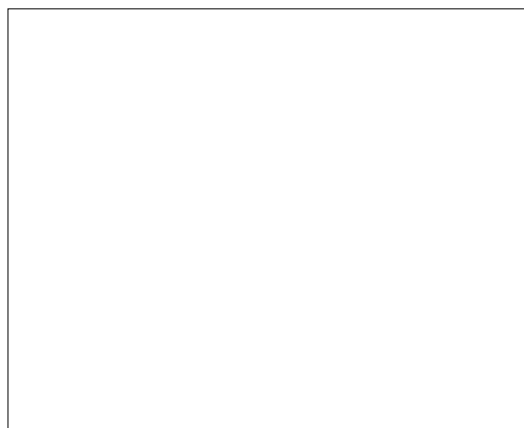


Figure 22 2D representation of lissoclimides.

2019), lissoclimides bind within the 60S subunit E-site-tRNA pocket. Molecularly, the binding mechanism by which lissoclimides alter eukaryotic protein synthesis involves a steric clash with the CCA-end of the tRNA in the E-site pocket during the elongation phase of protein synthesis. Preventing tRNA from exiting the ribosome finally leads to polysomal accumulation and eventual cell death (Pellegrino et al., 2019; Robert et al., 2006). To solve lissoclimide structures (figure 22, figure 23), we used the vacant 80S yeast ribosome (PDB: 4V88) as starting model. Difference density maps (Fobs – Fcalc) were used to locate every inhibitor in its binding site, shedding light on the different rearrangements that the pocket underwent upon binding. As previously reported for Chlorolissoclimide (Könst et al., 2017), the *trans*-decalin ring adopts a chair-chair conformation when accommodated into the E-site pocket of the 60S ribosomal subunit. The pocket shows the presence of a newly built spermidine molecule involved in rRNA stabilization. In the vacant 80S yeast ribosome this density was modelled as a triplet of magnesium atoms. Spermidine engages an extra H-bond with the piperidinedione moiety of some inhibitors. According to the presence of the hydroxyl group on C-8, lissoclimides can establish contacts with the eukaryotic specific protein eL42 (figure 22). The residues involved in these interactions are PRO56 and PHE58. Haterumaimide-Q, Methylissoclimide, Fluorolissoclimide and Bromolissoclimide bear the hydroxyl group at C-8 and are thus able to interact with the protein environment, contrarily Haterumaimide-J along with Deoxy-Fluorolissoclimide, lacking that group cannot make any contact with the eukaryotic specific protein eL42. Within the group of C-8 hydroxyl bearing compounds, we

showed how the substitution of the functional group on C-3 can play a role in the hydrogen bond network formation. Comparison between different structures highlighted different orientations of the decalin ring of lissoclimides in the binding site (RMSD: 0.2/0.3). The succinimide moiety has, averagely, the same orientation in the pocket leading to similar H-bond networks with the rRNA environment, a closer look to both ribosomes in the asymmetric unit show how the binding of lissoclimides in the pocket is not static but carries a certain level of dynamicity as shown in the report table for every inhibitor, this evidence is reported for ligand protein, protein-protein and protein-nucleic acid interactions (Chen et al., 2016; Kuroda and Gray, 2016; Panigrahi and Desiraju, 2007) The role of substitutions on C-3 has been deeply analyzed with the help of several crystallographic tools, stating some features of the intriguing halogen- π and CH_3 - π interactions. Halogenated compounds are, as reported in fig 1, Fluorolissoclimide and Deoxyfluorolissoclimide carrying a fluorine atom at C-3, Haterumaimide-J, carrying a Chlorine instead and Bromolissoclimide bearing the heaviest among the studied substitutions, a bromine atom. Methylissoclimide carries an extra methyl group in position C-3 and Haterumaimide-Q does not bear any substitution at that position. The substitution borne at C-3 has been previously reported to engage a dispersion interaction with the nucleobase G2794 and in one case with the neighboring base G2793 as well (Könst et al., 2017; Pellegrino et al., 2019). Throughout the result part, all different networks of interactions established will be carefully discussed, as well as underlying similarities and observed differences that might influence their activity on translation and binding stability. Furthermore, the Fo-Fo maps will be used to corroborate evidence found during the analysis of single 80S/lissoclimide complexes and their comparison. Interesting cases concerning differences calculated among lissoclimides using Haterumaimide-Q as reference will constitute the second part of the result on lissoclimides.

Overviews

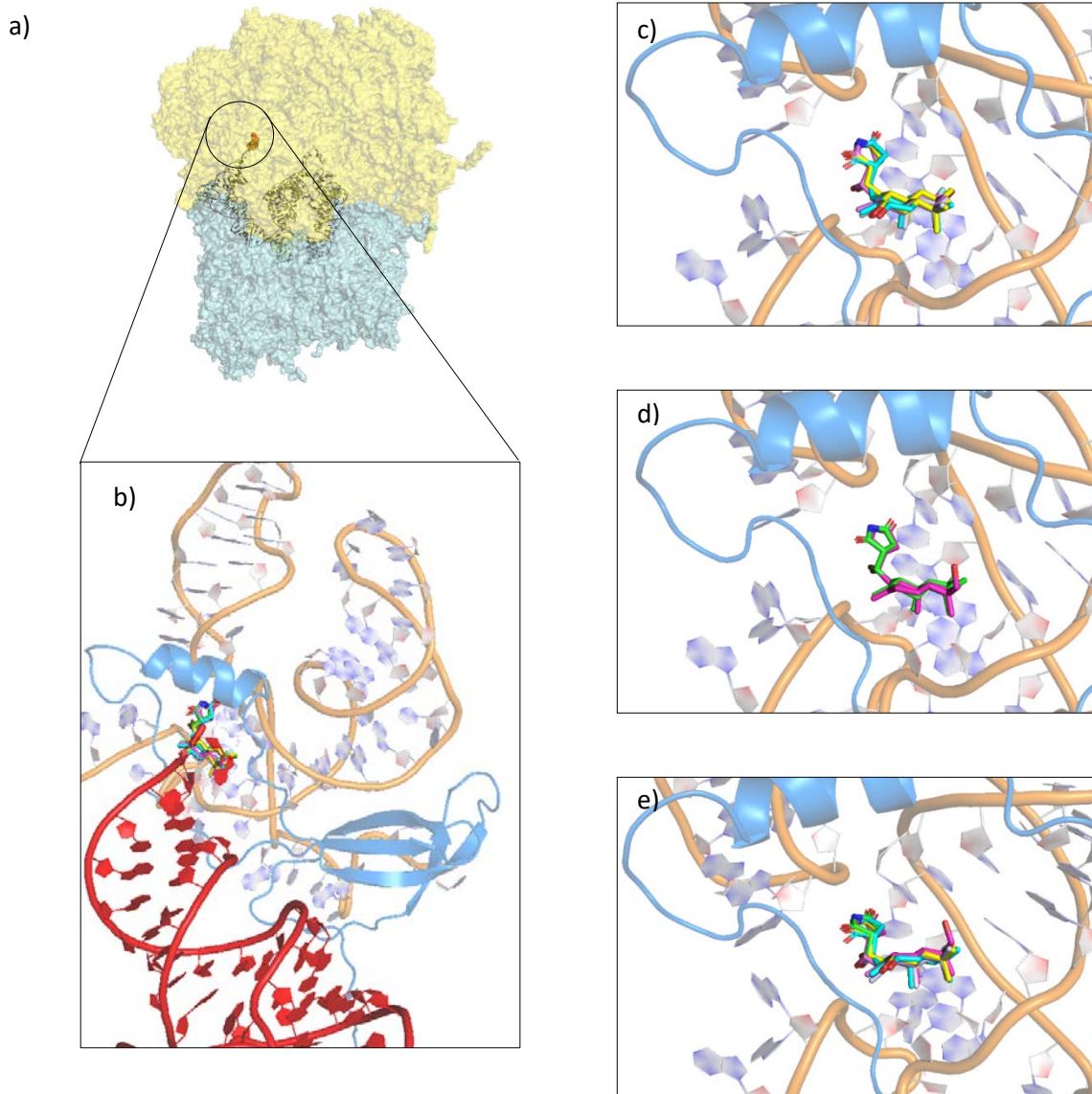


Figure 23 Lissoclimides binding site in a yeast silico model of the 80S ribosome a) Lissoclimides bound within their pocket localized in the large ribosomal subunit LSU shown as surface in yellow. b) Steric clash between the CCA end of the E-site tRNA (PDB:4V6F) in red and different lissoclimides. In blue the eukaryotic specific protein eL42 involved in different contacts with different inhibitors. c) Haterumaimide-Q, Haterumaimide-J, Fluorolissoclimide, Deoxyfluorolissoclimide, Bromolissoclimide and Methyllissoclimide in their binding pocket. d) Lissoclimides (respectively Deoxyfluorolissoclimide and Haterumaimide-J) not bearing the hydrossilic group on the carbon in position 8 cannot contact the eukaryotic specific protein eL42. e) Lissoclimides bearing the hydrossilic group on the carbon in position 8 (Haterumaimide-Q, Fluorolissoclimide, Bromolissoclimide and Methyl lissoclimide) establish contacts with the eukaryotic specific protein eL42.

Structure of Haterumaimide-Q in complex with the eukaryotic 80S ribosome

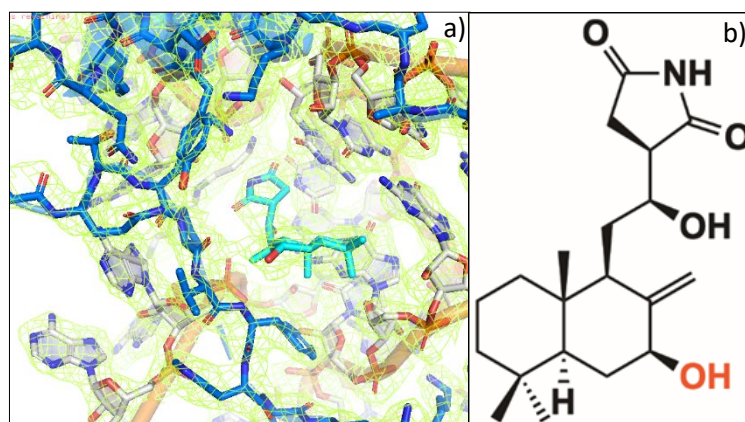


Figure 24 Haterumaimide Q Overview a) Haterumaimide Q shown in cyan in its binding pocket, the featured enhanced map contouring the binding pocket at 1.2 σ level. The density is shown in lemon green b) 2D structure of Hat-Q, the hydroxyl group at C-8 is colored in red.

Haterumaimide-Q is the simplest inhibitor among the analyzed molecules. As shown in figure 22 it bears a hydroxyl group at position C-8 in addition to the universally shared hydroxyl group at C-14 on the linker connecting the *trans*-decalin ring and the succinimide moiety. As indicated by its bidimensional representation, Haterumaimide-Q lacks any functional group on C-3, making the interaction with the two nucleobases G2793-G2794 marginal (figure 22, figure 24). It is possible for HatQ to form contacts with the eukaryotic specific protein eL42. Despite this ability the three-dimensional organization of the binding pocket suggests a minimal interaction with the protein environment. The distances between the C-8 hydroxyl group on HatQ and two residues on eL42 (PRO56 and PHE58) able to form two hydrogen bonds, are not within the canonical range for this kind of interaction. Notably 3.8 Å relatively to the OH group of PRO56 and 3.5 Å away from PHE58 as reported in table n°3. Haterumaimide-Q, as the other members of its family, establishes strong interactions with the ribosomal RNA via its succinimide ring. Specifically, with the backbone of G92 and C93 where it establishes two hydrogen bonds; the first with ribose on G92 and the second with the phosphate backbone of C93. An extra interaction has been proposed with the spermidine molecule

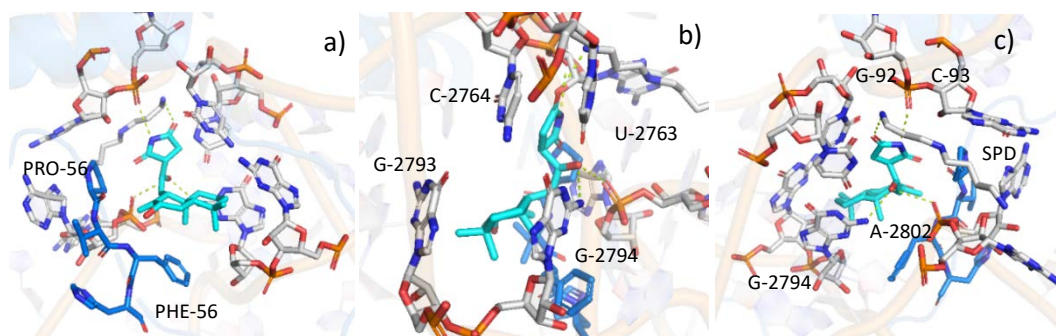


Figure 25 Haterumaimide Q binding site a) Overview of Haterumaimide-Q in its binding pocket, interacting residues from 25S rRNA and eL42 are shown in sticks, in grey nucleotides and in blue amino acids, yellow dashed lines underline interactions within the pocket. b) Detail of guanosine residues 2793 and 2794 (N in *H. sapiens*) in proximity of Haterumaimide-Q. c) Detail of interactions between the rRNA residues A2802/G2793 and the hydroxyl group borne by C-14 in Haterumaimide-Q. The piperidinedione moiety interacts with the ribosomal RNA, further contacts are visible with the spermidine molecule in the E-pocket.

present in the E-tRNA pocket as a further stabilizing contact, this molecule has recently modelled in the pocket instead of magnesium following the publication of pathogenic yeast structures where spermidine has been placed in the pocket (Zgadzay et al., 2022) (figure 25). The hydroxyl group on the linker connecting the two ring moieties of HatQ has been previously reported to interact with the backbone of A2802 (Könst et al., 2017; Pellegrino et al., 2019), here we notice a relevant shift of the decalin ring yielding to the reorganization of the H-bond network established by this particular functional group. The interaction with the NH₂ group of G2794, most likely favored by the lack of any stabilizing groups on C-3, can improve the stability of HatQ in its binding pocket. A comprehensive look at both molecules in the asymmetric unit of 80S ribosome crystals reveals that the interaction with G2794 is present in the two different pockets, supporting the shift hypothesis. Comparing HatQ model and CL (PDB: 5TWB) we can appreciate the displacement of the decalin ring and the relative rearrangement of the network of interaction with the rRNA residues (figure 26). As reported by cytotoxicity assays and in vitro translation inhibition experiments, HatQ has an IC₅₀ of 120 μM (ref), making it one of the less potent members of the lissoclimide family. From a thermal stability point of view, this molecule does not show potent effect either being the last in the rank in the thermostability assays performed using nano differential scanning fluorimetry

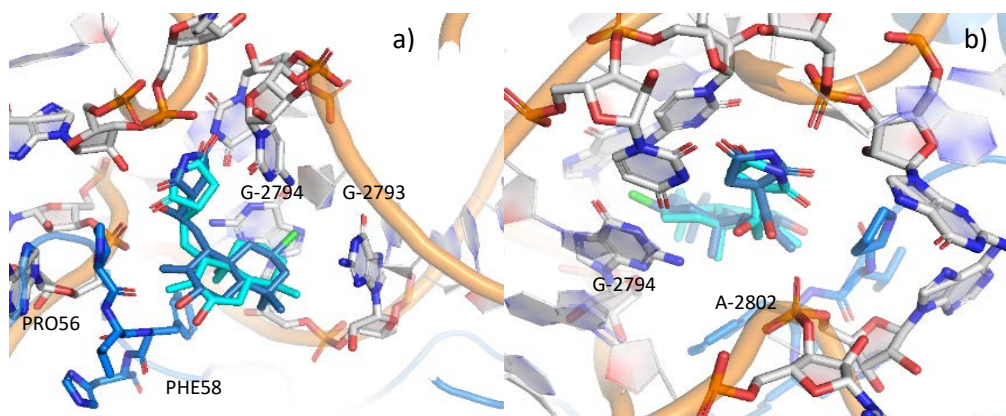


Figure 26 Haterumaimide Q vs Chlorolissoclimide. a) Top view of the superimposition of Hat-Q (in cyan) and CL (in blue) binding pockets (RMSD 0.250). The binding pocket general conformation remains the same while HatQ is rotated towards the residue G-2794. b) Bottom view of the superimposition. The hydroxylic group on C-14 of HatQ moves to interact with G-2794.

HATQ	Ribosome Residues	Molecule1	Molecule2
C8-OH	Pro56	3.80 H-bond	4.1 H-bond
C8-OH	Phe58	3.60 H-bond	3.8 H-bond
C14-OH	A2802	3.10 H-bond	2.70 H-bond
	G2793	3.10 H-bond	3.20 H-bond
C18=O	G92-ribose OH	3.10 H-bond	2.90 H-bond
C17=O	C2763	3.00 H-bond	3.00 H-bond
	SPD	3.10 H-bond	3.20 H bond
C18-N-C17	C93-OP	2.90 H-bond	2.90 H-bond

Table 3 Measured interaction distances within the Haterumaimide binding pocket. In the first column functional moieties on HatQ, in the second column interacting residues in the pocket. Third and fourth column contain in green distances canonically falling in the literature values for the described interaction, in yellow values partially exceeding the reported values and in red values completely out of range.

Structure of Haterumaimide-J in complex with the eukaryotic 80S ribosome

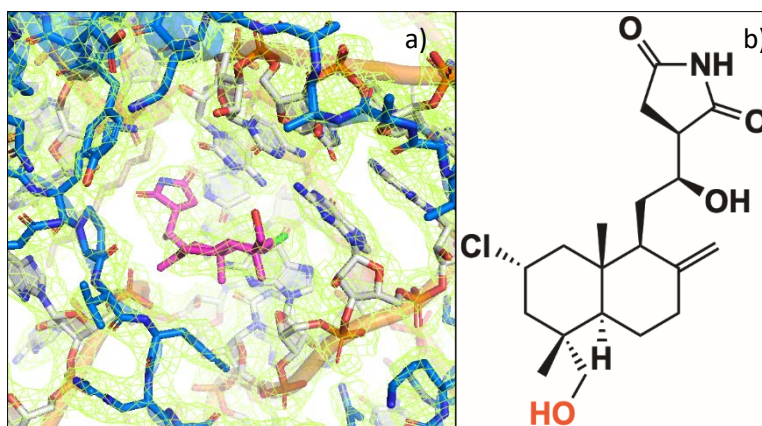


Figure 27 Haterumaimide J Overview a) Haterumaimide J in magenta in its binding pocket, the density from the featured enhanced map contouring the binding pocket at 1.2 σ level is shown in lemon green b) 2D structure of Hat-J, the hydroxyl group at C-20 is coloured in red.

Haterumaimide-J is a newly synthesized chlorine bearing member of the lissoclimide family of compounds (Michalak et al., 2019), as shown in figure 27b, it lacks the hydroxyl group on C-8 making impossible any kind of interaction with the eukaryotic specific protein eL42. As previously highlighted, HatJ bears a chlorination in position C-3, this functional group is found on lissoclimides coming from natural sources, such as the first discovered Chlorolissoclimide from the marine tunicate lissoclinum (Biard et al., 1994). Haterumaimide J has instead a hydroxyl group linked to C-20 able to interact with the pocket environment, where it establishes an interaction with the guanine nucleobase G2793 as shown in figure 28. The distance reported in table n° 4 is 2.7 Å in the first ribosomal molecule and 3.4 Å in the second molecule. This difference in the two ribosomal molecules is not the only one as discussed in the next pages. The hydroxylation on C-20 might partially compensate for the lack of stabilizing interactions with eL42, stretching the nucleobase G-2793 towards the inner part of the pocket. The succinimide moiety, as described for HatQ and other members of lissoclimides, forms a dense network of H-bonds with the nucleic acid environment forming contacts with G92 and C93 backbones and the spermidine molecule. The presence of the halogen in position C-3, as previously postulated,

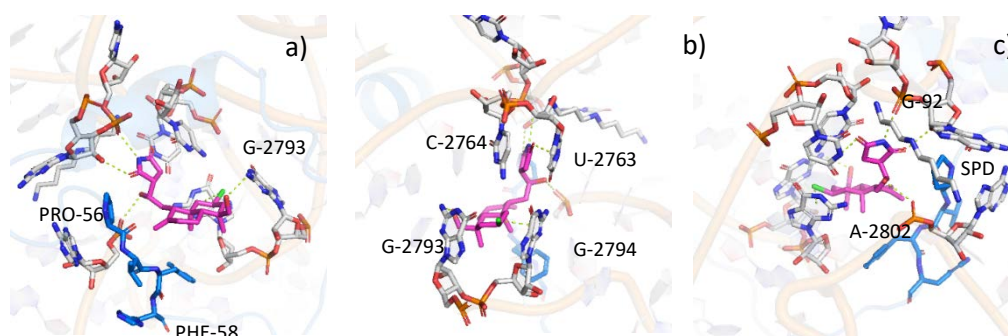


Figure 28 Haterumaimide-J binding site. a) Interacting residues from 25S rRNA and eL42 are shown in sticks, in grey nucleotides and in blue amino acids, yellow dashed lines underline interactions within the pocket. The hydroxyl group borne at C20 interacts with the G2793 b) Detail of guanosine residues 2793 and 2794 (N in *H. sapiens*), the face on halogen- π interaction between the chloride and the π system of G-2794 is shown with a yellow dashed line c) piperidinedione interactions with rRNA established with G-92, G-93 and C-2764. The interaction between the phosphate group of A-2802 is also highlighted.

induce a shift of the decalin ring pushing away the hydroxyl group on C-14 from the interaction with G2794-NH₂ group in the ribosomal molecule 1. Moreover, in the molecule number 2 the interaction with the guanosine nucleobase remains present, and distance-wise, more oriented in the direction of the amino group of G2794 rather than with the phosphate backbone of A2802. The halogen- π interaction between the chloride borne at C-3 and the rRNA residue is shown in figure 5b. Chloride and the π orbitals of G2794 interacts via a dispersion interaction already described (Könst et al., 2017; Pellegrino et al., 2019) (figure 28). The halogen sits 3.3-3.4 Å away from the plane of the G2794 ring matching the interaction distance reported in literature (Könst et al., 2017; Li et al., 2019; Pellegrino et al., 2019). G2793 and G2794 in both ribosomal molecules assume the same conformation if compared with the previously published inhibitors; CL and C45. A light tilt of G2793 due to the interaction with the OH group on C-20 can be seen, but carefully considered not relevant for the binding pocket configuration due to the resolution limit of the dataset used to build the model (figure 29).

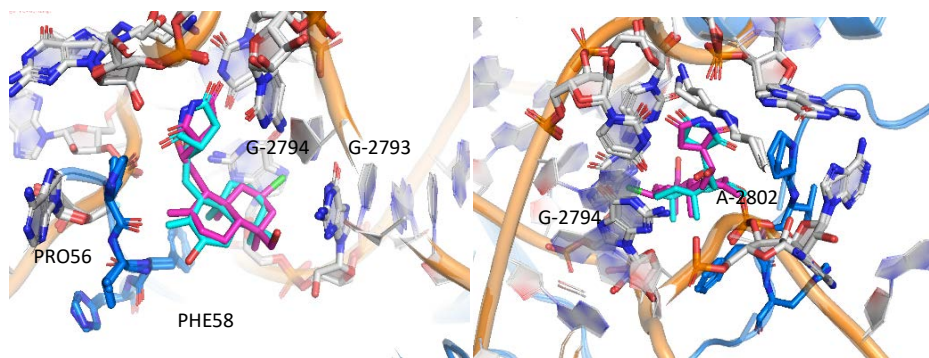


Figure 29 Haterumaimide-Q vs Haterumaimide-J a) Top view of the superimposition of Hat-Q (in cyan) and HatJ (in magenta) binding pockets (RMSD 0.267). A small shift in the decalin ring is visible b) Bottom view of the superimposition of HatQ and CL. The hydroxylic groups on C-14 of HatQ and HatJ are involved in similar interaction both with A2802 and G2794.

Group on HATJ	Group On Ribosome	Molecule1	Molecule2
C3-Cl	G-2794	3.3-halogen-pi	3.40-halogen-pi
C3-Cl	G-2793	3.82-halogen-pi	4.25-halogen-pi
C20-OH	G-2793	2.72-H-bond	3.4 H-bond
C14-OH	A-2802	2.85 H-bond	3.4 H-bond
C18=O	G-92-ribose OH	3.10 H-bond	2.75 H-bond
C17=O	C-2764-N	2.91 H-bond	3.11 H-bond
C18-N-C17	G-93-OP	2.92 H-bond	2.50 H-bond

Table 4 Measured interaction distances within the Haterumaimide J binding pocket. On the first column functional moieties on Hat-J, in the second column interacting residues within the pocket. Third and fourth column contain in green distances fulfilling the literature values for the described interaction, in yellow values partially exceeding the reported values and in red values completely out of range.

Structure of Methyllissoclimide in complex with the eukaryotic 80S ribosome

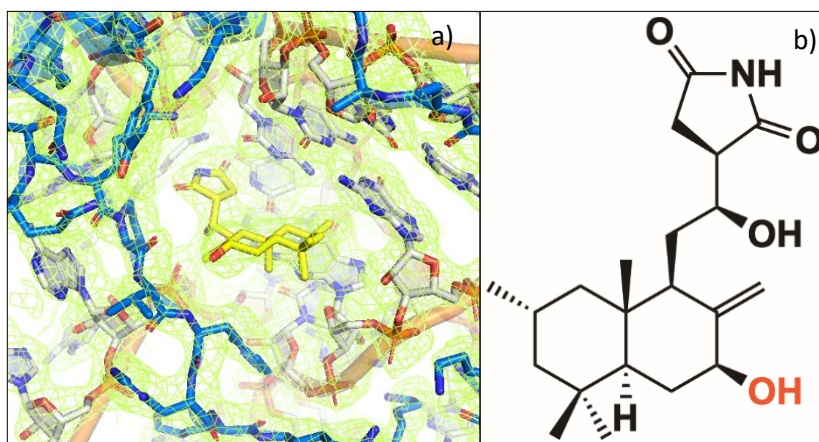


Figure 30 Methyllissoclimide Overview a) Methyllissoclimide coloured in yellow in its binding pocket, the density from the featured enhanced map contouring the binding pocket at 1.2 σ level is shown in lemon green b) 2D structure of MeL, the hydroxyl group at C-8 is colored in red.

Methyllissoclimide shares the same common lissoclimide structure, including the hydroxyl group in position C-8. As shown in figure 30a and in figure 30b, the network of interactions does not differ much from the already presented molecules. Notably, MeL is able to contact via C-8 hydroxylation the eukaryotic specific protein already mentioned in case of HatQ. Looking at table n°5, the interaction distances are higher than the cut-off imposed at the beginning of our discussion. The decalin ring shift noted for HatJ persists, most likely because of the presence of the methylation on C-3, supposed to force the inhibitor on the observed conformation. Regarding the common succinimide-linker moiety, the interaction with A2802 is present and it is the only interaction the hydroxylation at C-14 establishes within the pocket, as observed in both ribosomal molecules, the interaction distance with the guanidine nucleobase number 2794 is far too distant to be considered as similar to those already observed in HatQ and HatJ (figure 31). The hydrogen bonds formed with G92 and C93 and the previously observed interaction with the spermidine molecule are present and shown in figure 8a and 8c. The methylation borne at C-3 replaces the previously described halogen substitution, giving us the chance to discuss the interaction between the π system of G2794 and the non-polar CH_3 group.

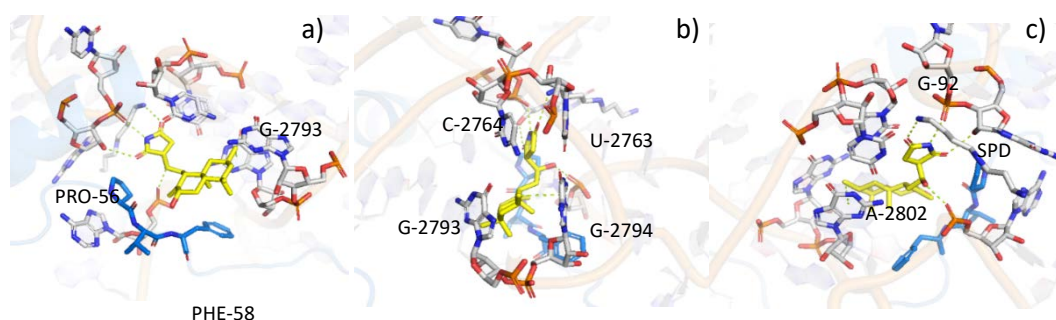


Figure 31 Methyllissoclimide binding site. a) rRNA residues are shown in grey RNA and amino acids from eL42 in blue, yellow dashed lines indicate interactions within the pocket. b) Detail of guanosine residues 2793 and 2794 in proximity of Methyllissoclimide. The interaction between the methyl group carried at C3 and the π system of G-2794 is shown with a yellow dashed line. c) Piperidinedione interactions with rRNA established with G-92, G-93 and C-2764. The interaction between the phosphate group of A-2802 is highlighted along with the hydrogen bond established with the spermidine molecule.

Already observed in several deposited structures this peculiar interaction is poorly characterized (Perras et al., 2017). As shown in figure 31b the methyl group is located 3.5 Å away from the rRNA residue G2794. This interaction is due to the charge-transfer from the C-H orbital and the π system (Mazumdar and Choudhury, 2022; Ribas et al., 2002). It is worth to consider the possibility of MeL interacting not only with the aforementioned nucleotide, but with the neighbour G2793 as well via one of the other C-H orbitals according to their orientation. Due to the resolution at which this complex has been solved, it is not possible to discuss with high precision this particular issue. The presence of both functional groups at C-3 and C-14 is likely the source of the position of MeL in its binding pocket being more similar to the Chlorolissoclimide position rather than Haterumaimide-Q as shown in the PyMOL session containing all lissoclimides. The synergic effect due to presence of substitutions in position three and height will be further investigated in the following pages.

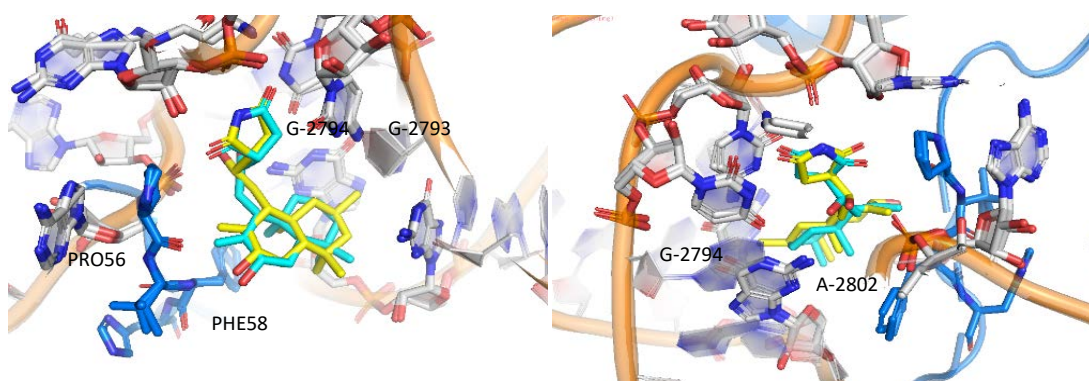


Figure 32 Haterumaimide-Q vs Methyllissoclimide a) Top view of the superimposition of Hat-Q (in cyan) and MeL (in yellow) binding pockets (RMSD 0.357). A small shift in the decalin ring is visible b) Bottom view of the superimposition of HatQ and CL. The hydroxylic groups on C-14 of HatQ and HatJ are involved in similar interaction both with A2802 and G2794.

Group on MeL	Group On Ribosome	Molecule1	Molecule2
C3-CH ₃	G-2794	3.50-CH-pi	3.80-CH-pi
C3-CH ₃	G-2793	3.90-CH-pi	3.85-CH-pi
C8-OH	Pro56	3.40 H-bond	3.64 H-bond
C8-OH	Phe58	3.50 H-bond	3.31 H-bond
C14-OH	A-2802	2.30 H-bond	2.45 H-bond
C18=O	G-92-ribose OH	3.00 H-bond	3.46 H-bond
C17=O	U-2763-N	2.80 H-bond	2.10 H-bond
C17=O	SPD	2.90 H-bond	3.20 H-bond
C18-N-C17	G-93-OP	2.70 H-bond	2.90 H-bond

Table 5 Measured interaction distances within the Methyllissoclimide binding pocket. On the first column functional moieties on MeL, in the second column interacting residues within the pocket. Third and fourth column contain in green distances fulfilling the literature values for the described interaction, in yellow values partially exceeding the reported values.

Structure of Fluorolissoclimide in complex with the eukaryotic 80S ribosome

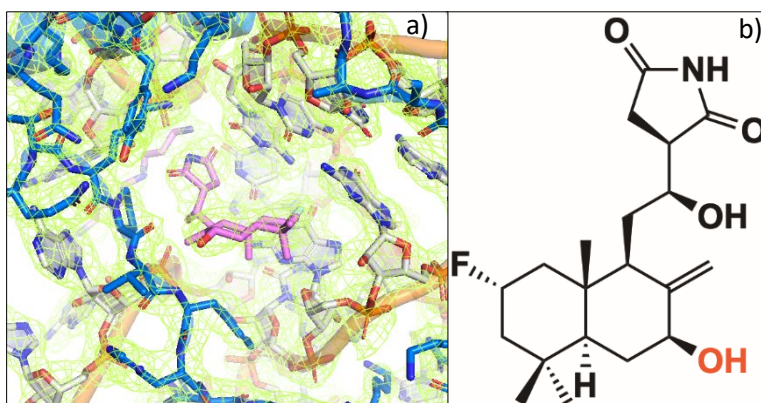


Figure 33 Fluorolissoclimide overview a) Fluorolissoclimide coloured in yellow in its binding pocket, the density from the featured enhanced map contouring the binding pocket at 1.2 σ level is shown in lemon green b) 2D structure of FL, the hydroxyl group at C-8 is colored in red.

Fluorolissoclimide is a freshly synthesized analog of the lissoclimide family of compounds. Its peculiarity is due to the substitution of the naturally occurring chloride with the smallest halogen among this group of atoms (figure 33). Similarly, to MeL and HatQ it carries a hydroxyl functional group on C-8 that gives to Fluorolissoclimide the chance to interact via hydrogen bond with PRO56 and PHE58 from the already mentioned eL42. Fluorolissoclimide makes two contacts with this protein, as reported in table n^o, with an interaction distance of 3.2 Å for both hydrogen bonds (figure 34). The accommodation of FL in its binding pocket shares several features with the already described molecules. The decalin ring bearing the halogen substitution is placed in a slightly rotate conformation in comparison with Haterumaimide Q allowing the protein to get closer to the hydroxyl substitution on C-8 and establish a stronger contact (figure 35). Taking a closer look to the succinimide moiety we can appreciate the rotation of the ring with the consequent readjustment of the OH group borne at C-14 placing it further away from the NH₂ of G2793 responsible for the interaction with HatQ. In case of Fluorolissoclimide, the interaction distance with the phosphate backbone of A2802 is shorter than the previously reported distances, as shown in table n^o 6.

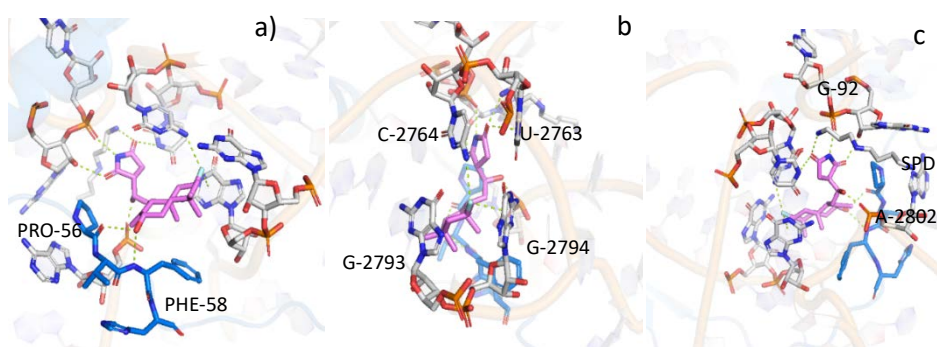


Figure 34 Fluorolissoclimide binding site. a) Interacting residues from 25S rRNA are shown in sticks in grey, eL42 protein in blue. Yellow dashed lines indicate different kind of interactions within the pocket. The hydroxyl group borne at C-8 interacts with the eukaryotic specific protein eL42 b) Detail of guanosine residues 2793 and 2794, the last one establishes a face on halogen- π interaction with the chloride atom borne at C3, as indicated by a yellow dashed line c) piperidinedione interactions with rRNA established with G-92, C-93, C-2764 and the spermidine moiety modelled in the pocket. The interaction between the phosphate group of A-2802 is also highlighted.

The asset of the binding pocket suggests a double bridge between the spermidine molecule, the nucleobase U2763 and the C18=O group. The interesting features of Fluorolissoclimide include the halogen- π interaction in a face on geometry involving the fluorine substitution at C-3. The interaction length measured with respect to the ring plane is 3.1Å, smaller than the one reported for chloride (figure 34). This might be due to different reasons related both to the Vander Walls radii of different atoms and the electronegativity of the groups under scrutiny. The halogen seems to interact also with another polar group in its neighbourhood - the NH₂ group of C2794 donor of an H-bond. This extra interaction has already been described by (Pellegrino et al., 2019) in case of a chlorine substitution. The conformation the second molecule in the asymmetric unit confirms this particular conformation of the binding pocket. As shown in table n° FL, among the described molecules, has a denser network of H-bonds. The influence of such a network will be discussed in the optic of the thermal stabilization induced by FL upon binding.

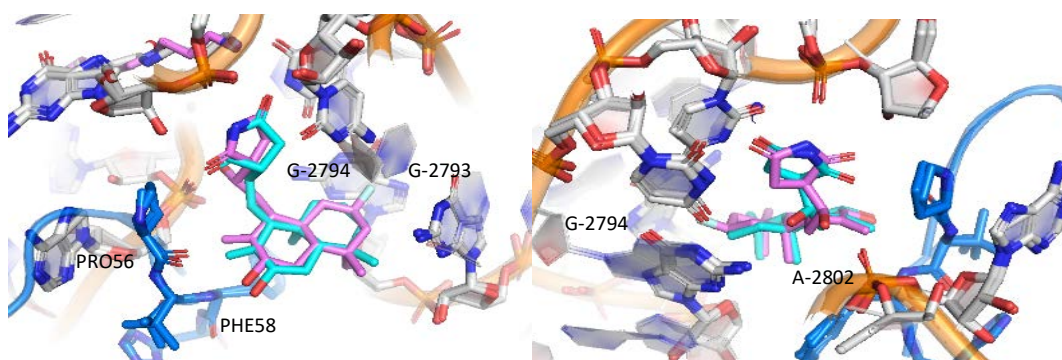


Figure 35 Haterumaimide-Q vs Fluorolissoclimide. a) Top view of the superimposition of Hat-Q (in cyan) and FL (in pink) binding pockets (RMSD 0.357). Detail of the decalin ring orientation within the pocket, the presence of fluoride on C-3 helps accommodating the inhibitor in the binding site. The hydroxylic groups on C-14 of HatQ and FL differ in their network of interaction, Fluorolissoclimide does not interact via H-bond with G2794.

Group on FL	Group On Ribosome	Molecule1	Molecule2
C3-F	G-2794	3.1-halogen-pi	3.5-halogen-pi
C3-F	G-2793	- halogen-pi	- halogen-pi
C3-F	C-2764	3.3 H-bond	-
C8-OH	Pro56	3.2 H-bond	3.40 H-bond
C8-OH	Phe58	3.2 H-bond	3.00 H-bond
C14-OH	A2802	2.10 H-bond	2.60 H-bond
C18=O	G92-ribose OH	3.00 H-bond	3.20 H-bond
C17=O	U2763-N	3.00 H-bond	2.40 H-bond
	SPD	2.80 H-bond	2.80 H-bond
C18-N-C17	G93-OP	2.70 H-bond	2.58 H-bond

Table 8 Measured interaction distances within the Fluorolissoclimide binding pocket. On the first column functional moieties on FL, in the second column interacting residues within the pocket. Third and fourth column contain in green distances fulfilling the literature values for the described interaction, in yellow values partially exceeding the reported values.

Structure of Deoxy-fluorolissoclimide in complex with the eukaryotic 80S ribosome

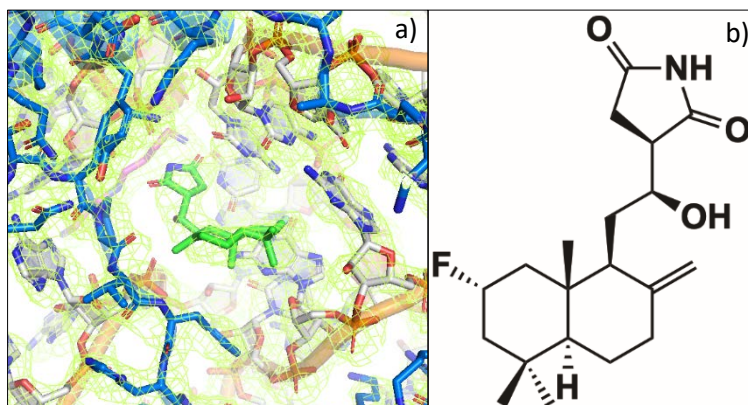


Figure 36 Deoxyfluorolissoclimide Overview .

a) Deoxyfluorolissoclimide coloured in yellow in its binding pocket, the density from the featured enhanced map contouring the binding pocket at 1.2 σ level is shown in lemon green b) 2D structure of DFL.

Deoxyfluorolissoclimide is the deoxygenated counterpart of FL, the only difference between these two molecules is the lack of the hydroxyl group at C-8 (figure 22, figure 36). As already stated for similar cases, this fact implies the inability of DFL to form connections with protein residues surrounding the pocket. Attention needs to be paid to the rings of DFL. The decalin ring is slightly shifted up if compared with FL, unveiling once more how the hydroxyl group on C-8 plays a role in the pocket conformation (figure 37). The lack of interaction with eL42 seems to give to DFL a degree of freedom more. The succinimide moiety along with the hydroxylated linker slightly shifts up moving the modelled inhibitor towards rRNA residues G2793-G2794. This shift induced a movement of the OH group at position C-14 away from the rRNA backbone, particularly A2802 bringing back the interaction distance to 2.6 Å. The network of interaction surrounding the succinimide ring appears to be conserved. DFL makes contacts with G92, C93 along with the spermidine molecule within the pocket. A zoom in into the halogenated part of DFL highlights a similar behaviour of such group: the face on halogen- π is shown in figure 11b with an interaction distance matching the one of FL, 3.0 Å away from the ring plane of G2794. Guanosine 2793 seems to interact in a similar manner as already shown for FL, engaging in an H-bond with the halogenated group (figure 37).

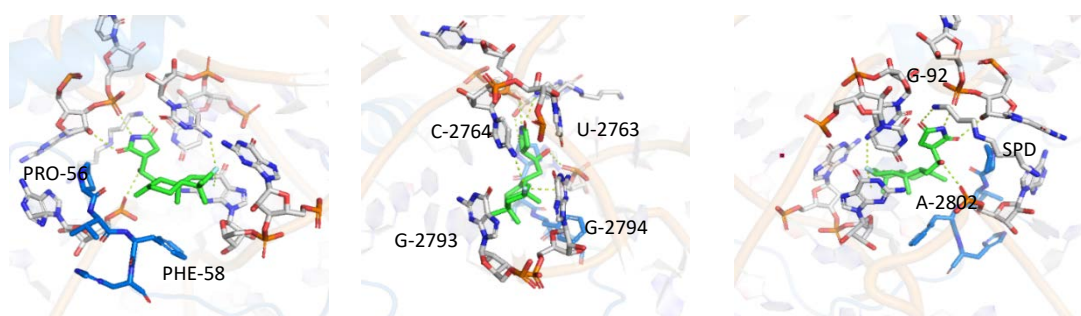


Figure 37 Deoxyfluorolissoclimide binding site. a) Interacting residues are shown in sticks, in grey rRNA and in blue amino acids from eL42, yellow dashed lines indicate interactions within the pocket. b) The face on halogen- π interaction between the fluoride and the π system of G-2794 is shown with a yellow dashed line c) piperidinedione interactions with rRNA established with G-92, G-93, C-2764 and the amine group of spermidine. The interaction between the phosphate group of A-2802 is also highlighted.

The second ribosome molecule offers us a different view of the interaction network within the binding pocket. The halogen- π interaction along with some hydrogen bonds seems to have longer distances if compared with values reported for molecule 1. This fact could be explained, not only with the actual different conformation of the binding pockets, but also with the known differences in the quality of the map for the molecule number 2. DFL shows a thermal stabilization profile stronger than HatQ, as well lacking the hydroxylation at C-8 opening questions on how halogen substitutions affect the stability and conformation of the binding pocket (figure 38) (Mei et al., 2019).

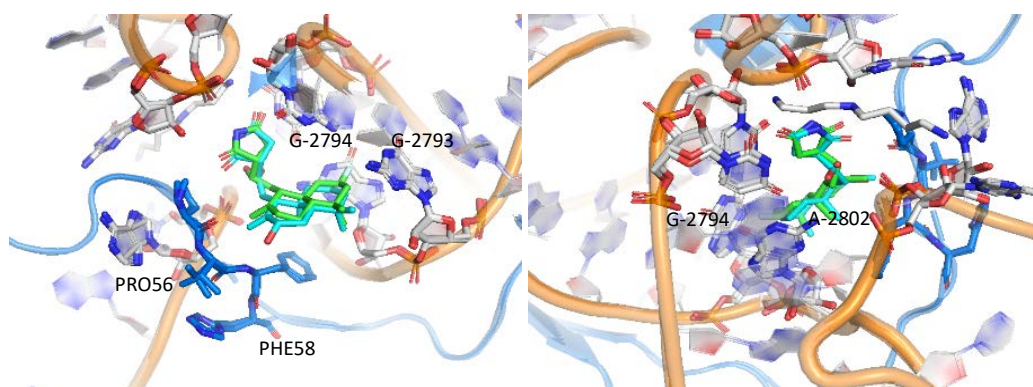


Figure 38 Haterumaimide-Q vs Deoxyfluorolissoclimide. a) Top view of the superimposition of Hat-Q (in cyan) and DFL (in pink) binding pockets (RMSD 0.237). Detail of the decalin ring orientation within the pocket, the absence of hydroxylation on C-8 . The hydroxylic groups on C-14 of HatQ and FL differ in their network of interaction, Fluorolissoclimide does not interact via H-bond with G2794.

Group on DFL	Group On Ribosome	Molecule1	Molecule2
C3-F	G-2794	3.0-halogen-pi	3.4-halogen-pi
C3-F	G-2793	3.9-halogen-pi	4.1-halogen-pi
C3-F	C-2764	3.2 H-bond	3.8 H-bond
C14-OH	A2802	2.9 H-bond	3.6 H-bond
C18=O	G92-ribose OH	2.9 H-bond	3.09 H-bond
C17=O	C2763-N	2.9 H-bond	3.10 H-bond
	SPD	3.1 H-bond	2.60 H bond
C18-N-C17	C93-OP	2.9 H-bond	2.95 H-bond

Table 7 Measured interaction distances within the Deoxyfluorolissoclimide binding pocket. On the first column functional moieties on DFL, in the second column interacting residues within the pocket. Third and fourth column contain in green distances fulfilling the literature values for the described interaction, in yellow values partially exceeding the reported values.

Structure of Bromolissoclimide in complex with the eukaryotic 80S ribosome

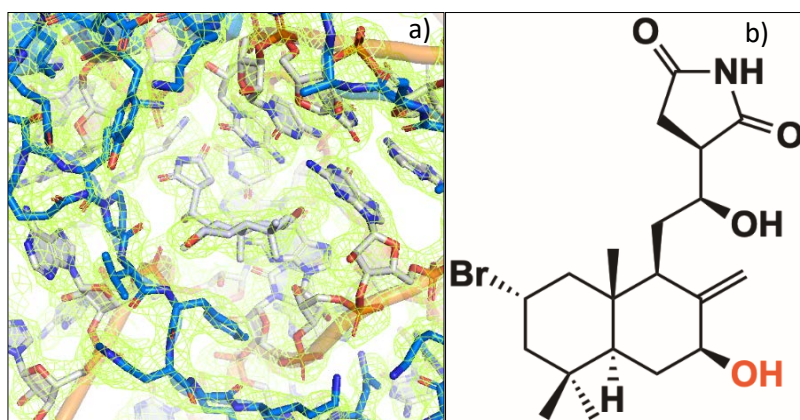


Figure 39 Bromolissoclimide Overview. a) The density from the featured enhanced map contouring the binding pocket at 1.2 σ level is shown in lemon green b) 2D structure of BrL, the hydroxyl group at C-8 is coloured in red.

Bromolissoclimide has the common core of other lissoclimides but it bears a bromine substitution on C-3 - the heaviest halogen substitution among the presented ones (figure 22, figure 38). Interestingly this substitution is often found in natural compounds from marine origins (Benedetto Tiz et al., 2022). Thanks to the presence of the OH group on C-8, Bromolissoclimide can and does make contacts with the eukaryotic protein eL42 establishing, as its fluorinated counterpart FL, two hydrogen bonds. Bromolissoclimide interacts via C-8 hydroxylation with proline 56 and phenylalanine 58 as shown in figure 40 . Interaction distances are 3.0 Å for both bridges, indeed very similar to the reported for FL but slightly shorter than the one reported for natural occurring Chlorolissoclimide (Könst et al., 2017). The rotation of the decalin ring respect Haterumaimide Q is observed for Bromolissoclimide as well, probably facilitating the face on halogen- π that will be later discussed. A synergic combination between the movement of the decalin ring due to the substitution on C-3 and the presence of the C-8 could be the reason why the interaction distances between the C-14 hydroxylation on the linker connecting the piperidinedione moiety in case of Bromolissoclimide decreases compared to Haterumaimide J and

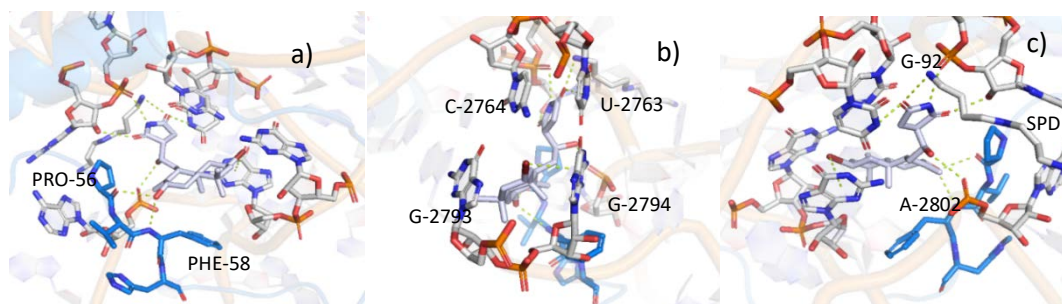


Figure 40 Bromolissoclimide binding site. a) Interacting residues are shown in sticks, in grey rRNA and in blue amino acids from eL42, notably proline 56 and phenylalanine 58. Yellow dashed lines indicate interactions within the pocket. b) The face on halogen- π interaction between the bromide and the π system of G-2794 is shown with a yellow dashed line c) The H-bond network between the piperidinedione moiety and the pocket environment is shown, remarkable interactions are established with G-92, G-93, C-2764 and the spermidine molecule. The interaction between the phosphate group of A-2802 and the hydroxyl group on C14 is also highlighted.

Deoxyfluorolissoclimide. The C-14 hydroxylation is involved in an H-bond with the rRNA residue A2802, as already discussed with an interaction distance of 2.4 Å in the first molecule, and 2.90 Å in the second one. The linker-succinimide moiety interacts with the pocket in a very similar manner, the interactions with the rRNA backbone involve residues G92 and C93 respectively. A tilt is visible when compared to the position assumed by the HatQ counterpart (figure 41). The interaction with the residue C2764 and the succinimide ring is shown in figure 40 in yellow dashes. The same group on Bromolissoclimide establishes an extra hydrogen bond with the polyamine present in this structure. The C-3 bromide atom characteristic of BrL, sits between the guanosine-nucleobases getting involved in a halogen- π interaction. Among all the discussed interactions between the π system of rRNA bases and the three first members of the seventh group in the periodic table of elements, this specific X-Br- π is the one with the longest interaction distance, 3.5 Å away from the base plane. Significantly longer than the one from lighter halogens, it is linked to the physical dimensions of the element in question. Remarkably, the interaction distance matches with the one reported for Agelastine A (McClary et al., 2017). Together with the already discussed FL, Bromolissoclimide shows a very dense network of H-bond interactions, affecting its stability within the pocket, as also suggested by the thermal stability assays (figure 40).

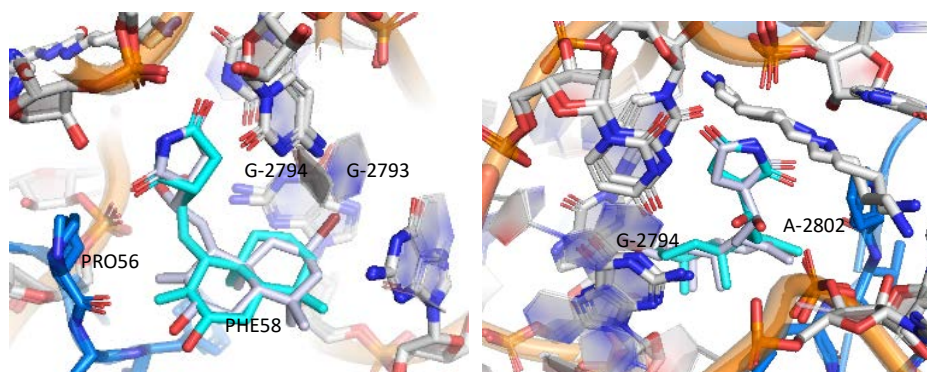


Figure 41 Haterumaimide-Q vs Bromolissoclimide. a) Top view of BrL (in grey) superimposed on HatQ (in cyan) (RMSD 0.337). b) Detail of the respective movement of decalin ring within the pocket. C-14 hydroxylation is shown for both inhibitors. The tilt of this group towards A2802 in case of BrL is present as in case of FL.

Group on BrL	Group On Ribosome	Molecule1	Molecule2
C3-Br	G-2794	3.5-halogen-pi	3.9-halogen-pi
C3-Br3.0	G-2793	3.6-halogen-pi	4.1-halogen-pi
C8-OH	Pro56	3.00 H-bond	3.13 H-bond
C8-OH	Phe58	3.00 H-bond	3.20 H-bond
C14-OH	A2802	2.40 H-bond	2.90 H-bond
C18=O	G92-ribose OH	3.30 H-bond	3.00 H-bon
C17=O	C2764-N	3.00 H-bond	2.50 H-bond
	SPD	3.20 H-bond	2.60 H-bond
C18-N-C17	C93-OP	2.70 H-bond	3.10 H-bond

Table 8 Measured interaction distances within the Bromolissoclimide binding pocket. On the first column functional moieties on BrL, in the second column interacting residues within the pocket. Third and fourth column contain, in green, distances fulfilling the literature values for the described interaction.

Lissoclimides comparison

Many hypotheses have been formulated regarding the different organization of the t-RNA E-binding site upon interaction with lissoclimides. What is clear from the first look at the single structure is the crucial role of two different groups on the inhibitor: the hydroxylation on C-8 and the functional group on C-3 (CH₃, F, Cl, or Br). To better investigate different hypotheses and make more solid statements, lissoclimides have been clustered in different groups:

- Lissoclimides bearing simultaneously halogens on C-3 and the OH group on C-8 (FL-CL-BrL)
- Lissoclimides bearing halogens on C-3 and no hydroxylation on C-8 (DFL-HATJ)
- Lissoclimides not bearing halogens with the OH group on C-8 (HATQ-MeL)
- Lissoclimides bearing the same halogen with and without the C-8 hydroxylation (FL-DFL)

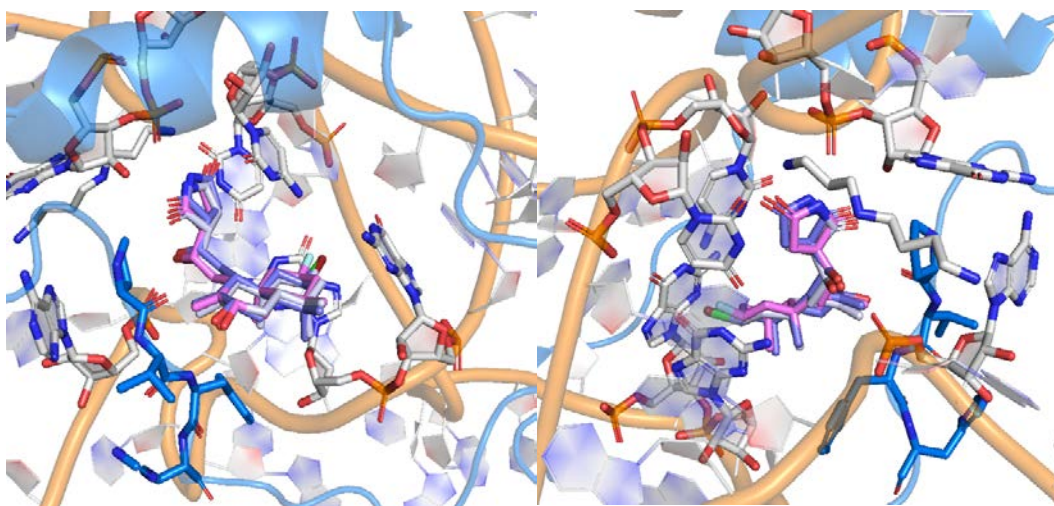


Figure 42 BrL-vs-CL-vs-FL a) Top view of superimposition of halogen bearing lissoclimides with the hydroxyl group on carbon 8. In pink Fluorolissoclimide, in purple Chlorolissoclimide and in grey Bromolissoclimide. Details of the rearrangement of halogens according to their radius. Fluorine, Chlorine and Bromine respectively in white, green and dark red. b) Bottom view of superimposition, C-14-OH group interacting with A2802 is shown, the clear match between groups from different inhibitors is observed despite the slight rotation of the succinimide moiety.

The analysis of C-3 halogen/C-8 hydroxylation bearing compounds shows how these molecules accommodate within the binding site in a very similar manner, the hydroxyl group establishes interaction with the eukaryotic protein eL42, as shown in figure 42. Despite the different halogen borne at C-3 the interaction with the nucleobases shows the same arrangement of G2793 and G2794, with a shorter distance between the halogen and the base scaling with the Van der

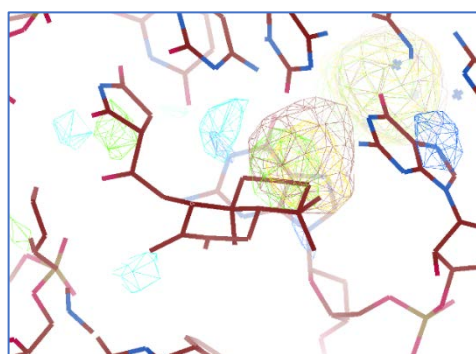


Figure 43 Residual density Fo-Fo calculation on Hat-Q (model shown in figure). Density contouring C-3 comes from three separated difference map calculations. In green $FO_{\text{HatQ}}-FO_{\text{FL}}$, in yellow $FO_{\text{HatQ}}-FO_{\text{HATJ}}$ and in burgundy $FO_{\text{HatQ}}-FO_{\text{BrL}}$. All maps are shown at $\pm 3.5 \sigma$.

Walls radii of the substitution ([VdW radii vs halogen- π] F (1.47Å VdW- 3.05 Å halogen- π) < Cl (1.75 VdW- 3.35 Å halogen- π) < Br (1.85) VdW- 3.55 Å halogen- π ref). The combined effect of the halogenation and the hydroxylation on C-8 places the C-14 OH group on the linker in the right position to interact via H-bond with the phosphate backbone of A2802 (figure 41b). This particular behavior is observed for FL, CL and BrL and to some extent (the loss of H-bonds with eL42) in MeL. Further analyses of the pocket do not show any other engagement of C-14-OH, which is confirmed by the Fo-Fo difference map peaks

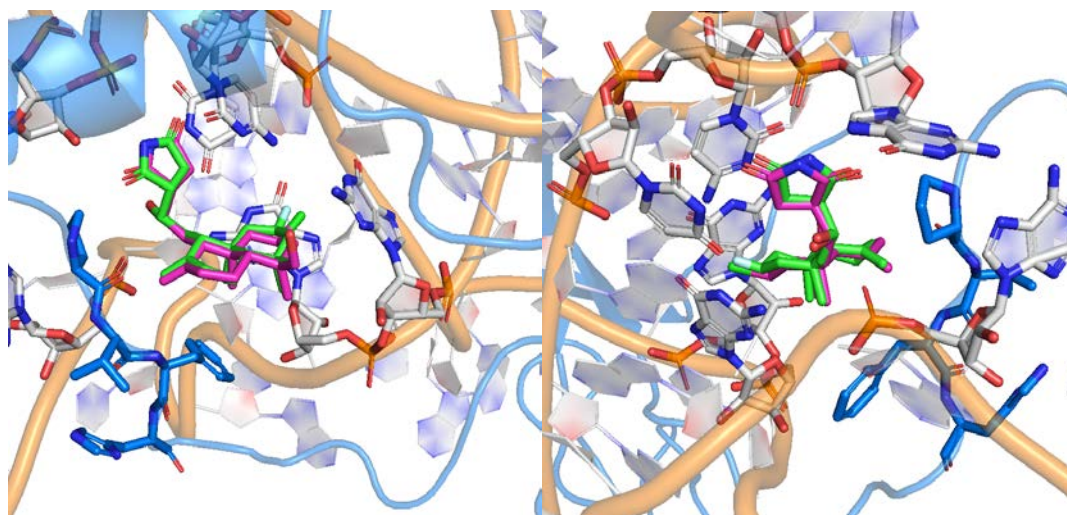


Figure 44 DFL vs HATJ a) Top view of superimposition of lissoclimides lacking the OH group on carbon 8. In green Deoxyfluorolissoclimide, in magenta Haterumaimide J. The decalin is placed almost in the same position in both inhibitors b) Bottom view of superimposition. The same orientation of the succinimide moiety is evident from the figure.

analysis. The Fo-Fo residual density in fig 43 is calculated using Haterumaimide-Q as reference and it shows how qualitatively different the interaction is with G2793-G2794 between the reference and the halogenated congeners. The strongest signal comes, as expected, from Bromolissoclimide, carrying the heaviest among the substitutions and the richest in terms of electrons. In the middle we find Haterumaimide J, bearing a chlorine atom. The smallest density is the one coming from Fluorolissoclimide. In figure 43 is present a strong electron density signal behind nucleobases G2794-G2793. This density comes from an Os-hexamine molecule that has different occupancies and positions in the different crystals. During the Fo-Fo calculations these differences are enhanced giving the final results shown above. More residual density is spread around the binding pocket, of particular relevance is the cyan density in the proximity of C-8 hydroxylation in Haterumaimide-Q coming from $F_{O_{HATQ}} - F_{O_{HATJ}}$, indicating the presence of electrons in the HatQ initial map and the absence of them in Hat-J, this observation is consistent with the chemical structure of these two compounds. Another interesting comparison to understand the contribution of C-8 and C-3 substitutions is the one between Haterumaimide-J and

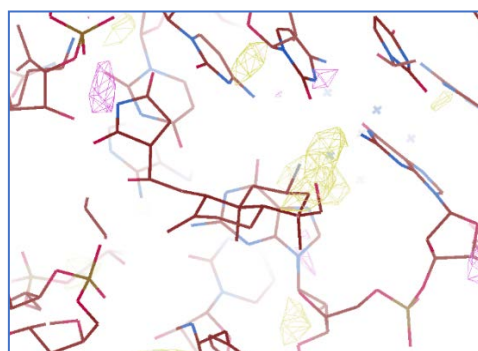


Figure 45 Residual density Fo-Fo calculation with Hat-J (model shown in figure) and DFL. The yellow density in the proximity of C-3 comes from the difference map calculations between Hat-J and DFL, All maps are shown at $\pm 3.5 \sigma$.

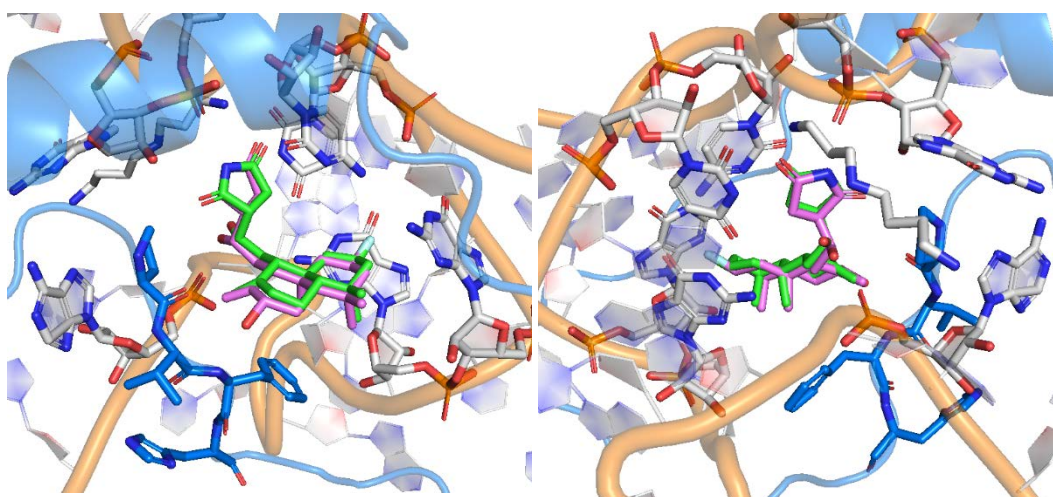


Figure 46 FL vs DFL a) Top view of superimposition of “same-halogen” bearing lissoclimides with and without the OH group on carbon 8. In green Deoxyfluorolissoclimide, in pink Fluorolissoclimide. The decalin ring shift of DFL respect of FL is appreciable b) Bottom view of superimposition. The movement due to the lack of hydroxylation on C-8 brings the OH group of C-14 of DFL closer to the nucleobase G2794.

Deoxyfluorolissoclimide both molecules possess the halogenation on C-3 and both lack the OH group on C-8 (figure 44). As already highlighted before, Hat-J has this group displaced on C-20 as shown in figure 22. Once again, the superimposition shows the match between the decalin rings of DFL and Hat-J and the same orientation of C-14 hydroxyl group (figure 45). Comparison between the amplitudes from these inhibitors shows the presence of residual density for C-20 hydroxylation extending towards the NH₂ group of G-2793, corroborating the assumption previously made just analyzing the interaction distances (figure 46). We can as well appreciate the lack of residual density on the OHX binding site, most likely due to the similar position in the two-dataset subtracted. Model comparison and difference map inspection are powerful tools used to find differences in lissoclimide binding interactions. A useful comparison used to understand the role of halogens and their synergic contribution with the hydroxylation on C-8 to lissoclimide binding is the one between Fluorolissoclimide and Deoxyfluorolissoclimide (figure 46). As we can observe in figure the accommodation into the binding pocket is pretty similar in case of fluorine bearing molecules. We observed a reduction in the interaction distance between

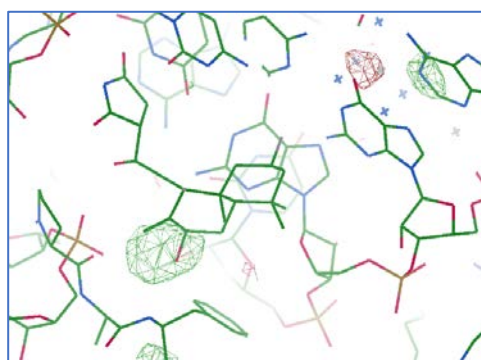


Figure 46 Residual density Fo-Fo calculation on FL-DFL (FL model shown in figure). The yellow density by C-8 comes from the difference map calculations between FL and DFL. Map is shown at $\pm 3.5 \sigma$.

the halogen and the π system due to the shift of the whole compound due to the lack of C-8 hydroxylation. The interaction between the eukaryotic protein eL42 and the hydroxyl group is corroborated by the presence of the density calculated comparing the phases calculated using the diffraction intensity collected (figure 47).

Lissoclimides thermal stability evaluation

The structural information gathered in the previous part of results are just a part of the story about lissoclimides, as anticipated in the material and methods paragraph, the thermal stability induced by the binding of lissoclimides has been investigated using Nano Differential Scanning Fluorimetry. Experimental points, Onset and Inversion, have been derived from the recorded curves plotted in a graphic comparing different values against the control (Ribosomes incubated with DMSO). As shown in figure 48, the general behavior of lissoclimides highlights their tendency to increase the thermal stability of the 80S ribosome in different ways. The most stabilizing congeners are Bromolissoclimide and Fluorolissoclimide, followed by Deoxyfluorolissoclimide showing a weaker stabilization effect. At the end of the list we found, ranked according to their effect of thermal stability: Methyllissoclimide, and the two Haterumaimides behaving in a very similar way. The hydrogen bond network established within the binding pocket seems to play a crucial role in the stability of lissoclimide/80S complexes. As largely discussed in the previous result chapter, Bromolissoclimide and Fluorolissoclimide form the densest H-bond network among all investigated molecules. Their close contacts with the eukaryotic specific protein eL42 grant these molecules a more solid anchorage to the E-site. This fact has an evident effect on thermal stability profiles, pointing to these two congeners as the most stabilizing ones. The rest of the compounds have, DFL excluded, a very similar effect on the stability profiles. The comparison between their structures suggests how the less dense network (compared to BrL and FL) might be the reason of their weaker effect.

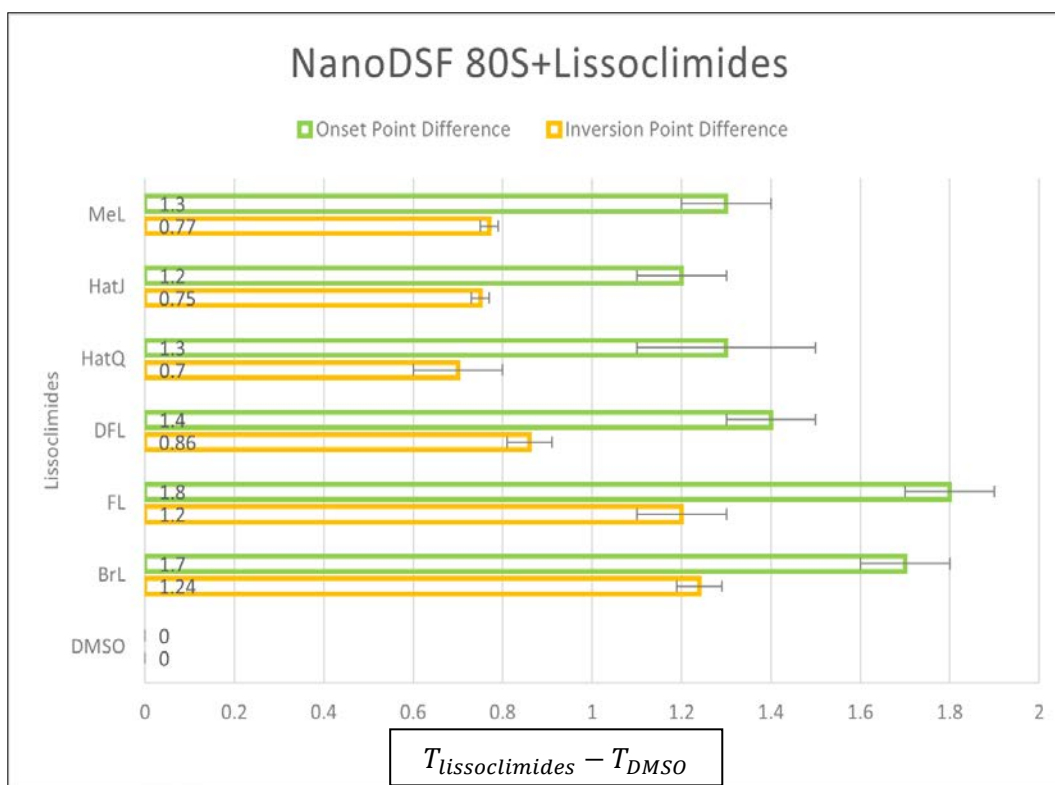


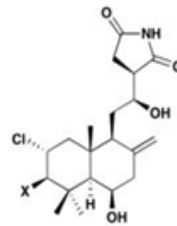
Figure 48 Lissoclimide thermostabilizing effect on the eukaryotic yeast 80S ribosomes. Differences between the onset temperature between lissoclimides and ribosomes incubated with DMSO are plotted in green with their average within the square and relative error bars. In yellow, following the same representation are shown the differences between the inversion point of ribosomes incubated with lissoclimides minus the one of ribosomes incubated with just DMSO.

Lissoclimides cytotoxicity

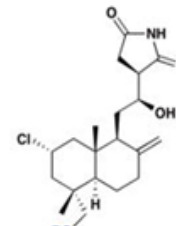
Extensive studies on lissoclimide cytotoxicity have been performed using molecules obtained both from natural sources and total synthesis approaches. The cell line of election for the preliminary studies is the P388 murine leukemia cell line. In literature, the tested molecules are reported to have from sub-nanomolar to several nanomolar IC₅₀ values (Könst et al., 2017; Michalak et al., 2019; Pak et al., 2021; Pellegrino et al., 2019) (figure 49). Despite their general inhibitory ability, some congeners have more

potent effects. It is the case of Haterumaimide-J showing an IC₅₀ of several hundred folds lower than Haterumaimide-Q, 0.5 nM for HatJ and 120 nM for HatQ (Pellegrino et al., 2019; Robert et al., 2006). Chlorolissoclimide and Dichlorolissoclimide have both been reported to have similar inhibitory effect, showing IC₅₀ values of respectively 4 nM and 2 nM (Könst et al., 2017; Pellegrino et al., 2019). Concerning the other lissoclimide molecules object of this studies, preliminary results show interesting features of molecules bearing different halogens. All the molecules have been tested on a translation in vitro system and against the P388 murine leukemia cell line (Data not shown). From the preliminary results, halogenated members of lissoclimides behave in different ways in the two line of experiments. Fluorinated and Brominated members have been shown to hinder the in vitro translation system more than their Chlorinated counterparts. On the contrary in the cytotoxicity assays Haterumaimide-J has been shown to be more effective in cell proliferation inhibition. These results need to be analyzed considering the differences between the in vitro translation systems inhibition and cytotoxicity tests. In the first case all molecules do not need to pass through any cell wall or barrier, while the in vivo tests presuppose a certain permeability for the cellular compartment (Damiani et al., 2019). The conditions in vitro are in general closer to the crystallization ones and trend shown in the thermal stability assays seems to match with the preliminary reports on translation inhibition.

	X	Y	R	P388 IC ₅₀
chlorolissoclimide (CL, 3)	H	Cl	H	4 nM
dichlorolissoclimide (DCL, 4)	Cl	Cl	H	2 nM
3-β-hydroxychlorolissoclimide (5)	OH	Cl	H	NR
haterumaimide A (hatA, 6)	Cl	Cl	Ac	7 nM
haterumaimide N (hatN, 7)	H	Cl	Ac	7 nM
haterumaimide Q (hatQ, 8)	H	H	H	120 nM



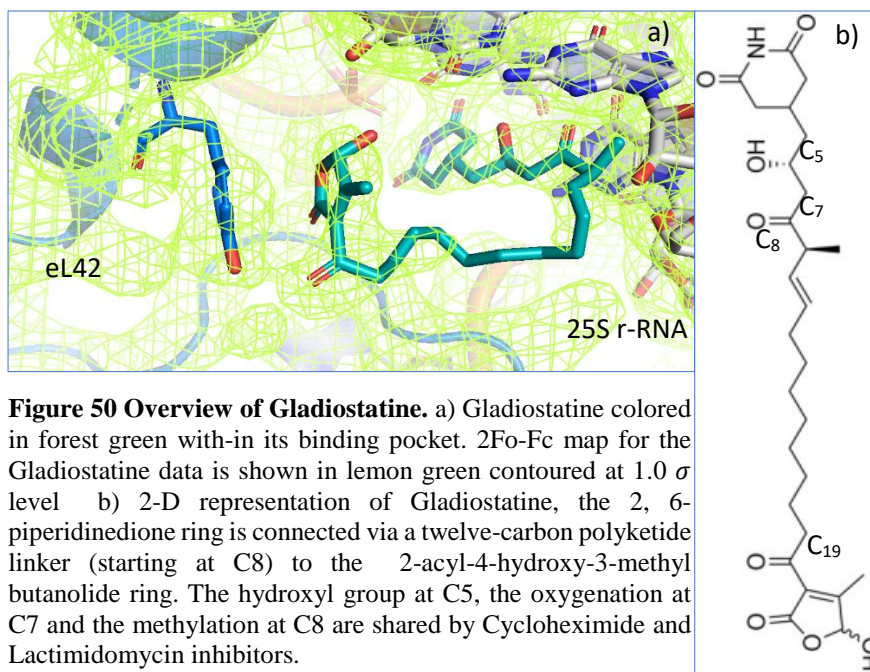
9: X = Cl: hatE (8 nM)
10: X = H: hatF (11 nM)



11: R = H: hatJ (0.5 nM)
12: R = Ac: hatK (1 nM)

Figure 49 Lissoclimide cytotoxicity values. Adapted from Konst et al. Lissoclimides values of half inhibitory concentrations (IC₅₀) assessed on murine leukemia P388 cell lines. Not all compound in the scheme have been structurally studied in this work.

Structure of Gladiostatine in complex with the eukaryotic 80S ribosome



Using *S. cerevisiae* ribosome crystal form, a mode of binding for Gladiostatine has been proposed. As known from literature (Schneider-Poetsch et al., 2010), glutarimide inhibitors bind within the 60S subunit E-site-tRNA pocket (Figure 23). Molecularly, the binding mechanism by which Gladiostatine alter eukaryotic protein synthesis is very similar, in terms of ribosome binding, to the one already described for glutarimide inhibitors. It involves the inhibitor steric clash with the CCA-end of the tRNA entering the E-site. The structure of the 80S ribosome in complex with Gladiostatine have been solved under multiple soaking conditions, as anticipated in the material and methods part, the first data collections showed a difference map peak located within the 60S large ribosomal subunit suggesting the presence of the glutarimide moiety in the same position shown for Cycloheximide and Lactimidomycin. Using the vacant 80S yeast ribosome (PDB: 4V88 (Ben-Shem et al., 2011)) as starting model, the whole Gladiostatine molecule has been fit into the pocket, despite the fact no density for the polyketide tail was present. The following refinements did not show any extra 2Fo-Fc density for the tail. The stepwise increase of Gladiostatine in hard soaking conditions allowed us to find unbuilt and unmodelled density in the proximity of the eukaryotic specific protein eL42; the positive map peak appeared close to the residue

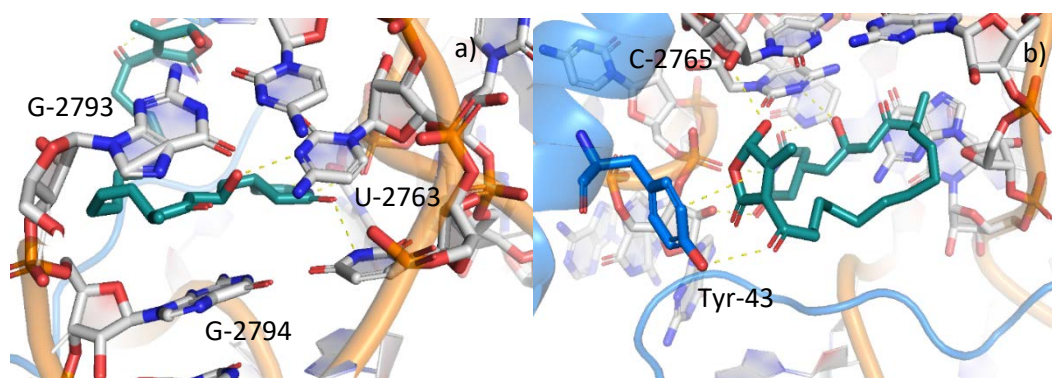


Figure 51 Gladiostatine (GLD) network of interactions within the 60S E-site pocket. a) Network of interaction of Gladiostatine with 25S r-RNA residues. The OH group on C5 establishes an H-bond with C2764, similarly the piperidinedione ring engages the same kind of interaction with U-2763. b) Polyketide tail of GLD extruding towards the solvent side, the 2-acyl-4-hydroxy-3-methylbutenolide ring linked at the end of the tail interacts with the TYR43 of the eukaryotic specific protein eL42. It establishes a $\pi - \pi$ interaction with the aromatic ring of TYR-43 and an extra H-bond with the hydroxyl group of the same residue, moreover the hydroxyl group in position three on the ring gets in touch with the OH group on the ribose of C2765.

tyrosine 43 (figure 50). The shape of the electron density suggested the presence of the specific *2-acyl-4-hydroxy-3-methyl butanolide* ring of Gladiostatine. Several cycles of refinement gave as a result a partial density for the whole molecule, leaving completely uncovered three carbon atoms in the polyketide tail as shown in figure 50. The conformation within the binding site is close to the one of its glutarimide relatives, as discussed later on. The 2-6 piperidine-dione moiety interacts with the phosphate backbone of G92 and C93, in addition to the nucleobase U2763. The hydroxyl group on the polyketide tail seems to engage in a hydrogen bond with C2764, this behavior has been observed in case of Lactimidomycin and Cycloheximide as well (figure 51, figure 52). Concerning the oxygen on C-16, it can, and according to the orientation and distance in the model, does establish hydrogen bonds with the ammino group of G2764. The long polyketide tail then takes the path of the solvent side to finally interact via the 2-acyl-4-hydroxy-3-methylbutenolide ring with TYR43 of eL42 (figure 51). Due to the poor quality of the electron density map, the only statements possible might just fall in the domain of speculation. The π -orbital on the 2-acyl-4-hydroxy-3-methylbutenolide ring could interact with the π system of TYR43. In addition, the hydroxylation on position 4 on the ring seems capable of different interactions with the OH group of TYR43, but also with the OH group of the nucleic acid residue of C2765. The flexibility given by the polyketide tail, as shown in figure 52, is probably the reason why the density relative to this part is not well defined. The interaction with eL42 might also be unspecific and the high concentration reached during the soaking experiments responsible for the density in proximity of TYR43.

Superimposing the already solved structures from Cycloheximide (PDB 4U3U, 5LSK) and Lactimidomycin (PDB 4U4R), it is possible to appreciate the similar rearrangement of the binding pocket. The moiety in common to all inhibitors sits in almost an identical manner regarding the interactions with G2764 establishing the same hydrogen bond network. Regarding the piperidinedione ring it is positioned, for all three molecules, in the same orientation making the same contacts. For CHX and LMT the binding pocket show

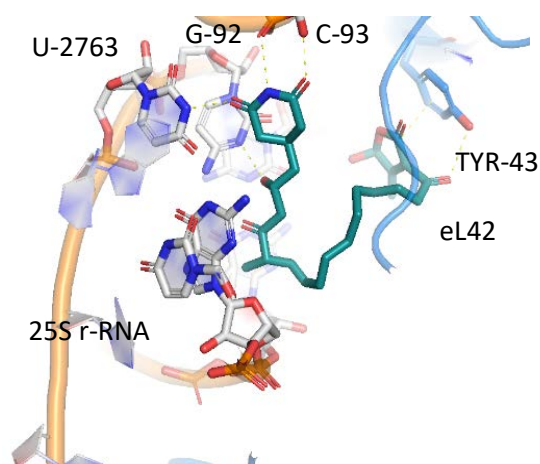


Figure 52 Gladiostatine network of interactions. Bottom view of Gladiostatine in its binding pocket. Interaction with the 25S rRNA in particular with G-92 and G-93 nucleobases are highlighted. Protein eL42 and Tyr43 interaction with GLD are shown in the background.

three magnesium atoms, in GLD structures modelled as a spermidine molecule. Despite this difference, no interaction between GLD and the polyamine are detected. The polyketide tail of Gladiostatine along with the lactone ring of Lactimidomycin move towards the E-site pointing to the solvent. The lactone ring does establish a hydrogen bond with the hydroxyl group on the sugar moiety of G2793, Gladiostatine on the contrary could not make any contact on its way to the solvent side, probably adopting several conformations that only at high concentrations led to the formation of the 2-acyl-4-hydroxy-3-methylbutenolide network of interactions (figure 53). As reported in literature (Nakou et al., 2020), Gladiostatine is mildly affecting *Saccharomyces cerevisiae* growth, but it shows a potent effect on several cancer cell lines. Due to the similarity between *H. sapiens* and *S. cerevisiae* E-sites, the reason of these differences is unlikely due to differences among the different ribosomes, but most probably to other mechanisms involved in cell proliferation. The cell wall permeability or the different types of transport under which this molecule is brought inside the cell compartment might be the main cause of the discrepancies between cancer cells and yeast' ones. To better understand this particular issue more studies focusing on the different pathways with which Gladiostatine interferes are needed, especially on its strong effect on cell migration as reported (Nakou et al., 2020).

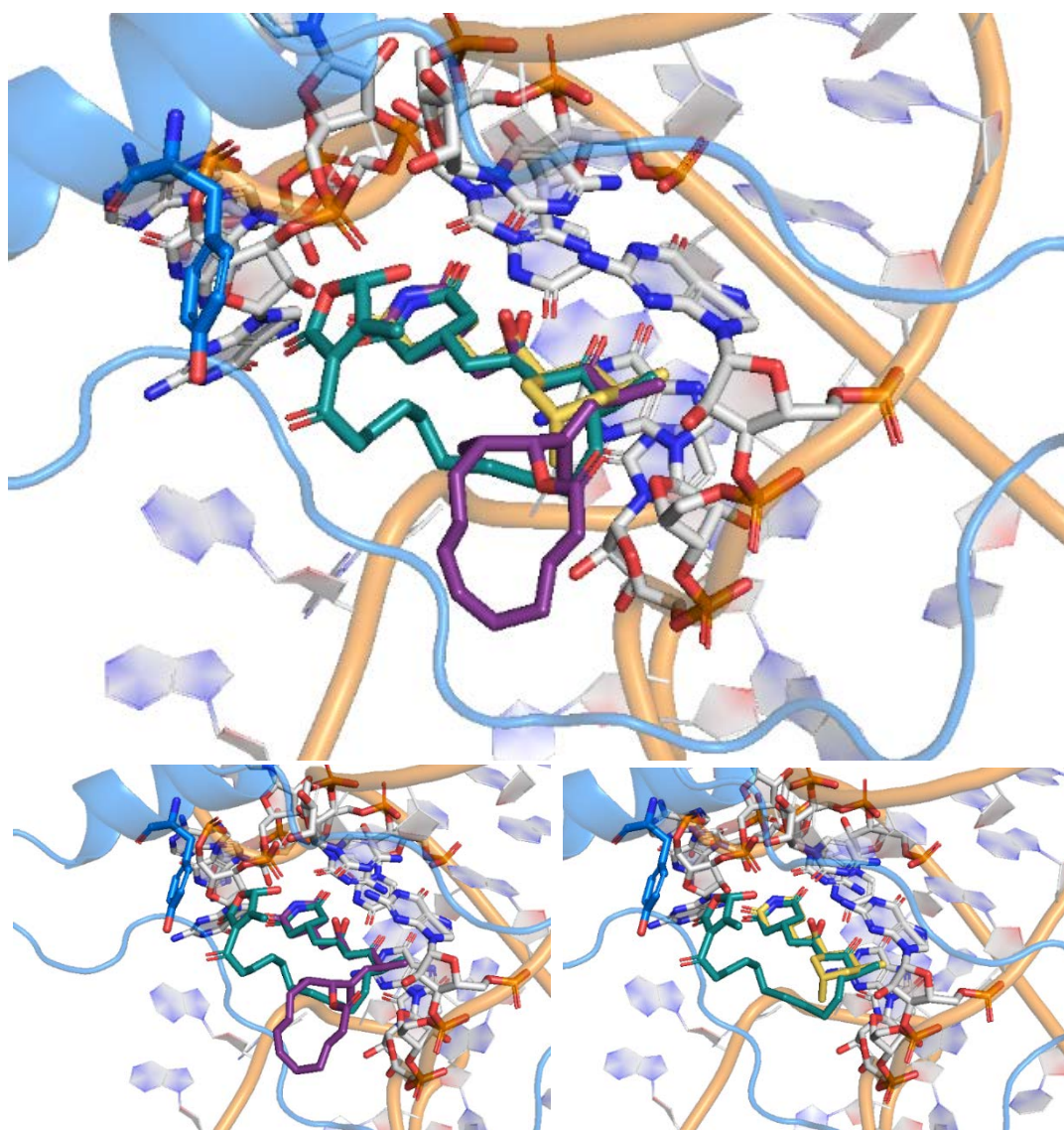


Figure 53 Structural superimposition of glutarimide inhibitors. a) Gladiostatine (GLD) in green forest, Lactimidomycin (LMT PDB: 4U4R) in purple and Cycloheximide (CHX PDB: 4U3U) in ocher occupy the same binding site in the 60S ribosomal subunit, sharing part of their interaction network. b) GLD and LTM superimposition (RMSD: 0.35 Å) the bulky lactone ring of LMT and the polyketide tail of GLD take the same direction towards the solvent side. c) GLD and CHX superimposition (RMSD: 0.28 Å) the common moieties align within the pocket and interact with the rRNA residues in an identical manner.

Conclusions and perspectives

The inhibition of protein synthesis has broadly demonstrated its potential in the fight against cellular malignancies (Myasnikov et al., 2016; Yusupova et al., 2021). Targeting the translational apparatus in cancer is not only a research topic, but the reality in the life of many people benefiting the effects of such treatments. Enhancing the efficiency of new drugs and ideally reducing their side effects is a task that needs precise optimization and deep knowledge of the molecular mechanisms involved. Here, we have provided structural information concerning seven different molecules that have shown their efficacy against different cancer cell lines (Könst et al., 2017; Nakou et al., 2020; Pellegrino et al., 2019; Robert et al., 2006). Additionally, the evaluation of the thermal stability change induced upon binding has been quantified using Nano Differential Scanning Fluorimetry underlining the paramount importance of the H-bond networks established within the binding pocket. The comparison between the structural arrangement unveiled by X-ray crystallography and the thermostability assays suggests a correlation between H-bond and complexes thermal stability: the denser the interaction network, the stronger the effect of thermal stability. Halogen substitutions play a central role anchoring lissoclimides at their binding site, as shown by the comparison between halogen and non-halogen bearing lissoclimide bound to the 80S yeast ribosome. The thermodynamic characterization of Haterumaimide-J binding using Isothermal Titration Calorimetry, revealed the exergonic nature of its interaction with the E-t-RNA binding site in the large ribosomal subunit. This powerful technique is often used in structural biology with great success. Unfortunately, it requires enormous quantities of material to be performed on a system like ribosome complexes. Despite this fact, a deeper study of the thermodynamic properties of the interaction between lissoclimides and the ribosome is not only interesting, but also beneficial for the future developments in the design of new congeners. The importance of halogen substitutions in pharmaceutical and bioactive molecules has been pointed out in several publications (Benedetto Tiz et al., 2022). Chlorine and bromine are often found in biologically active metabolites, on the contrary iodine and fluorine stay more unusual among natural occurring molecules (Cabrita et al., 2010). Despite the fact that chlorine is definitely more concentrated than bromine in sea water, this last atom is more frequently found as a substituent in algae organ-halogenated compounds (Neumann et al., 2008). Only few examples of

fluorinated natural occurring molecules have been reported in literature (Carvalho and Oliveira, 2017). Despite this fact fluorine is broadly implied in modern medicinal chemistry as suggested by the number of fluorine bearing drugs approved by FDA in the last two years, 14 in 2021 and 13 in 2020 (Benedetto Tiz et al., 2022; Mei et al., 2019). None of these molecules possessed iodine or bromine. The use of different halogen has been proved to increase the bioavailability of pharmaceutical molecules. Notably fluorine substitutions have been reported to increase the permeability of lymphocyte cell walls in molecules used to inhibit the inverse transcriptase of HIV-1. The different behavior of lissoclimide in vitro and in vivo inhibitory assays might have origin from the permeability of cell membranes. Despite the fact that fluorine should increase the permeability of the cell wall, from the preliminary results of the cytotoxicity tests, this behavior seems to not be respected in lissoclimides' case (Benedetto Tiz et al., 2022). The central importance of hydrogen bond interactions in the substrate recognition finds one more corroborating evidence in the structural and biophysical investigation conducted on lissoclimide molecules.

Gladiostatine in complex with the 80S ribosome has been solved at a medium resolution. This cut-off combined with the flexibility of its polyketide tail did not allow us to make strong conclusions on its mode of binding, most probably α -specific for its 2-acyl-4-hydroxy-3-methyl butanolide linked to the tail. As reported in literature (Nakou et al., 2020) the effect of this glutarimide inhibitor is stronger on higher eukaryotes cells than yeast one. The reason of the differences observed in the cytotoxicity assays might rise from specific mutations in the protein environment around the higher-eukaryotes E-site pocket. In the perspective of gaining a better understanding of the binding of these molecules further studies can be suggested, especially for Gladiostatine. The recent advances in cryo-electron microscopy allowed this technique to reach unprecedented precision in the determination of the three-dimensional structures of macromolecular complexes (Myasnikov et al., 2016). The issue of the flexibility of the polyketide tail along with a more detailed view of the lissoclimide binding pocket could be addressed using this technique.

Research Project 2

*Structural and Biophysical
characterization of ribosome tetramers
derived from chicken embryos exposed to
hypotermia*

Aim of the project

Chicken ribosome tetramers constituted one of the first experimental prove that ribosomal particles were crystallizable entities (Byers, 1966). Their potential use in structural biology was extensively assessed by different groups during thirty years (Barbieri, 1979; Byers, 1971; Milligan and Unwin, 1986; Morimoto et al., 1972a). These studies provided relevant information about the three dimensional organization of the ribosome (Milligan and Unwin, 1986). Researchers have been investigating not only the physiological function of tetramers, but also how the para-crystalline sheets they form in vivo play a role inside embryonic cells. They provided a conspicuous corpus of evidences and built several hypothesis (Barbieri, 1974). Unfortunately, in that period all the tools in structural, molecular and cellular biology were not as powerful as nowadays. The lack of high-resolution techniques in these fields let a high number of questions unsolved. The fascinating process of crystallization involves complex changes in the environment conditions that would allow the phase transition of the specimen into a new and ordered array of molecules. As introduced in the previous chapters, the flexible nature of the expansion segments has been detrimental in the deciphering of their three-dimensional arrangement and thus of their role. The unique features of the tetramer assembly suggest the possibility of a stable arrangement of these tentacle-like structures at the interface between monosomes. The aim of this project is to produce a stable purification protocol able to yield tetrameric particles suitable for Cryo-electron microscopy studies with the ultimate goal of understanding their fine three-dimensional arrangement at the molecular level. Unveiling their structure will help shedding light upon their function within the embryonic cellular compartment.

Materials and Methods Project 2

Chicken ribosome complexes purification

Fertilized eggs from Gallus-Gallus were incubated at 37°C for hundred twenty hours (five days) paying attention to the humidity levels in the incubator. At day 5 eggs were placed at 4°C and let to cool down for twenty-four hours, this triggers ribosome tetramerization and bidimensional crystal formation (Byers, 1966). Eggs were then opened in a precooled Petri dish, the embryo removed from the amnion using a surgical clamp, washed with buffer A and placed in a sterile falcon containing buffer B. From hundred to hundred fifty embryos were extracted. Before starting the lysis process protease and RNA-

<i>Buffer A</i>	
Compound	Concentration
Hepes/KOH pH 7.2	30 mM
KCl	150 mM
MgCl ₂	10 mM
EDTA	0.5 mM
DTT	1 mM
<i>Buffer B</i>	
Compound	Concentration
Hepes/KOH pH 7.2	30 mM
KCl	150 mM
MgCl ₂	10 mM
Sucrose	250 mM
EDTA	0.5 mM
DTT	1 mM

ase inhibitors were added to the mix to preserve ribosome integrity. One volume of buffer B was added to the solution containing embryos and the lysis performed in a loose fit cell homogenizer. Ten rapid strokes were enough to break tissues and cell walls. The obtained lysate was then centrifuged at 4500 rpm for 15 minutes and the supernatant removed. The debris containing cell walls, nuclei and unbroken cells were re-dissolved in buffer B and re-homogenized with the loose fit cell breaker, avoiding the nuclei rupture and recovering as much material as possible. The cell lysate was centrifuged at 16000 rpm for 30 minutes and the S30 fraction recovered with a long needle and filtered with a 5 µm filter to remove big albumin aggregates. At this point the purification process took two different paths. In the first one the filtration process started using a 100 KDa cut-off filter. The S30 fraction has been concentrated and small proteins eliminated in the filtrate. Averagely 8 mg of material per tube were loaded onto 20-40 % sucrose gradient and spun for thirteen hours at 18000 rpm using a SW28 swinging rotor. The gradients were then fractionated from the bottom using a BioRad fraction collector with a fraction volume of 0.5 ml. Profiles were recorded using a NanoDrop device plotting the A_{260} against the fraction number (figure 54). Fractions of interest were pulled together and concentrated against buffer B, at this purification step

full peaks were collected. The first peak starting from the bottom gradient contained particles with an approximate Svedberg coefficient of 170S identifiable with ribosome tetramers. The second peak contained the single monosomes. After concentration via 100 KDa filter, the ribosome containing solutions was loaded again onto 20-40% sucrose gradients and spun for thirteen hours at 18000 rpm in smaller tubes loading approximately 1 mg of ribosomes per gradient. Gradients were fractionated using the same device instead set to give fractions of approximately 300 μ L. Only peak fractions having optical absorbance at 260 nm higher than the half of the maximum peak value were collected and pulled together. Buffer containing sucrose was exchanged with buffer D, lacking any kind of sugar in its composition, concentrated until the desired concentration (2 mg/ml) and flash frozen in liquid nitrogen.

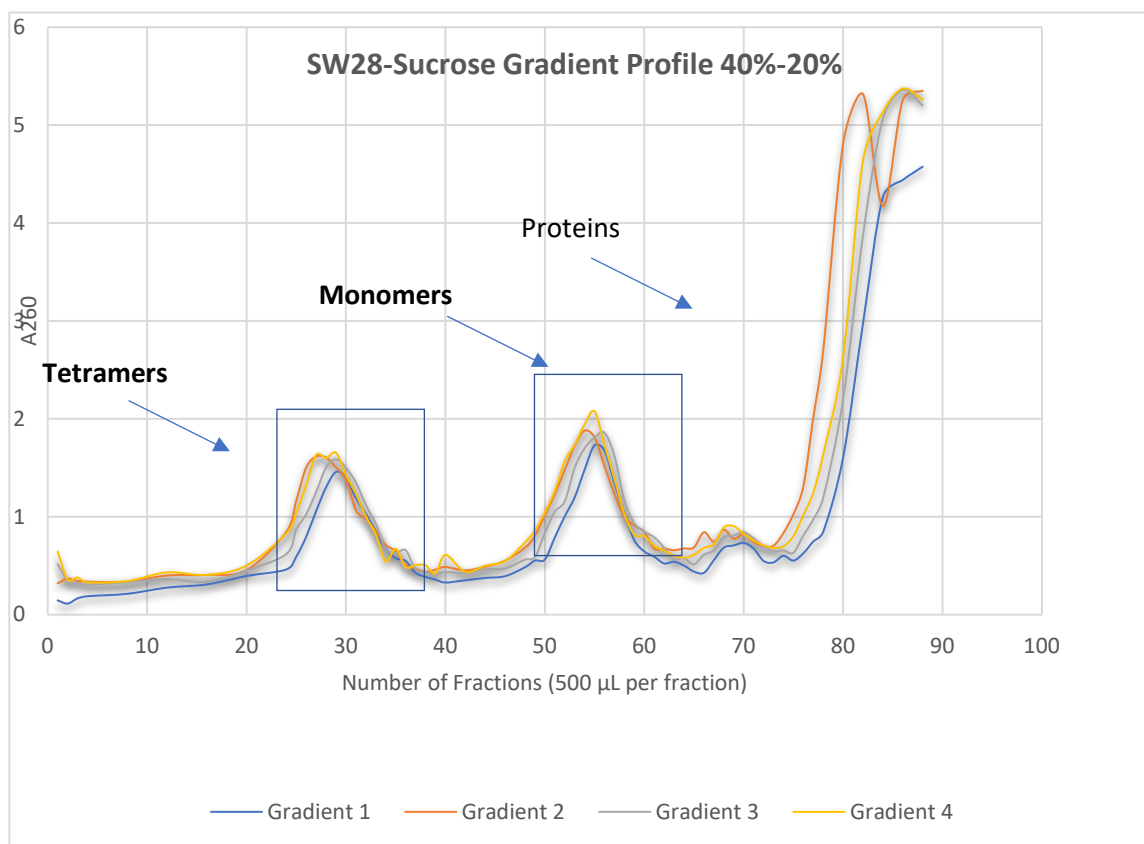


Figure 54 40-20% sucrose gradient profiles of concentrated S30 fraction. The first peak from the bottom represents the tetrameric content of the S30 fraction, the second and lighter peak is constituted of 80S monosomes and the shoulder at the top of the gradient is enriched in protein content. Peaks inside rectangles have been pulled together.

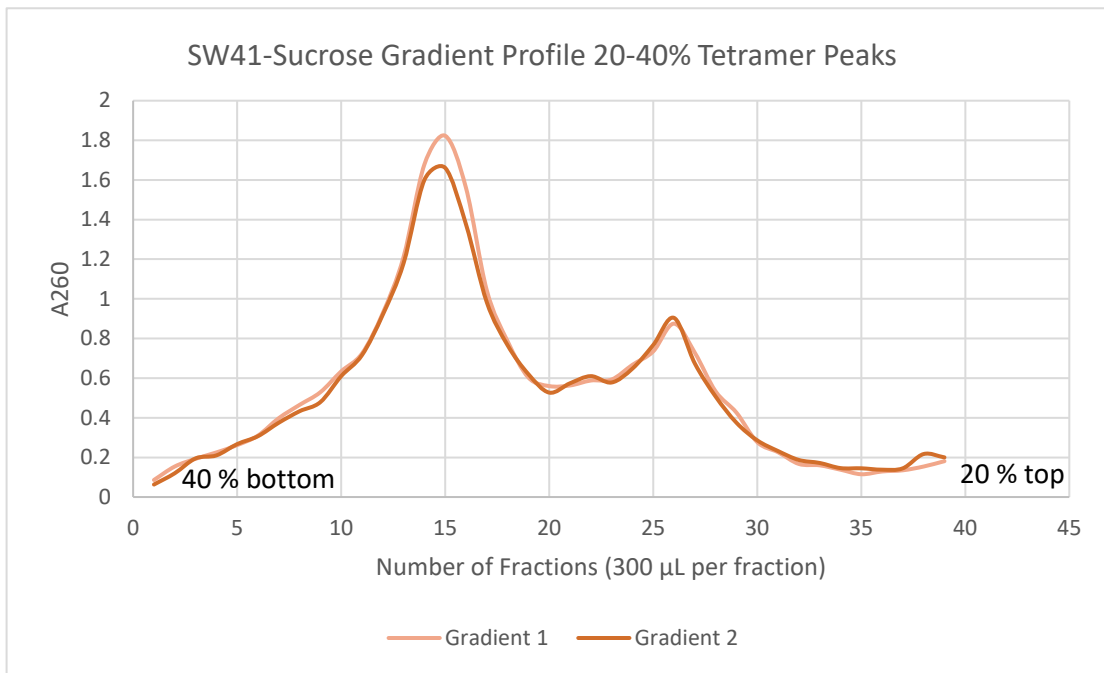


Figure 55 40-20% sucrose gradient profiles of pulled and concentrated tetrameric peaks in figure 54. The first peak contains tetrameric particles, the second and lighter peak is constituted of 80S monosomes coming either from the tail of the tetramer peak or from their dissociation.

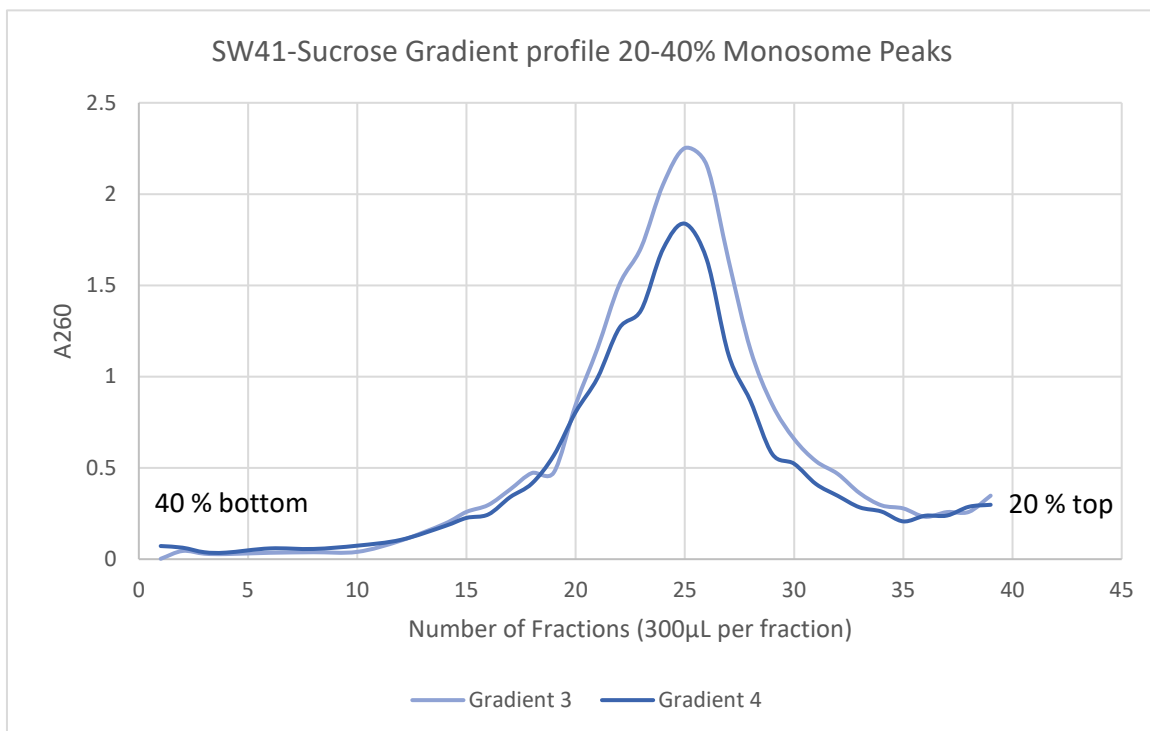


Figure 56 20-40% sucrose gradient profiles of pulled and concentrated monomeric peaks in figure 54. The peak is constituted of 80S monosomes as shown by the sedimentation behavior, identical to the one shown for the second peak in figure 52.

The tetrameric complex has also been purified following another procedure. After filtration through the 5 μm the S30 fraction has been carefully deposited on a cushion of solution C containing 2 M sucrose. The S30 fraction was spun at 45000 rpm for 4 hours and 30 minutes in the fixed angle rotor Ti 50.2. The final

<i>Buffer C</i>	
Compound	Concentration
Hepes/KOH pH 7.2	30 mM
KCl	150 mM
MgCl ₂	10 mM
Sucrose	2 M
EDTA	0.5 mM
DTT	1 mM

product was a transparent pellet constituted of ribosomes in all aggregational states. The containing protein solution kept separated from the ribosomal pellet using the cushion layer, lately discarded putting centrifuge tubes upside down. The pellet was kept on ice and re-dissolved in buffer D, with the same composition as buffer B but without any sucrose. The ribosome concentration was then estimated using Nanodrop, averagely from four to twelve milligrams of ribosomes were obtained at this step. This material has been layered onto 20-40% sucrose gradient and spun overnight at 18000 rpm for fourteen hours in the SW41 rotor. Fraction were collected as before and the absorbance at 260 nm estimated and plotted against fraction number (figure 57).

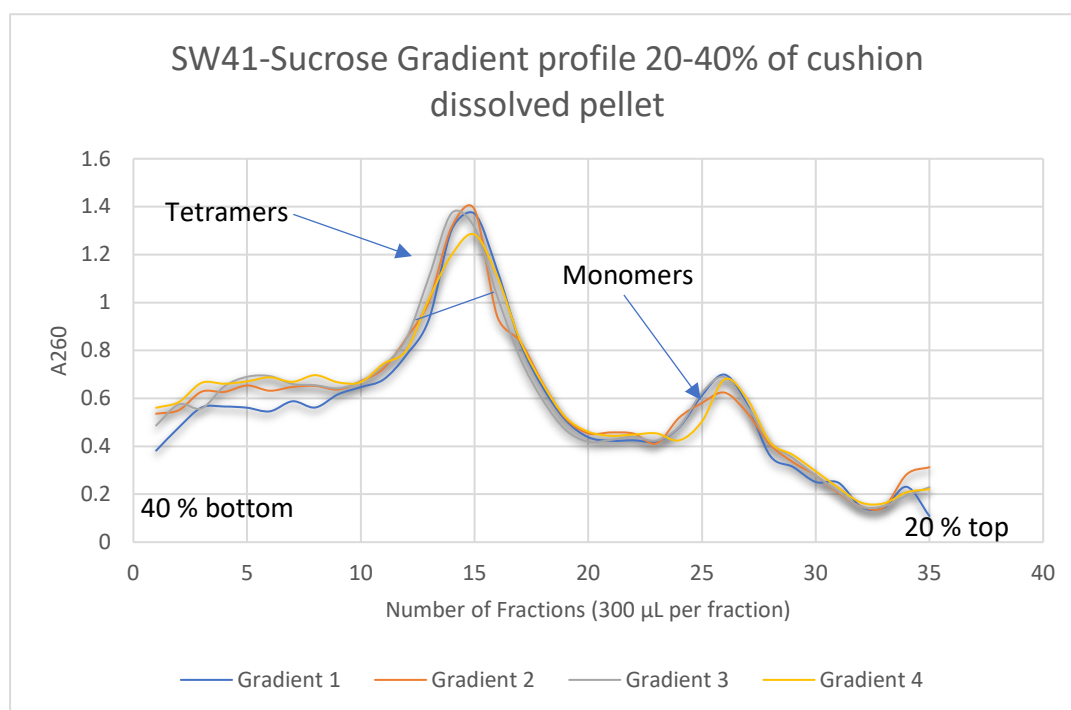


Figure 57 40-20% sucrose gradient profile of dissolved ribosomal pellet recovered after sucrose cushion. The profiles show two separate peaks as previously seen in figure 5 and figure 6. The comparison with figure 6 shows an increased absorbance for the baseline at the bottom of the tube, probably due to tetramers aggregation during the cushion step.

The same rule used for fraction selection was used as before, peak fractions collected and concentrated using 100 KDa cut-off filters. Both peaks were collected separately, the tetramer peak and the monosome one. During the concentration process buffer containing sucrose was exchanged with buffer D. Once the desired concentration was reached, 2 mg/ml, the sample was flash frozen in liquid nitrogen and stored at -80° C, ready for further investigations.

<i>Buffer D</i>	
Compound	Concentration
Hepes/KOH pH 7.2	30 mM
KCl	150 mM
MgCl ₂	10 mM
EDTA	0.5 mM
DTT	1 mM

Chicken Ribosome Complexes Characterization

Material coming from different peaks has been analyzed using the standard methods in structural and molecular biology. Protein content has been firstly investigated via 15 % SDS-page gel in denaturation conditions showing the characteristic presence of ribosomal proteins and several contaminants. rRNA integrity has been assessed via 1% agarose gel showing not only the absence of rRNA degradation, but also confirming its ribosomal nature (figure 58). Shape and size of the heaviest peak have been first roughly determined using dynamic light scattering, a technique that can answer questions relative to physical characteristics of the specimen under study, but

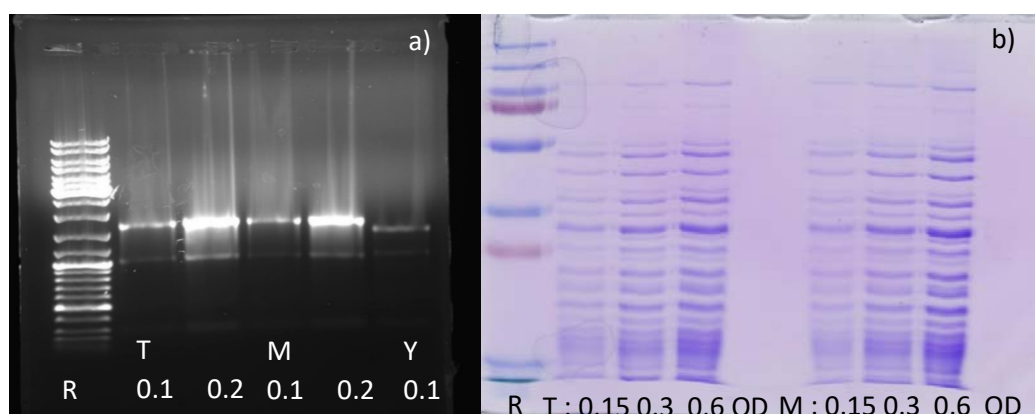


Figure 58 Chick ribosome gels. a) 1% Agarose gel in denaturation condition for rRNA quality check: in order the ruler, 0.1 and 0.2 A₂₆₀ OD from the tetramer peak, 0.1 and 0.2 A₂₆₀ OD from the monomer peak and yeast ribosome rRNA as a control. b) 15% SDS-Page gel, in the first three lines different amounts of material coming from tetramers peak and in the last three material coming from the monomer peaks.

also about the purity of the sample under question. Measurements have been taken using the instrument (DynaPro Wyatt instruments) in 10 duplicates. The hydrodynamic particle radius is in good agreement with the expected value of 300 Å (figure 59). The sample appeared to be monodispersed and pure enough to proceed with visual examination on negative stained carbon grids.

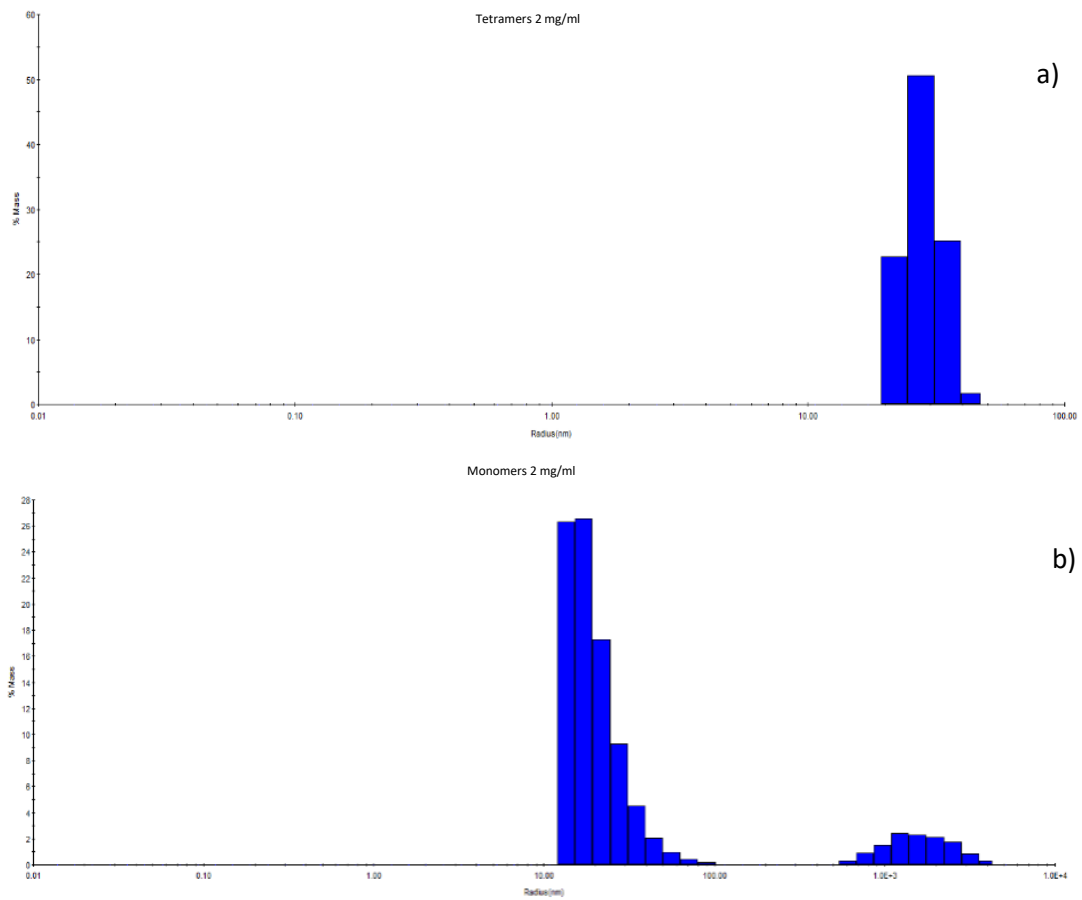


Figure 59 Dinamyc Light Scattering (DLS) plot of chicken tetramers and monomers at 2 mg/ml. a) Tetramers show a good level of homogeneity with a hydrodinamic radius of averagely 300 Å. b) Monomers show a good level of homogeneity, but heavier aggregates are present within the sample.

Mass spectrometry

Mass spectrometry allows to identify the protein content of a sample with a certain level of precision related to the database against which the experimental values are compared, as later explained in this session. Ribosomal proteins and contaminants have been identified in the ribosome's tetramer sample and compared with the ribosomal proteins and contaminants detected in 80S ribosomes.

Sample digestion

The protein mixtures were precipitated with TCA 20% overnight at 4°C and centrifuged at 14,000 rpm for 10 min at 4°C. The protein pellets were washed twice with 1 mL cold acetone and air dried. The protein extracts were solubilized in urea 2 M, reduced with 5 mM TCEP for 30 min and alkylated with 10 mM iodoacetamide for 30 min in the dark. Trypsin digestion was performed at 37°C and an overnight with 500 ng trypsin (Promega, Charbonnières les Bains, France). Peptide mixtures were then desalted on C18 spin-column and dried on Speed-Vacuum.

LC-MS/MS Analysis

Samples were analyzed using an Ultimate 3000 nano-RSLC coupled in line, via a nano-electrospray ionization source, with the Orbitrap Exploris 480 mass-spectrometer (Thermo Fisher Scientific, Bremen, Germany) equipped with a FAIMS (high Field Asymmetric Ion Mobility Spectrometry) module. Peptide mixtures were injected in 0.1% TFA on a C18 Acclaim PepMap100 trap-column (75 µm ID x 2 cm, 3 µm, 100Å, Thermo Fisher Scientific) for 3 min at 5 µL/min with 2% ACN, 0.1% FA in H₂O and then separated on a C18 Acclaim PepMap100 nano-column (75 µm ID x 50 cm, 2.6 µm, 150 Å, Thermo Fisher Scientific) at 300 nL/min and 40°C with a 90 min linear gradient from 5% to 30% buffer B (A: 0.1% FA in H₂O / B: 80% ACN, 0.1% FA in H₂O), regeneration at 5% B. Spray voltage were set to 2.1 kV and heated capillary temperature at 280°C. For the FAIMS module, a combination of two Compensation Voltage (CV), -40 V and -55 V, was chosen with a cycle time of 1 second for each. For the full MS1 in DDA mode, the resolution was set to 60,000 at m/z 200 and with a mass range set to 350-1400. The full MS AGC target was 300% with an IT set to Auto mode. For the fragment spectra in MS2, AGC target value was 100% (Standard) with a resolution of 30,000 and the maximum Injection Time set to Auto mode. Intensity threshold was set at 1E4. Isolation width was set at 2 m/z and

normalized collision energy was set at 30%. All spectra were acquired in centroid mode using positive polarity. Default settings were used for FAIMS with voltages applied as described previously, and with a total carrier gas flow set to 4.2 L/min.

Mass spectrometry data analysis

Proteins were identified by database searching using SequestHT (Thermo Fisher Scientific) with Proteome Discoverer 2.5 software (PD2.5, Thermo Fisher Scientific) on *Gallus gallus* database downloaded from UniProt (unreviewed, release 2022_03_28, 25236 entries). Precursor and fragment mass tolerances were set at 10 ppm and 0.02 Da respectively, and up to 2 missed cleavages were allowed. For all the data, Oxidation (M, +15.995 Da) was set as variable modification, and Carbamidomethylation (C, + 57.021 Da) as fixed modification. Peptides and proteins were filtered with a false discovery rate (FDR) at 1%. Label-free quantification was based on the extracted ion chromatography intensity of the peptides. All samples were measured in technical triplicates. The measured extracted ion chromatogram (XIC) intensities were normalized based on median intensities of the entire dataset to correct minor loading differences. For statistical tests and enrichment calculations, not detectable intensity values were treated with an imputation method, where the missing values were replaced by random values similar to the 10% of the lowest intensity values present in the entire dataset. Unpaired two tailed T-test, assuming equal variance, were performed on obtained log₂ XIC intensities.

Table 11 In table ribosomal protein identified by LC-MS analysis. In the first and third columns the gene names of proteins belonging either to the large subunit (first column), or to the small subunit (fourth column), in the third and sixth column their PSM

Ribosomal Identified Proteins					
Gene Name	Protein Name	PSM	Small Subunit	PSM	Protein Name
RPL3	uL3	1891	RPS2	636	uS2
RPL4	uL4	858	RPS3A	410	eS1
RPL6	eL6	1432	RPS3	440	uS3
RPL7A	uL8	1448	RPS6	143	eS6
RPL8	uL1	989	RPS7	146	eS7
RPL9	uL6	391	RPS8	789	eS8
RPL10A	uL1	522	cRPS11	668	uS17
RPL11	uL5	479	RPS10	294	eS10
RPL12	uL11	629	RPS12	338	eS12
RPL13	eL13	1407	RPS14	425	uS15
RPL14	eL14	603	RPS15A	941	uS8
RPL15	eL15	432	RPS16	986	uS9
LOC107049046 L17	uL22	747	RPS19	916	eS19
RPL18A	eL20	486	RPS20	410	uS10
RPL19	eL19	505	RPS21	440	eS21
RPL21	eL21	531	RPS23	143	uS12
RPL22 L1	eL2-like	372	RPS24	146	eS24
RPL22	eL22	132	RPS25	789	eS25
RPL23	uL14	716	RPS26	25	eS26
RPL23A	uL23	1112	RPS27L	181	eS27-like
RPL24	eL24	530	RPS27	101	eS27
RPL26L1	eL26-like	1024	RPS28	483	eS28

RPL27	eL27	541	RPS29	98	eS29
RPL27A	uL15	417	FAU S30	117	eS30
RPL31	eL31	558			
RPL32	eL32	926			
RPL34	eL34	855			
RPL35	uL29	346			
RPL36A	eL42	735			
RPL35A	eL33	282			
RPL37	eL37	18			
RPL37A	eL37-a	298			
RPL38	eL38	456			
RPLP0	uL10	1197			
RPLP2	P2	488			
UBA52 L40	eL40	134			

Negative Stain Grids

Tetramer's containing solution at concentration of 0.3 mg/ml was diluted until 0.03 mg/ml and stained with uranyl acetate. Images were collected on Tecnai F20 twin equipped with a field emission gun operating at 200kV and a camera GATAN US10001 with a magnification of 50000X, corresponding to a pixel size of 2.12 Å . Grids show a sample constituted of two different kind of ribosomal particle identifiable with 80S monosomes and tetrameric aggregates of 80S ribosome (figure 60). This experiment confirmed what previously shown by agarose gel, the second peak from 40%-20% sucrose gradient contains ribosomal particles, specifically aggregating to form tetramers as shown in figure 12.

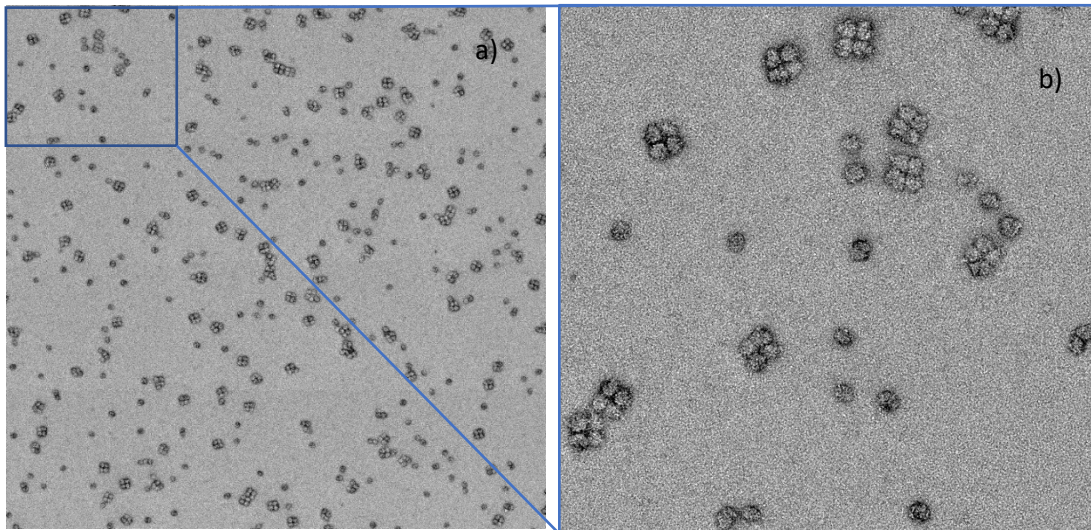


Figure 60 Negative stain micrographs of chick tetrameric complexes. a) Micrograph showing tetrameric and monomeric ribosomes, is it possible to notice aggregates of tetramers, likely coming from bidimensional crystal sheets. b) zoom-in of negative stained micrograph with well separated tetramers are visible.

Grids preparation and screening on Glacios.

(Melnikov et al., 2012) ComQF+thinC R 2/2, Au_300 mesh carbon coated grids were cleaned and charged using the Model 1070 Nano-Clean from Fischione Instruments available at the integrated structural biology (IBS) platform at IGBMC. Sample deposition was performed using the Vitrobot system present on the IBS platform (“Vitrobot | Cryo EM Sample Preparation - FR,” n.d.), 3 μL of sample were deposited at different concentrations (0.15, 0.3 and 0.5 mg/ml). Vitrobot parameters were set as follow:

- Temperature 5°C
- Humidity 95-100 %
- Deposition time 30 s
- Blotting Force 5
- Blotting Time 2 s

After sample deposition, grids were flash frozen in liquid ethane and stored in liquid nitrogen. Grid clipping was performed before the screening session on Glacios microscope equipped with:

- field emission gun X-FEG operating at 200 kV,
- K2 summit electron counting direct detection camera
- CETA-D electron diffraction detector

After a first screening (figure 61), the best grid frozen at 0.5 mg/ml was chosen, the data collection strategy set and the data collected with the following relevant parameter for data processing :

- Accelerating voltage: 200 kV
- Spherical aberration: 2.7 mm
- Pixel size: 0.901 Å
- Total exposure: 41 $\frac{e}{\text{Å}^2}$

Gain images were collected and 3828 movies recorded and on-the-fly processed using Cryo-Spark live showing that all orientations were present.

Data Processing data collected on Glacios.

Collected data were further processed using Cryo-Spark. The data processing workflow included the import of recorded movies, their patch motion correction and contrast transfer function calculation of every image extracted from movies. Particle picking has been firstly performed running the blob picker job available on Cryo-spark, setting the blob parameters at 700 Å for the inner radius and 1200 Å for the outer one. Particles have been extracted from micrographs using a box with a size of 1200 Å, cropped down four times for computational reasons. The number of movies collected and the final number of particles extracted would not allow the high resolution to be reached. The extracted particles have been classified in 2D classes furtherly narrowed and selected to undergo to the ab-initio volume calculation. This particular step is fundamental in

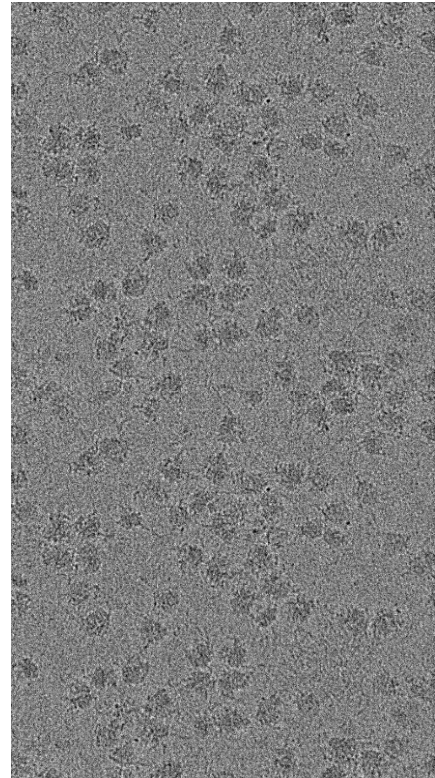


Figure 61 Micrographs collected on Glacios at IGBMC. Tetrameric formations are visible and can be distinguished from single 80S ribosomes.

the other step of structure determination. It will provide the template to which the particles will be aligned and refined in the homogeneous refinement step (Punjani et al., 2017). Despite the fact that only the classes carrying the features observed in negative stained grids have been selected for ab initio, this step shows some peculiarities leaving unanswered the question about detailed features of the whole complex organization as shown in figure 62. Different particle extraction strategies have been applied to overcome this computational issue, but none of them improved the previously obtained 3D volume used for refinement.

**Import Movies – Motion Correction – CTF calculation
Particle Extraction**

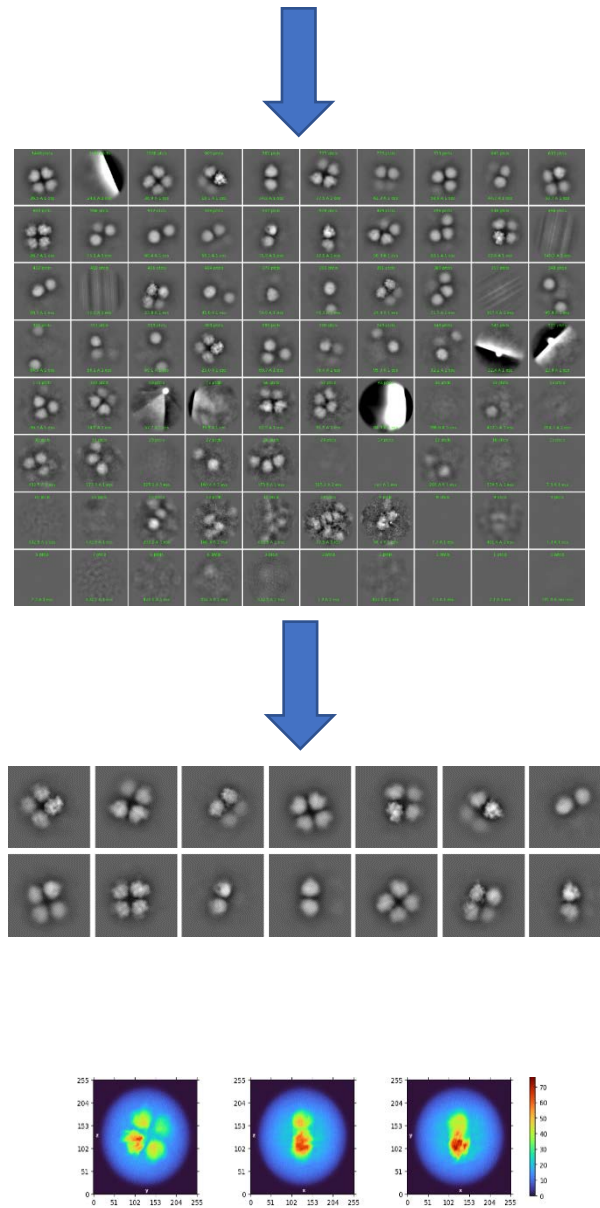


Figure 62 Work flow of data processing performed on the dataset collected on Glacios at IGBMC. a) 2D classification after Motion Correction and CTF calculation shows bidimensional particles clustered according to their similarities. b) The 2D classification is narrowed down using prior knowledge on the complex composition.

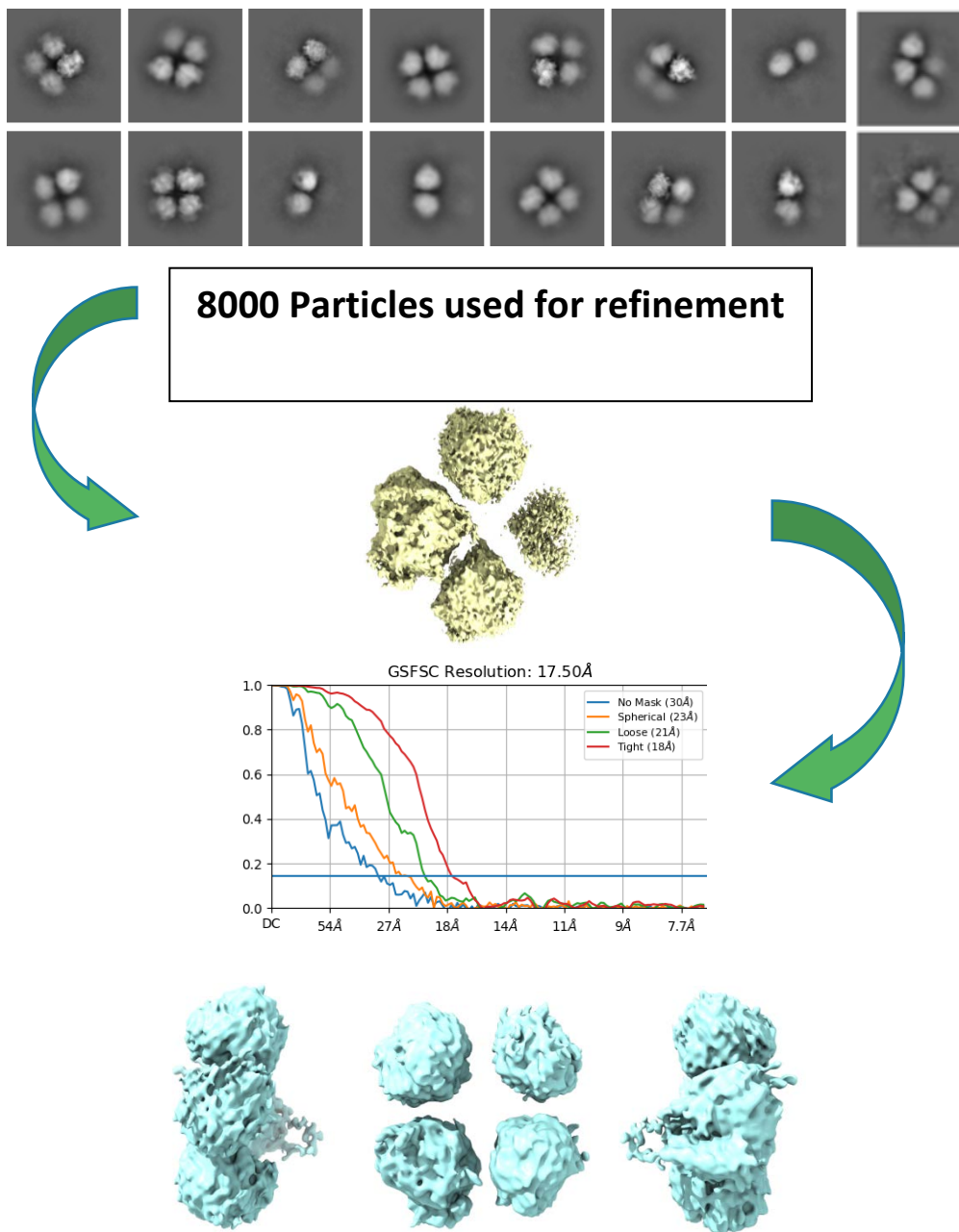


Figure 63 Tetramers homogeneous refinement workflow. a) 8000 Particles belonging to the 2D classes were refined against the volume obtained from the ab initio reconstruction. b) Fourier Shell Correlation and m , the golden number of 0.143 for FSC has been hit at 17.5 Å resolution which did not allow the calculation of any mask. c) Three different orientation of the reconstructed volume at 17.5 Å

using the volume in figure 63 a template has been generated and used to re-pick particles and extract them again, to further classify in 2D classes and repeat the procedure until a more accurate volume was achieved. Unfortunately, due to the small number of movies recorded and the low number of tetrameric particles extracted the quality of this refinement is poor (figure 63).

Grid preparation, screening and data collection on Titan Kryos

ComQF+thinC R 2/2, Au_300 mesh carbon coated grids were cleaned and charged using the Model 1070 Nano-Clean from Fischione Instruments available at the integrated structural biology (IBS) platform at IGBMC. Sample deposition was performed using the Vitrobot system present on the IBS platform, 3 μ L of sample were deposited at different concentrations (0.5 and 0.7 mg/ml). Vitrobot parameters were set as follow:

- Temperature 5°C
- Humidity 95-100 %
- Deposition time 30 s
- Blotting Force 5
- Blotting Time 2 s

After sample deposition, grids were flash frozen in liquid ethane and stored in liquid nitrogen. Not clipped grids were transfer then to Dubochet Center of Imaging (DCI) in Lausanne where a first screening to check sample and ice quality was performed on Glacios (figure 64).

All the frozen grids were screened and several micrographs per grid recorded in order to select the best condition among the available pull. A grid containing chicken tetramers at concentration of 0.5 mg/ml was selected and subsequently mounted on the Titan Kryos I at DCI. Data were collected with the following relevant for data processing parameters:

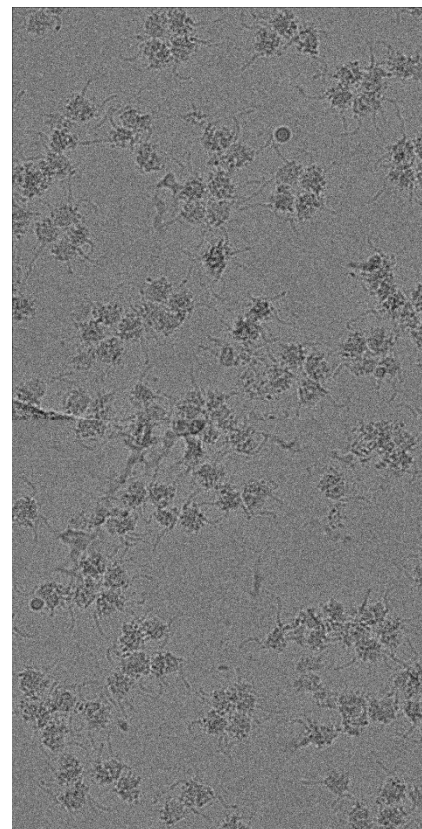


Figure 64 Micrographs collected on Glacios at DCI. Tetrameric assemblies are well spread on micrograph. Little amount of 80S ribosomes is present.

- Accelerating voltage: 300 kV
- Spherical aberration: 2.7 mm
- Pixel size: 0.927 Å
- Total exposure: $20 \frac{e}{\text{Å}^2}$
- Tilting 30° from movie 23264

The on-the-fly data processing showed a certain degree of preferential orientation, to avoid any further problem during data processing 30° tilted series have been collected from exposure 23264 to final.

Data Processing data collected on Titan Kryos DCI

Data processing have been performed in different ways. Following the example of the previous dataset the images have been imported, motion corrected and the contrast transfer function calculated per every image. Blob picking and particle extraction were firstly performed on a portion of collected micrographs and several rounds of 2D classification carried out. The 2D classes obtained from this step were then used as a template to re-pick particles from the totality of micrographs for further 2D classification (figure 65). Providing similar templates to the ab-initio reconstruction

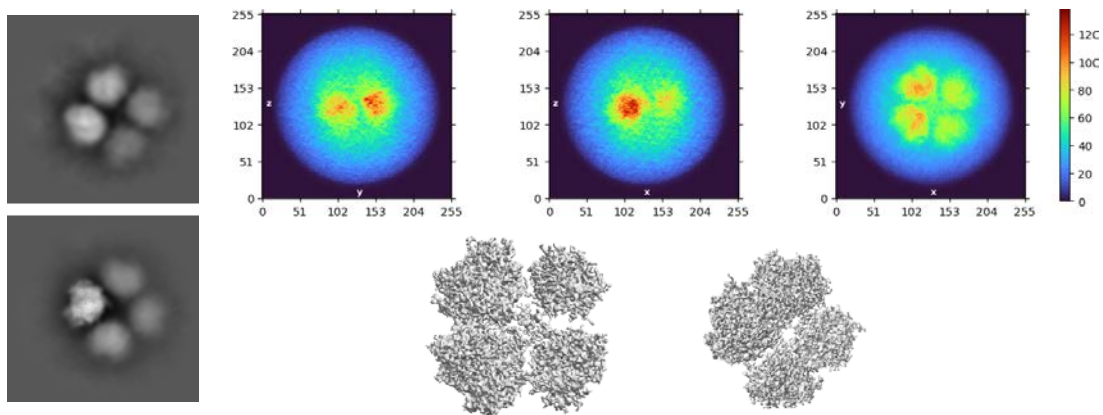


Figure 65 Volume determination procedure . a) 2D classification after Motion Correction and CTF calculation shows bidimensional particles clustered according to their similarities. b) The 2D classification is narrowed down using prior knowledge on the complex composition.

algorithm showed a different behavior in this particular dataset: every attempt to obtain an ab-initio trustable model using a high number of particles failed. The algorithm carrying the ab-initio calculation converged after every run to one single subunit of the tetrameric complex, making the workflow previously implemented completely inapplicable. The strategy has then changed, small parts of the dataset were processed

and 2D classes showing planar tetrameric assemblies used to perform the ab-initio reconstruction (figure 65). The outcome of this process showed that it was possible to obtain a volume with similar features as the one obtained with the previous dataset (figure 63) . The volume obtained has been then refined first against the particles that generated this particular volume, then against all particles belonging to that class 2D giving the result shown in figure 66 . This volume has been used to repick particles from micrographs in order to obtain a better reconstruction on which refine them. A sort of “ab-initio volume refinement” was implemented. Particles were re-picked, re-extracted, re-classified in 2D classes and narrowed according the criteria stated above,

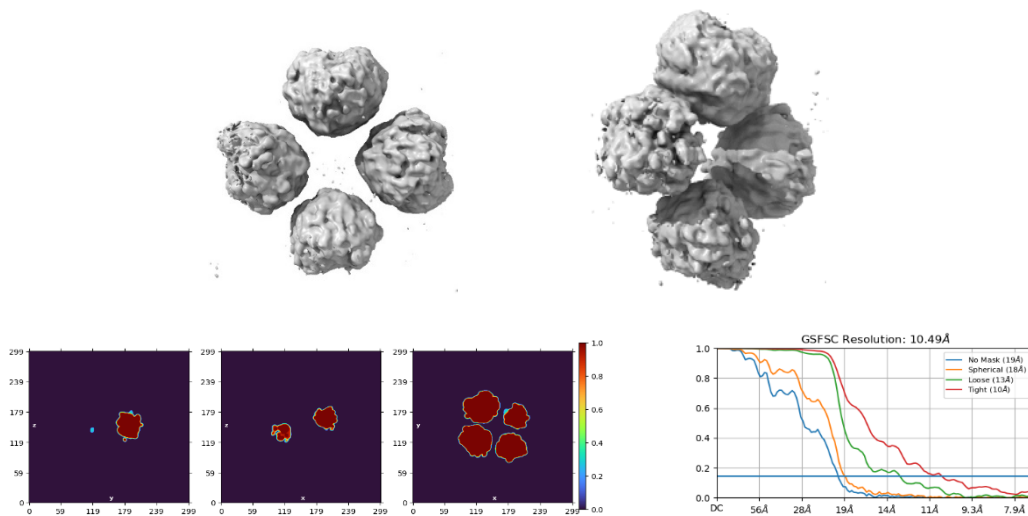


Figure 66 First attempt of chick ribosome tetramers reconstruction. a) Tetramers’ refined volume. b) Mask generated during homogeneous refinement. c) Fourier Shell Correlation, the golden number of 0.143 for FSC has been hit at 10.5 Å resolution

only manifestly tetrameric particles were included in the ab-initio calculation. Several approaches have been applied, yielding to the discovery of the optimal number of particles to be included in the ab-initio job. This search fruitfully opened the way to a more precise tetramers reconstruction. The issue of “one-particle-focus” has not been solved. It is indeed explainable with the alignment process that has to deal with bigger displacement due to the bigger physical dimensions. Particles belonging to only one bidimensional class were selected the result suggest that is possible to solve the full complex at least at medium resolution. The reconstruction obtained from tetrameric 2D classes shows a certain level of density aberration. Respectively three, seven and twelve thousand for each ab initio reconstruction asking to generate three separate ab

initio classes (figure 66). Volumes obtained from the ab-initio reconstruction were inspected in Chimera-X where the threshold for signal to noise was set at the same level for every reconstruction as shown in figure 68. Notably, the quality of the reconstruction has a double behavior. The higher the number of particles included in the volume calculation, the more defined one of the 80S ribosomes forming the tetramers became. On the other end, the more particles were added to the reconstruction the more the deviation from the tetrameric behavior was evident.

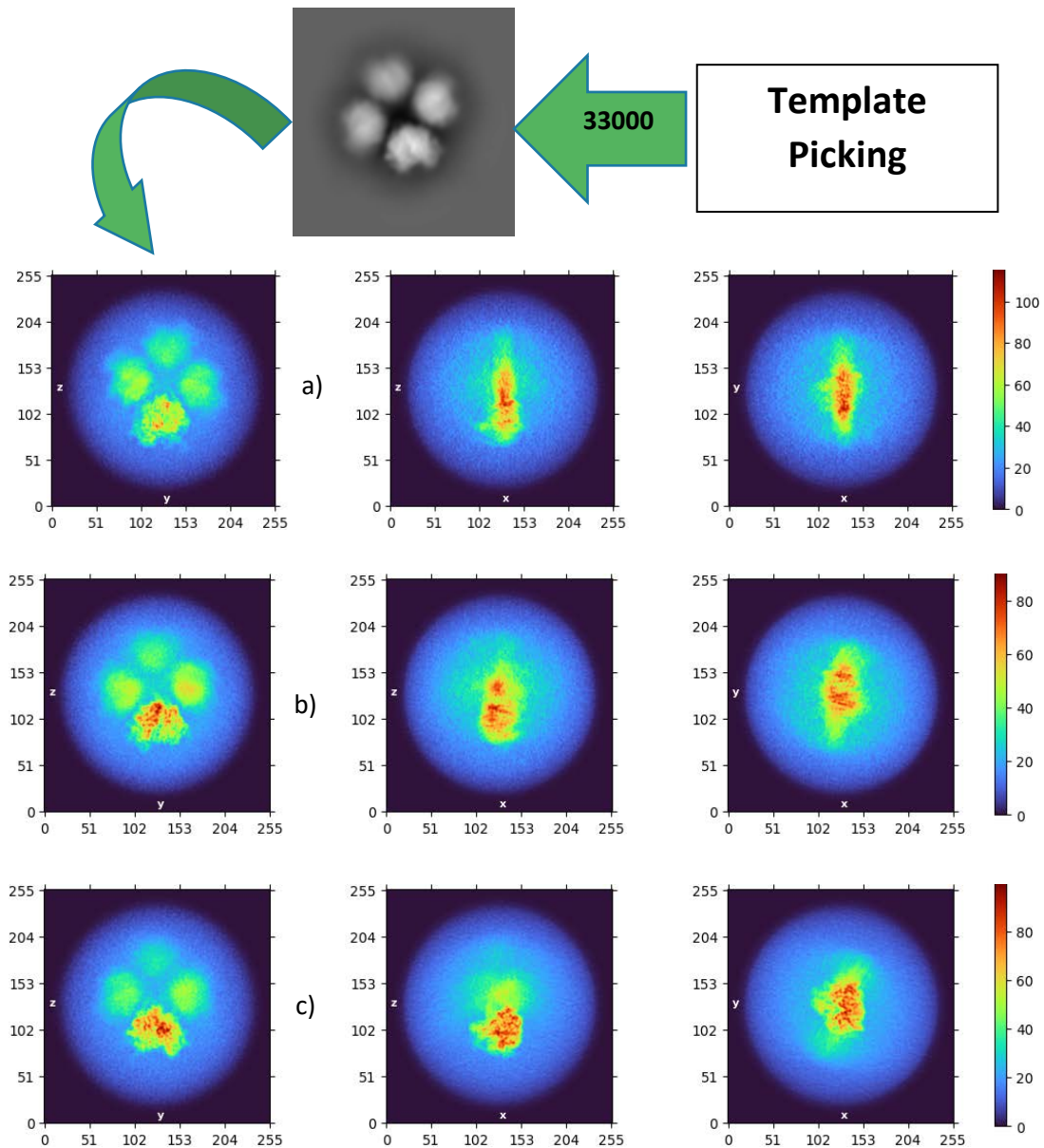


Figure 67 Ab initio reconstruction behaviour as a function of particle number. a) orthogonal projections of the volume reconstructed with 3000 particles, the warmer the colour palette turns the higher is the precision in reconstruction. b) bidimensional slices of the volume obtained with 7000 particles in the ab-initio calculations, the 80S ribosome on the bottom is better reconstructed to the detriment of the whole volume. c) orthogonal slices of the three-dimensional volume reconstructed with 10000 particles, the behaviour observed before persists as the particle number increases.

According to the goal of having the most representative of the three-dimensional arrangement of tetramers, the ab-initio model obtained with the lower number of particles was used for refinement (figure 69). The refinement was performed against all particles selected from which the first tetrameric class that generated the volume was previously extracted. The solution obtained has the features of the ribosomal tetrameric assembly. The map shows a full 80S ribosome surrounded by four blobs showing feature common to the well resolved subunit.

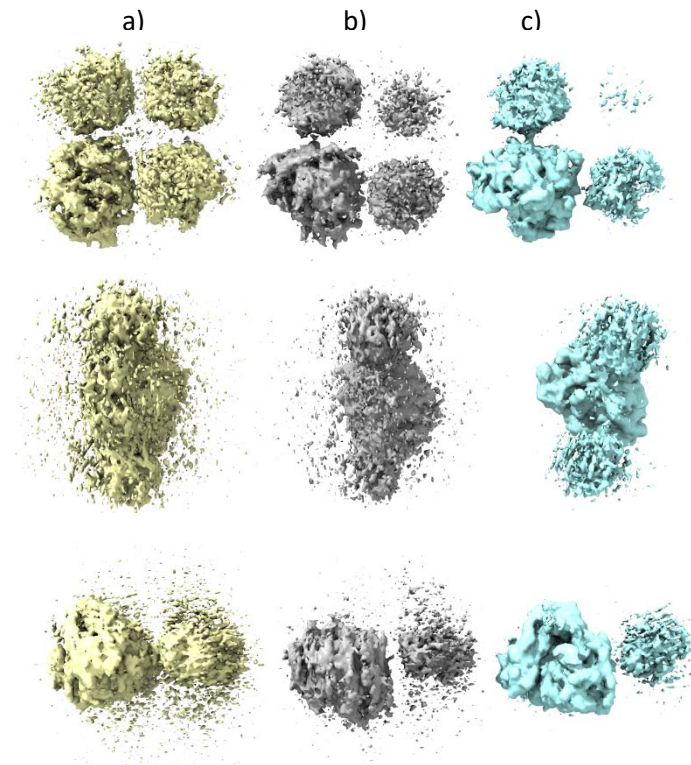


Figure 68 Ab initio reconstructed volumes. Three different ab initio volumes showed from different angles and obtained from the particles belonging to the 2D class shown in figure 6. a) In yellow three different orientation of the volume obtained from the class upper-mentioned limiting the number of particles included in the reconstruction to 3000. One of the particles is more defined than its neighbours. b) In grey representative orientations of the volume obtained from the class upper-mentioned limiting the number of particles included in the reconstruction to 3000. One of the particles is more defined than its neighbours. All volumes are shown at $\sigma = 5$

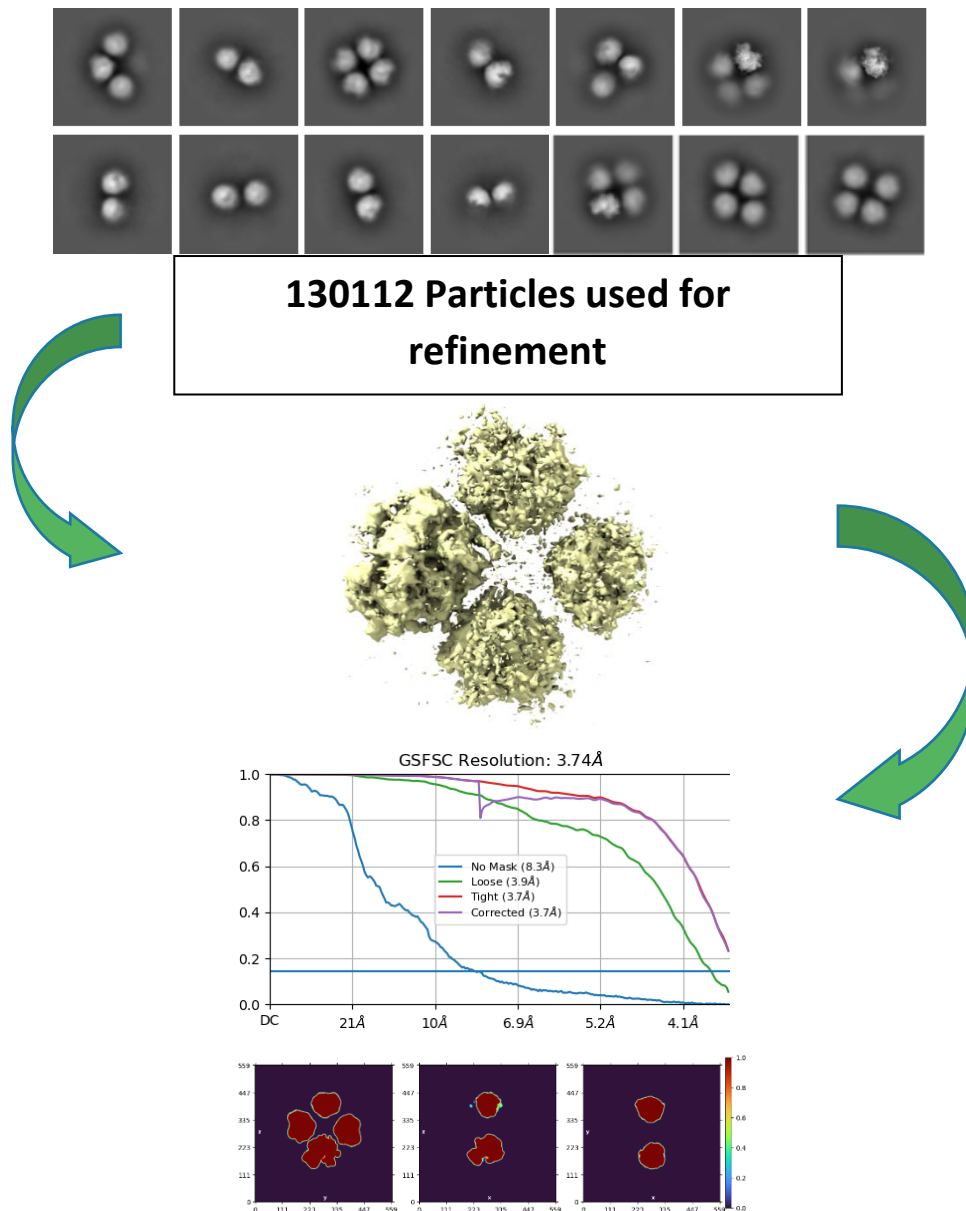


Figure 69 Tetramers homogeneous refinement workflow. a) Particles belonging to the 2D classes were re-extracted with twice cropped box sizes allowing a reconstruction at higher resolution. b) 130112 particles refinement against the volume reconstructed with 3k particles. c) Fourier Shell Correlation and mask, the golden number of 0.146 for FSC has not been hit, meaning the resolution limit is higher. Computational limitations did not allow the refinement with fully uncropped box size.

The solution previously calculated raised another methodological question: Is it possible to extract the single subunits of the tetrameric assemblies and refine them separately to obtain a reliable final volume? To address this issue, particles were re-picked using the templates generated with the refined volume previously obtained. The 2D classification job was performed with the re-centering option ON and with the aid of a circular mask of 1120 Å, with the same dimensions as the box used to extract particles. The number of classes was then narrowed as previously done and the ab initio reconstruction started. As expected the result of ab-initio reconstruction showed a single 80S ribosome with residual density its proximity as visible in figure 72. As done before the volume was refined against all particle in the 2D classes selection, allowing the visualization one of the 80S ribosomes constituting the complex. The resolution reached (Fourier Shell Correlation) is higher than the one achieved in case of tetrameric assemblies, furthermore the visual evaluation of the map showed a different quality for the obtained volume. Particles were refined against the volume in figure 72. The nature itself of homogeneous refinement does not allow to have a clear answer about the overall composition of ribosome tetramers. One of the cryo-spark blocks is specifically designed to address questions about the intrinsic variability of the particles used to obtain a certain reconstruction (Punjani et al., 2017). Particles and the calculated masks of monomers from tetramer picking were given as input to 3D-Var showing no variability in the given particles (figure 70). The same job has been performed on the final volume obtained from tetrameric aggregates, particles and mask of monomers underwent to the three-dimensional variability evaluation showing no significant displacement from one cluster of three-dimensional particles. This computational evidence supports the hypothesis of tetramers composed by ribosomes in the same conformation.

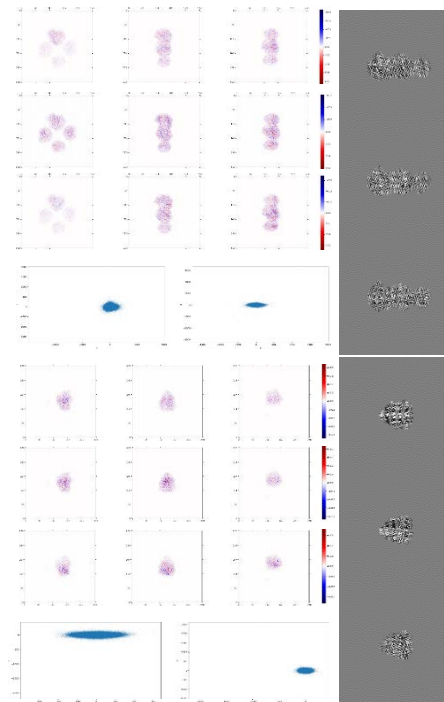


Figure 70 3D Variability results for tetramers and monomers extracted from tetramers.

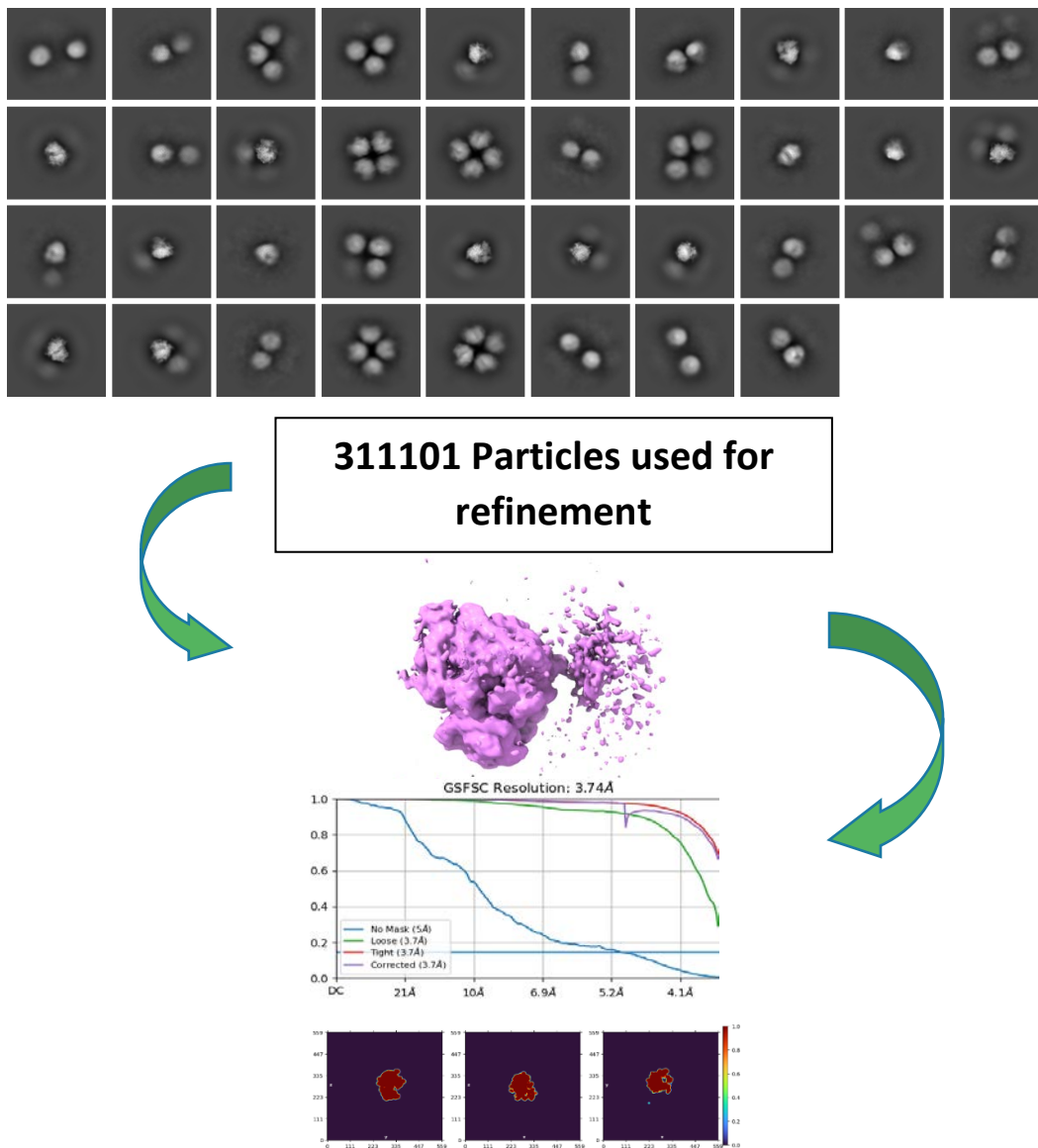


Figure 71 80S monomer isolated from tetramers homogeneous refinement workflow. a) Particles belonging to the 2D classes were re-extracted with a box size of 1120 Å cropped down to 560 Å. b) 311102 particles refinement against the volume reconstructed with all particles. c) Fourier Shell Correlation and obtained mask. The 0.143 limit for FSC has not been hit, meaning the resolution limit is higher. Computational limitations did not allow the refinement with fully uncropped box size.

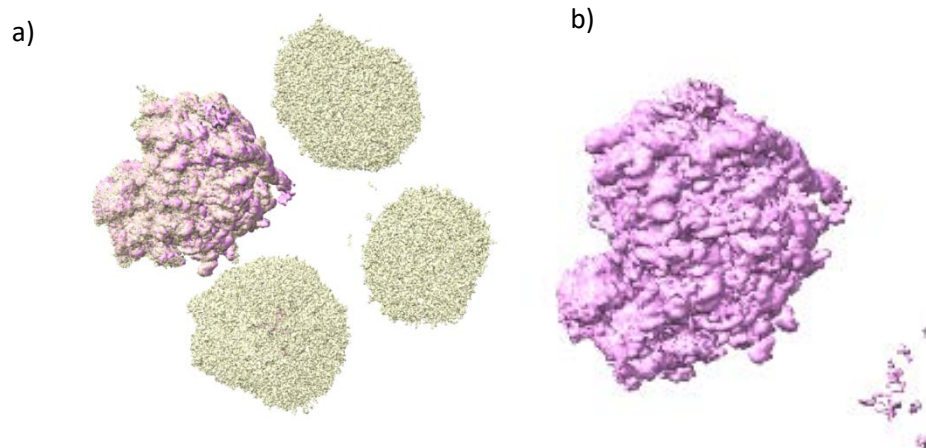


Figure 72 Cryo-EM reconstructions of tetramers and monomer from tetramers. a) Cryo-EM attempt of reconstruction of chick ribosome tetramers, the unclear blobs belong to neighbour ribosomes. b) Cryo-EM reconstruction of a monomer computationally extracted from tetramers.

Preliminary Results and Perspectives

The ribosome tetramers from chick embryos have been purified and characterized. All the biochemical assays performed showed a peak with an approximate Svedberg coefficient of 170S as shown in figure 57. The ribosomal RNA and protein composition have been assessed and the results are reported in figure 58. Furthermore, the protein composition of our sample has been inspected using mass spectrometry techniques. The analysis of mass spectrometry data revealed the presence of all ribosomal proteins present in the dataset used for comparison. Nevertheless, not all expected ribosomal proteins have been detected, this fact is linked to the incomplete nature of the dataset used for the analysis. In addition, the comparison between the mass spectrometry performed both on tetramer and monosome peaks revealed a slightly different protein composition (not shown). Different freezing conditions were screened allowing us to obtain several grids from which two main datasets have been collected and processed as described. Throughout the data processing steps, a certain level of preferential orientation of the particles has been observed. Interestingly this preferential orientation affects only the tetrameric complex and not the particles that compose it. This peculiarity allowed us to obtain a volume that reasonably represents one part of the bigger complex analyzed. The drawback of the approach adopted during data processing is that no information about the full arrangement of the complex can

be retrieved from our micrographs. The analysis of the obtained volume showed several interesting features in the 80S monomers isolated computationally from the tetrameric assembly. From the early publications from Morimoto (Morimoto et al., 1972a, 1972b), the absence of nascent polypeptide chain was postulated and experimentally proven by the absence of any radioactivity in the tetramers fraction during experiments with radioactively labeled Leucine. The reconstruction obtained shows the absence of any polypeptide chain in the ribosomal exit tunnel (figure 73 d). In the past authors proposed that puromycin did not have any effect on tetramerization because the nascent chain had already been released from ribosomes before tetramerization, making the action of puromycin irrelevant. The absence of nascent chain in tetramers suggests the additional step of releasing 80S monomers from actively translating polysomes (Morimoto et al., 1972a). The movement of the L1 stalk

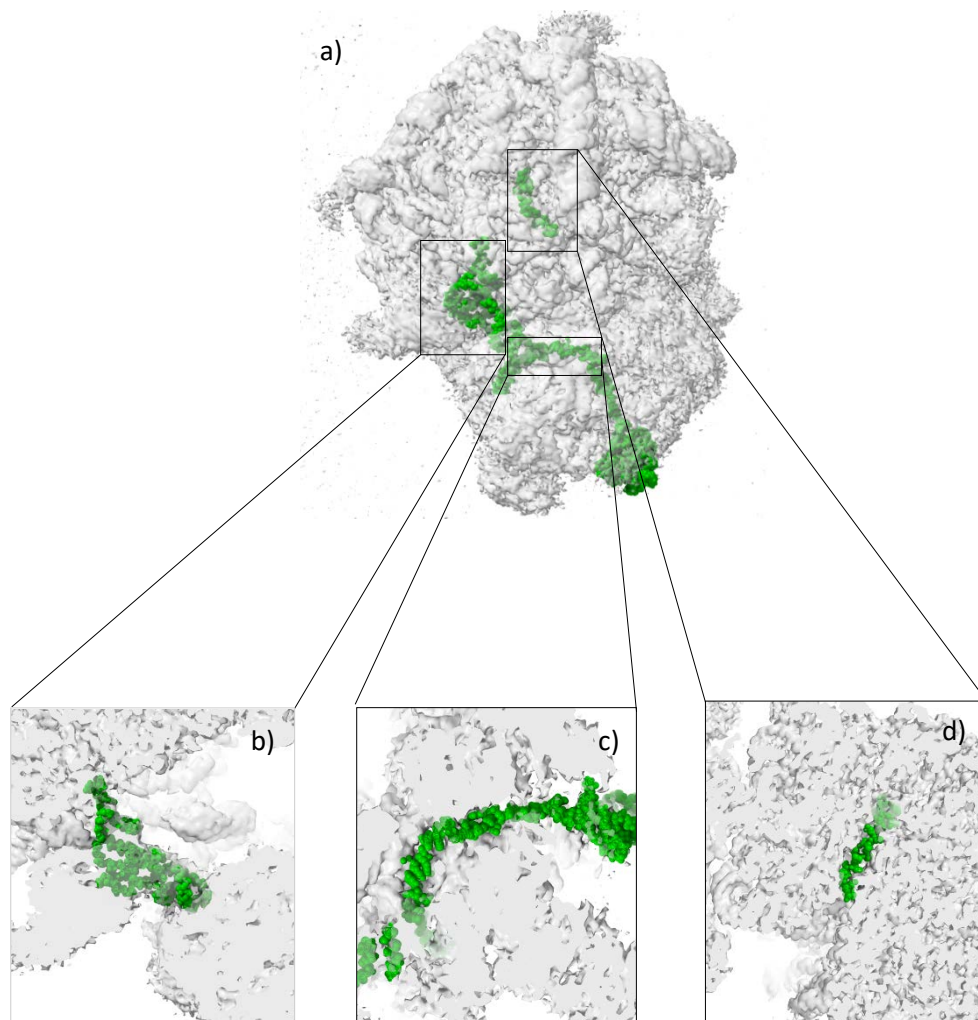


Figure 73 80S Ribosome isolated from the tetramer assembly. a) Cryo-EM reconstruction of the 80S monomer from chick ribosome tetramers. b) E-site tRNA surrounded by its density within its binding site, the unmodelled density represents the L stalk c) mRNA path within the ribosome, no density contours the superimposed mRNA molecule d) peptide exit tunnel within the large ribosomal subunit, no density contours the nascent polypeptide chain.

suggested the presence of E-site t-RNA. A closer look to the exit site revealed the presence the deacyl-tRNA within the pocket (figure 73 b). The molecule looks in a complete translocated state and ready to leave the ribosome. It is important to notice that the experiments conducted during the 60' and 70' showed how the glutarimide inhibitor cycloheximide impaired the formation of tetramers in vivo (Morimoto et al., 1972a). Nowadays we know where and how this molecule binds on the 80S ribosome and with the knowledge about its inhibition mechanism we can try to discuss what is the reason of this phenomenon. Despite the fact that E-site tRNA is often a contaminant in ribosome purification, its presence in our 80S ribosome might not be just a case. As previously discussed, cycloheximide binds within the binding pocket of eukaryotic ribosomes blocking the translocation step. If the tetramerization process needs the E-site tRNA in its binding pocket, then the inhibition of this phenomena upon cycloheximide treatment is not surprising. This inhibitor is also known to lead to polysome accumulation (Schneider-Poetsch et al., 2010), this might be related as well to the inhibition of ribosome complex formation. If monosomes are stalled on the mRNA by this molecule they will not be available to form tetramers in vivo. Along with the presence of E-site tRNA also the absence of any density in the mRNA path has been observed (figure 73 c). Tetramers, as reported in literature and suggested by our preliminary results, interacts via the large ribosomal subunit. This behavior is not often observed in systems where two or more ribosomes interact. In fact, the nature itself of the polysomal assembly implies a connection between the small ribosomal subunit, as shown in different works (Klaholz, 2021; Myasnikov et al., 2014). Furthermore, the reconstructions of colliding ribosomes revealed that in this case as well, the interaction is entirely happening between the two 40S subunits involved in the collision. In the prokaryotic kingdom, a variety of different hibernating ribosome complexes have been discovered during the last decade and even before. None of these present the features observed in tetramers, additionally the formation of these complexes is often mediated by stress response factors that stall ribosomes in order to protect them from the adverse environment. One exception to this “rule” is provided in a work where, after starvation, the presence of a peak corresponding to 110S was observed in the sucrose gradient profile of HeLa cells from mice (Krokowski et al., 2011). Cryo-electron microscopy of these specimens revealed that they are formed of ribosome dimers interacting via their big ribosomal subunit. The interaction was further explored revealing that the two subunits were linked via their P stalks. The preliminary reconstruction in our case does not allow us to propose any specific

interaction between 60S components. Nevertheless, the position assumed by the L1/L2 stalk might favor the interaction with the neighbor ribosome. The dimers reported in mice are observed in a degenerated system such HeLa mice cells. The experiments were performed under different conditions, including the nutriment deprivation. Author define this particular assembly as a hibernation state of the eukaryotic ribosome, making a parallel with the prokaryotic counterpart. In our case, a stress condition is present as well. Cold exposure has different effects on growing cells and different organisms react in different ways to this type of stimulus. Due to the high level of viability of chick embryos in early stages of development is not hard to think that this mechanism might have a physiological reason to happen. It is often observed in nature that eggs of different animals are exposed for short periods to cold stress, thus suggesting an evolutionary advantage in storing the translation machinery in the cell until more favorable conditions are encountered. Preliminary results and their interpretation have an enormous impact on the future directions of a project. Concerning the tetramer issue, several path can be thought and therefore taken. First of all, the necessity of better to achieve a broader angular distribution of particles is fundamental. Sample optimization is always the first approach to consider, especially in cases where the stability of the specimen can variate dramatically from purification to purification. The conformation and stability given by the ionic strength conditions in which the sample is frozen could in principle make another big step forward in the solution of the encountered problems. Characterization by analytical ultra-centrifugation under different experimental condition is surely a path to undertake to achieve a better quality. As already applied in other cases, cross-linking approaches can be beneficial in the stabilization of this enormous complex. Additionally, different approaches of processing can be explored, possibly yielding to more answers coming from these particular datasets. Finally, the striking progresses achieved in high resolution tomography are just too tempting to leave this path unexplored. Morimoto and colleagues suggested how this phenomenon was the proven proof that ribosome was crystallizable entities and a target for structure biology studies. On the other side, Barbieri and co-workers believed that there was something missing in the Morimoto model, as highlighted in different works. They suggested a more physiological explanation justifying the presence of this assemblies. The answer to this debate will not approach quickly. Is this really a mere thermodynamic process in which the parameter of temperature plays a solitary role or instead there is a more intricate explanation involving early developmental cellular processes?

Appendix

Tables

Haterumaimide Q	
Wavelength	1.0
Resolution range	206.3 - 3.16 (3.27 - 3.16)
Space group	P 1 21 1
Unit cell parameters	a=302.58 b=285.05 c=433.72 $\alpha=90$ $\beta=99$ $\gamma=90$
Unique reflections	1215791 (122248)
Multiplicity	2.0 (2.0)
Completeness (%)	98.28 (98.97)
Mean I/sigma(I)	7.29 (0.98)
R-merge	0.1243 (0.8491)
R-meas	0.1757 (1.201)
R-pim	0.1243 (0.8491)
CC1/2	0.994 (0.2)
CC*	0.998 (0.578)
Reflections used in refinement	1215426 (122123)
R-work	0.2255 (0.3650)
R-free	0.2481 (0.3659)
RMS(bonds)	0.006
RMS(angles)	1.17
Ramachandran favored (%)	99.82
Ramachandran allowed (%)	0.18
Ramachandran outliers (%)	0.00
Rotamer outliers (%)	0.03
Average B-factor	85.05

Haterumaimide J	
Wavelength Å	1.0
Resolution range	143.3 - 3.20(3.20 - 3.10)
Space group	P 1 21 1
Unit cell parameters	a=303.58 b=286.25 c=434.22 $\alpha=90$ $\beta=99$ $\gamma=90$
Unique reflections	1458793 (140700)
Multiplicity	2.0 (2.0)
Completeness (%)	99.18 (92.34)
Mean I/sigma(I)	6.03 (0.96)
R-merge	0.1277 (1.479)
R-meas	0.1805 (2.091)
R-pim	0.1277 (1.479)
CC1/2	0.963 (0.25)
CC*	0.991 (0.416)
Reflections used in refinement	1452846 (134984)
R-work	0.2489 (0.4065)
R-free	0.2954 (0.4121)
RMS(bonds)	0.009
RMS(angles)	1.89
Ramachandran favored (%)	97.84
Ramachandran allowed (%)	2.16
Ramachandran outliers (%)	0.00
Rotamer outliers (%)	0.96
Average B-factor	95.08

Fluorolissoclimide	
Wavelength Å	1.0
Resolution Range	158-3.0 (3.1-3.0)
Space group	P 1 21 1
Unit cell parameters	a=303.68 b=287.58 c=435.09 $\alpha=90$ $\beta=99$ $\gamma=90$
Unique reflections	1466777 (146354)
Multiplicity	2.0 (2.0)
Completeness (%)	99.96 (99.98)
Mean I/sigma(I)	9.36 (1.31)
R-merge	0.09408 (0.6538)
R-meas	0.1331 (0.9246)
R-pim	0.09408 (0.6538)
CC1/2	0.994 (0.37)
CC*	0.998 (0.735)
Reflections used in refinement	1466656 (146354)
R-work	0.2170 (0.3656)
R-free	0.2544 (0.3959)
RMS(bonds)	0.005
RMS(angles)	1.04
Ramachandran favored (%)	97.87
Ramachandran allowed (%)	1.16
Ramachandran outliers (%)	0.97
Rotamer outliers (%)	3.96
Average B-factor	90

DeoxyFluorolissoclimide	
Wavelength Å	1.0
Resolution Range	88 - 3.0 (3.11-3.0)
Space group	P 1 21 1
Unit cell parameters	a=301.85 b=284.58 c=432.74 $\alpha=90$ $\beta=99$ $\gamma=90$
Unique reflections	1434384 (141718)
Multiplicity	2.0 (2.0)
Completeness (%)	99.83 (98.95)
Mean I/sigma(I)	4.50 (0.83)
R-merge	0.1473 (1.203)
R-meas	0.2083 (1.701)
R-pim	0.1473 (1.203)
CC1/2	0.903 (0.124)
CC*	0.974 (0.50)
Reflections used in refinement	1432598 (141718)
R-work	0.2194 (0.3555)
R-free	0.2691 (0.3960)
RMS(bonds)	0.011
RMS(angles)	1.82
Ramachandran favored (%)	97.96
Ramachandran allowed (%)	2.04
Ramachandran outliers (%)	0.00
Rotamer outliers (%)	4.11
Average B-factor	95.15

Methylisoclimide	
Wavelength Å	1.0
Resolution Range	143.9- 2.9 (3.0-2.9)
Space group	P 1 21 1
Unit cell parameters	a=303.8 b=287.52 c=435.84 $\alpha=90$ $\beta=99$ $\gamma=90$
Unique reflections	1616823 (159778)
Multiplicity	2.0 (2.0)
Completeness (%)	99.29 (98.50)
Mean I/sigma(I)	12.30 (1.08)
R-merge	0.06411 (0.7581)
R-meas	0.09067 (1.072)
R-pim	0.06411 (0.7581)
CC1/2	0.975 (0.364)
CC*	0.994 (0.731)
Reflections used in refinement	1615436 (159778)
R-work	0.2125 (0.3777)
R-free	0.2441 (0.4327)
RMS(bonds)	0.005
RMS(angles)	1.13
Ramachandran favored (%)	99.61
Ramachandran allowed (%)	0.39
Ramachandran outliers (%)	0.00
Rotamer outliers (%)	4.79
Average B-factor	85.89

Bromolissoclimide	
Wavelength Å	1.0
Resolution range	98.96- 2.9 (3.0-2.9)
Space group	P 1 21 1
Unit cell parameters	a=302.09 b=285.96 c=433.31 $\alpha=90$ $\beta=99$ $\gamma=90$
Unique reflections	1597545 (159778)
Multiplicity	2.0 (2.0)
Completeness (%)	99.79 (98.50)
Mean I/sigma(I)	12.30 (1.33)
R-merge	0.06711 (0.7581)
R-meas	0.08267 (1.072)
R-pim	0.05411 (0.7581)
CC1/2	0.9642 (0.364)
CC*	0.992 (0.731)
Reflections used in refinement	1597545 (159778)
R-work	0.2235 (0.3777)
R-free	0.2670 (0.4327)
RMS(bonds)	0.009
RMS(angles)	1.60
Ramachandran favored (%)	99.68
Ramachandran allowed (%)	0.29
Ramachandran outliers (%)	0.02
Rotamer outliers (%)	4.79
Average B-factor	90.89

Gladiostatine	
Wavelength Å	1.0
Resolution range	171.9- 3.4 (3.5-3.4)
Space group	P 1 21 1
Unit cell parameters	a=303.8 b=287.52 c=435.84 $\alpha=90$ $\beta=99$ $\gamma=90$
Unique reflections	1927035 (159778)
Multiplicity	2.0 (2.0)
Completeness (%)	96.29 (98.50)
Mean I/sigma(I)	9.30 (0.8)
R-merge	0.06411 (0.7581)
R-meas	0.09067 (1.072)
R-pim	0.06411 (0.7581)
CC1/2	0.967 (0.264)
CC*	0.988 (0.731)
Reflections used in refinement	1615436 (159778)
R-work	0.2165 (0.4277)
R-free	0.2841 (0.4302)
RMS(bonds)	0.03
RMS(angles)	3.500
Ramachandran favored (%)	96.6
Ramachandran allowed (%)	2.6
Ramachandran outliers (%)	0.8
Rotamer outliers (%)	0.019
Average B-factor	110.89

Bibliography

- A, Y., 2005. Antibiotics targeting ribosomes: resistance, selectivity, synergism and cellular regulation. *Annual review of biochemistry* 74. <https://doi.org/10.1146/annurev.biochem.74.082803.133130>
- Afonine, P.V., Moriarty, N.W., Mustyakimov, M., Sobolev, O.V., Terwilliger, T.C., Turk, D., Urzhumtsev, A., Adams, P.D., 2015. FEM: feature-enhanced map. *Acta Cryst D* 71, 646–666. <https://doi.org/10.1107/S1399004714028132>
- Ahmad, M.U.D., Fish, A., Molenaar, J., Sreeramulu, S., Richter, C., Altincekic, N., Schwalbe, H., Wienk, H., Perrakis, A., 2021. Nano-Differential Scanning Fluorimetry for Screening in Fragment-based Lead Discovery. *J Vis Exp*. <https://doi.org/10.3791/62469>
- Aitken, C.E., Lorsch, J.R., 2012. A mechanistic overview of translation initiation in eukaryotes. *Nat Struct Mol Biol* 19, 568–576. <https://doi.org/10.1038/nsmb.2303>
- Alharazneh, A., Luk, L., Huth, M., Monfared, A., Steyger, P.S., Cheng, A.G., Ricci, A.J., 2011. Functional hair cell mechanotransducer channels are required for aminoglycoside ototoxicity. *PLoS One* 6, e22347. <https://doi.org/10.1371/journal.pone.0022347>
- Alkalaeva, E.Z., Pisarev, A.V., Frolova, L.Y., Kisselev, L.L., Pestova, T.V., 2006. In vitro reconstitution of eukaryotic translation reveals cooperativity between release factors eRF1 and eRF3. *Cell* 125, 1125–1136. <https://doi.org/10.1016/j.cell.2006.04.035>
- Arenz, S., Wilson, D.N., 2016. Bacterial Protein Synthesis as a Target for Antibiotic Inhibition. *Cold Spring Harb Perspect Med* 6, a025361. <https://doi.org/10.1101/cshperspect.a025361>
- Barbacid, M., Fresno, M., Vazquez, D., 1975. INHIBITORS OF POLYPEPTIDE ELONGATION ON YEAST POLYSOMES. *J. Antibiot.* 28, 453–462. <https://doi.org/10.7164/antibiotics.28.453>
- Barbieri, M., 1979. Ribosome crystallization in homogenates and cell extracts of chick embryos. *J Supramol Struct* 10, 349–357. <https://doi.org/10.1002/jss.400100306>
- Barbieri, M., 1974. The primitive ribosome model. *Journal of Theoretical Biology* 47, 269–280. [https://doi.org/10.1016/0022-5193\(74\)90197-0](https://doi.org/10.1016/0022-5193(74)90197-0)
- Behrmann, E., Loerke, J., Budkevich, T.V., Yamamoto, K., Schmidt, A., Penczek, P.A., Vos, M.R., Bürger, J., Mielke, T., Scheerer, P., Spahn, C.M.T., 2015. Structural snapshots of actively translating human ribosomes. *Cell* 161, 845–857. <https://doi.org/10.1016/j.cell.2015.03.052>
- Benedetto Tiz, D., Bagnoli, L., Rosati, O., Marini, F., Sancineto, L., Santi, C., 2022. New Halogen-Containing Drugs Approved by FDA in 2021: An Overview on Their Syntheses and Pharmaceutical Use. *Molecules* 27, 1643. <https://doi.org/10.3390/molecules27051643>
- Ben-Shem, A., Garreau de Loubresse, N., Melnikov, S., Jenner, L., Yusupova, G., Yusupov, M., 2011. The structure of the eukaryotic ribosome at 3.0 Å resolution. *Science* 334, 1524–1529. <https://doi.org/10.1126/science.1212642>
- Bertram, G., Bell, H.A., Ritchie, D.W., Fullerton, G., Stansfield, I., 2000. Terminating eukaryote translation: domain 1 of release factor eRF1 functions in stop codon recognition. *RNA* 6, 1236–1247. <https://doi.org/10.1017/s1355838200000777>
- Bhattacharya, A., Chowdhury, A., Chaudhury, K., Shukla, P.C., 2021. Proprotein convertase subtilisin/kexin type 9 (PCSK9): A potential multifaceted player in cancer. *Biochim Biophys Acta Rev Cancer* 1876, 188581. <https://doi.org/10.1016/j.bbcan.2021.188581>
- Biard, J.-F., Malochet-grivois, C., Roussakis, C., Cotelle, P., Hénichart, J.-P., Débitus, C., Verbist, J.-F., 1994. Lissoclimides, Cytotoxic Diterpenes from *Lissoclinum voeltzkowi* Michaelsen. *Natural Product Letters* 4, 43–50. <https://doi.org/10.1080/10575639408043890>
- Blair, J.M.A., Webber, M.A., Baylay, A.J., Ogbolu, D.O., Piddock, L.J.V., 2015. Molecular mechanisms of antibiotic resistance. *Nat Rev Microbiol* 13, 42–51. <https://doi.org/10.1038/nrmicro3380>
- Borovinskaya, M.A., Pai, R.D., Zhang, W., Schuwirth, B.S., Holton, J.M., Hirokawa, G., Kaji, H., Kaji, A., Cate, J.H.D., 2007. Structural basis for aminoglycoside inhibition of bacterial ribosome recycling. *Nat Struct Mol Biol* 14, 727–732. <https://doi.org/10.1038/nsmb1271>
- Bose, T., Fridkin, G., Davidovich, C., Krupkin, M., Dinger, N., Falkovich, A.H., Peleg, Y., Agmon, I., Bashan, A., Yonath, A., 2022. Origin of life: protoribosome forms peptide bonds and links RNA and protein dominated worlds. *Nucleic Acids Res* 50, 1815–1828. <https://doi.org/10.1093/nar/gkac052>

- Brönstrup, M., Sasse, F., 2020. Natural products targeting the elongation phase of eukaryotic protein biosynthesis. *Nat. Prod. Rep.* 37, 752–762. <https://doi.org/10.1039/D0NP00011F>
- Brunelli, M.A., Marini, M., Pettazoni, P., Bubola, G., 1977. Ribosomal crystallization in hypothermized chicken bone marrow. *Journal of Ultrastructure Research* 60, 140–147. [https://doi.org/10.1016/S0022-5320\(77\)80061-0](https://doi.org/10.1016/S0022-5320(77)80061-0)
- Bucher, K., Skogerson, L., 1976. Cryptopleurine--an inhibitor of translocation. *Biochemistry* 15, 4755–4759. <https://doi.org/10.1021/bi00667a001>
- Budkevich, T., Giesebrecht, J., Altman, R.B., Munro, J.B., Mielke, T., Nierhaus, K.H., Blanchard, S.C., Spahn, C.M.T., 2011. Structure and dynamics of the mammalian ribosomal pre-translocation complex. *Mol Cell* 44, 214–224. <https://doi.org/10.1016/j.molcel.2011.07.040>
- Burgers, L.D., Fürst, R., 2021. Natural products as drugs and tools for influencing core processes of eukaryotic mRNA translation. *Pharmacol Res* 170, 105535. <https://doi.org/10.1016/j.phrs.2021.105535>
- Byers, B., 1971. Chick embryo ribosome crystals: analysis of bonding and functional activity in vitro. *Proc Natl Acad Sci U S A* 68, 440–444. <https://doi.org/10.1073/pnas.68.2.440>
- Byers, B., 1966. Ribosome crystallization induced in chick embryo tissues by hypothermia. *J Cell Biol* 30, C1–6.
- Cabrita, M.T., Vale, C., Rauter, A.P., 2010. Halogenated compounds from marine algae. *Mar Drugs* 8, 2301–2317. <https://doi.org/10.3390/md8082301>
- Cannone, J.J., Subramanian, S., Schnare, M.N., Collett, J.R., D'Souza, L.M., Du, Y., Feng, B., Lin, N., Madabusi, L.V., Müller, K.M., Pande, N., Shang, Z., Yu, N., Gutell, R.R., 2002. The comparative RNA web (CRW) site: an online database of comparative sequence and structure information for ribosomal, intron, and other RNAs. *BMC Bioinformatics* 3, 2. <https://doi.org/10.1186/1471-2105-3-2>
- Carvalho, M.F., Oliveira, R.S., 2017. Natural production of fluorinated compounds and biotechnological prospects of the fluorinase enzyme. *Crit Rev Biotechnol* 37, 880–897. <https://doi.org/10.1080/07388551.2016.1267109>
- Casanas, A., Warshamanage, R., Finke, A.D., Panepucci, E., Olieric, V., Nöll, A., Tampé, R., Brandstetter, S., Förster, A., Mueller, M., Schulze-Briese, C., Bunk, O., Wang, M., 2016. EIGER detector: application in macromolecular crystallography. *Acta Cryst D* 72, 1036–1048. <https://doi.org/10.1107/S2059798316012304>
- Cate, J.H., Doudna, J.A., 1996. Metal-binding sites in the major groove of a large ribozyme domain. *Structure* 4, 1221–1229. [https://doi.org/10.1016/s0969-2126\(96\)00129-3](https://doi.org/10.1016/s0969-2126(96)00129-3)
- Chan, J., Khan, S.N., Harvey, I., Merrick, W., Pelletier, J., 2004. Eukaryotic protein synthesis inhibitors identified by comparison of cytotoxicity profiles. *RNA* 10, 528–543. <https://doi.org/10.1261/rna.5200204>
- Chen, D., Oezguen, N., Urvil, P., Ferguson, C., Dann, S.M., Savidge, T.C., 2016. Regulation of protein-ligand binding affinity by hydrogen bond pairing. *Science Advances* 2, e1501240. <https://doi.org/10.1126/sciadv.1501240>
- Chowdhury, H.M., Siddiqui, M.A., Kanneganti, S., Sharmin, N., Chowdhury, M.W., Nasim, M.T., 2018. Aminoglycoside-mediated promotion of translation readthrough occurs through a non-stochastic mechanism that competes with translation termination. *Hum Mol Genet* 27, 373–384. <https://doi.org/10.1093/hmg/ddx409>
- Cui, Y., Wu, L., Cao, R., Xu, H., Xia, J., Wang, Z.P., Ma, J., 2020. Antitumor functions and mechanisms of nitidine chloride in human cancers. *J Cancer* 11, 1250–1256. <https://doi.org/10.7150/jca.37890>
- Dabrowski, M., Bukowy-Bieryllo, Z., Zietkiewicz, E., 2018. Advances in therapeutic use of a drug-stimulated translational readthrough of premature termination codons. *Molecular Medicine* 24, 25. <https://doi.org/10.1186/s10020-018-0024-7>
- Damiani, E., Solorio, J.A., Doyle, A.P., Wallace, H.M., 2019. How reliable are in vitro IC50 values? Values vary with cytotoxicity assays in human glioblastoma cells. *Toxicol Lett* 302, 28–34. <https://doi.org/10.1016/j.toxlet.2018.12.004>
- Demeshkina, N., Jenner, L., Westhof, E., Yusupov, M., Yusupova, G., 2012. A new understanding of the decoding principle on the ribosome. *Nature* 484, 256–259. <https://doi.org/10.1038/nature10913>
- Dever, T.E., Dinman, J.D., Green, R., 2018. Translation Elongation and Recoding in Eukaryotes. *Cold Spring Harb Perspect Biol* 10, a032649. <https://doi.org/10.1101/cshperspect.a032649>

- Dinos, G., Wilson, D.N., Teraoka, Y., Szaflarski, W., Fucini, P., Kalpaxis, D., Nierhaus, K.H., 2004. Dissecting the ribosomal inhibition mechanisms of edeine and pactamycin: the universally conserved residues G693 and C795 regulate P-site RNA binding. *Mol Cell* 13, 113–124. [https://doi.org/10.1016/s1097-2765\(04\)00002-4](https://doi.org/10.1016/s1097-2765(04)00002-4)
- Djumagulov, M., Demeshkina, N., Jenner, L., Rozov, A., Yusupov, M., Yusupova, G., 2021. Accuracy mechanism of eukaryotic ribosome translocation. *Nature* 600, 543–546. <https://doi.org/10.1038/s41586-021-04131-9>
- Dmitriev, S.E., Vladimirov, D.O., Lashkevich, K.A., 2020. A Quick Guide to Small-Molecule Inhibitors of Eukaryotic Protein Synthesis. *Biochemistry (Mosc)* 85, 1389–1421. <https://doi.org/10.1134/S0006297920110097>
- Dn, E., Hf, N., 2011. mRNA translocation occurs during the second step of ribosomal intersubunit rotation. *Nature structural & molecular biology* 18. <https://doi.org/10.1038/nsmb.2011>
- Dölz, H., Vázquez, D., Jiménez, A., 1982. Quantitation of the specific interaction of [14a-3H]cryptopleurine with 80S and 40S ribosomal species from the yeast *Saccharomyces cerevisiae*. *Biochemistry* 21, 3181–3187. <https://doi.org/10.1021/bi00256a023>
- Emsley, P., Cowtan, K., 2004. Coot: model-building tools for molecular graphics. *Acta Cryst D* 60, 2126–2132. <https://doi.org/10.1107/S0907444904019158>
- Evidente, A., Kireev, A.S., Jenkins, A.R., Romero, A.E., Steelant, W.F.A., Van Slambrouck, S., Kornienko, A., 2009. Biological evaluation of structurally diverse amaryllidaceae alkaloids and their synthetic derivatives: discovery of novel leads for anticancer drug design. *Planta Med* 75, 501–507. <https://doi.org/10.1055/s-0029-1185340>
- Feldman, M.B., Terry, D.S., Altman, R.B., Blanchard, S.C., 2010. Aminoglycoside activity observed on single pre-translocation ribosome complexes. *Nat Chem Biol* 6, 54–62. <https://doi.org/10.1038/nchembio.274>
- Fuchs, S., Hsieh, L.T., Saarberg, W., Erdelmeier, C.A.J., Wichelhaus, T.A., Schaefer, L., Koch, E., Fürst, R., 2015. *Haemanthus coccineus* extract and its main bioactive component narciclasine display profound anti-inflammatory activities in vitro and in vivo. *J Cell Mol Med* 19, 1021–1032. <https://doi.org/10.1111/jcmm.12493>
- Fujii, K., Susanto, T.T., Saurabh, S., Barna, M., 2018. Decoding the Function of Expansion Segments in Ribosomes. *Molecular Cell* 72, 1013-1020.e6. <https://doi.org/10.1016/j.molcel.2018.11.023>
- Fürst, R., 2016. Narciclasine - an Amaryllidaceae Alkaloid with Potent Antitumor and Anti-Inflammatory Properties. *Planta Med* 82, 1389–1394. <https://doi.org/10.1055/s-0042-115034>
- Gao, Y.-G., Selmer, M., Dunham, C.M., Weixlbaumer, A., Kelley, A.C., Ramakrishnan, V., 2009. The structure of the ribosome with elongation factor G trapped in the posttranslocational state. *Science* 326, 694–699. <https://doi.org/10.1126/science.1179709>
- Garreau de Loubresse, N., Prokhorova, I., Holtkamp, W., Rodnina, M.V., Yusupova, G., Yusupov, M., 2014. Structural basis for the inhibition of the eukaryotic ribosome. *Nature* 513, 517–522. <https://doi.org/10.1038/nature13737>
- Gilles, A., Frechin, L., Natchiar, K., Biondani, G., Loeffelholz, O. von, Holvec, S., Malaval, J.-L., Winum, J.-Y., Klaholz, B.P., Peyron, J.-F., 2020. Targeting the Human 80S Ribosome in Cancer: From Structure to Function and Drug Design for Innovative Adjuvant Therapeutic Strategies. *Cells* 9, E629. <https://doi.org/10.3390/cells9030629>
- Gonzalez, I.L., Gorski, J.L., Campen, T.J., Dorney, D.J., Erickson, J.M., Sylvester, J.E., Schmickel, R.D., 1985. Variation among human 28S ribosomal RNA genes. *Proc Natl Acad Sci U S A* 82, 7666–7670. <https://doi.org/10.1073/pnas.82.22.7666>
- Gonzalez, I.L., Sylvester, J.E., Schmickel, R.D., 1988. Human 28S ribosomal RNA sequence heterogeneity. *Nucleic Acids Res* 16, 10213–10224.
- Gopalakrishnan, R., Matta, H., Choi, S., Chaudhary, P.M., 2020. Narciclasine, an isocarbostryril alkaloid, has preferential activity against primary effusion lymphoma. *Sci Rep* 10, 5712. <https://doi.org/10.1038/s41598-020-62690-9>
- Gürel, G., Blaha, G., Steitz, T.A., Moore, P.B., 2009. Structures of triacetyloleandomycin and mycalamide A bind to the large ribosomal subunit of *Haloarcula marismortui*. *Antimicrob Agents Chemother* 53, 5010–5014. <https://doi.org/10.1128/AAC.00817-09>

- Gutierrez, E., Shin, B.-S., Woolstenhulme, C.J., Kim, J.-R., Saini, P., Buskirk, A.R., Dever, T.E., 2013. eIF5A promotes translation of polyproline motifs. *Mol Cell* 51, 35–45. <https://doi.org/10.1016/j.molcel.2013.04.021>
- Hellen, C.U.T., 2018. Translation Termination and Ribosome Recycling in Eukaryotes. *Cold Spring Harb Perspect Biol* 10, a032656. <https://doi.org/10.1101/cshperspect.a032656>
- Jackson, R.J., Hellen, C.U.T., Pestova, T.V., 2012. Termination and post-termination events in eukaryotic translation. *Adv Protein Chem Struct Biol* 86, 45–93. <https://doi.org/10.1016/B978-0-12-386497-0.00002-5>
- Julien, S.G., Kim, S.-Y., Brunmeir, R., Sinnakannu, J.R., Ge, X., Li, H., Ma, W., Yaligar, J., Kn, B.P., Velan, S.S., Röder, P.V., Zhang, Q., Sim, C.K., Wu, J., Garcia-Miralles, M., Pouladi, M.A., Xie, W., McFarlane, C., Han, W., Xu, F., 2017. Narciclasine attenuates diet-induced obesity by promoting oxidative metabolism in skeletal muscle. *PLoS Biol* 15, e1002597. <https://doi.org/10.1371/journal.pbio.1002597>
- Kabsch, W., 2010. XDS. *Acta Cryst D* 66, 125–132. <https://doi.org/10.1107/S0907444909047337>
- Kantarjian, H.M., O'Brien, S., Cortes, J., 2013. Homoharringtonine/Omacetaxine Mepesuccinate: The Long and Winding Road to Food and Drug Administration Approval. *Clin Lymphoma Myeloma Leuk* 13, 530–533. <https://doi.org/10.1016/j.clml.2013.03.017>
- Keeling, K.M., Xue, X., Gunn, G., Bedwell, D.M., 2014. Therapeutics based on stop codon readthrough. *Annu Rev Genomics Hum Genet* 15, 371–394. <https://doi.org/10.1146/annurev-genom-091212-153527>
- Kim, J., Park, Y., Chun, Y.S., Cha, J.W., Kwon, H.C., Oh, M.S., Chung, S., Yang, H.O., 2015. Effect of Lycoris chejuensis and Its Active Components on Experimental Models of Alzheimer's Disease. *J Agric Food Chem* 63, 6979–6988. <https://doi.org/10.1021/acs.jafc.5b00889>
- Klaholz, B.P., 2021. Studying the Structural Organization of Polyribosomes with Alexander S. Spirin. *Biochemistry (Mosc)* 86, 1053–1059. <https://doi.org/10.1134/S0006297921090030>
- Klein, D.J., Moore, P.B., Steitz, T.A., 2004. The contribution of metal ions to the structural stability of the large ribosomal subunit. *RNA* 10, 1366–1379. <https://doi.org/10.1261/rna.7390804>
- Klinge, S., Voigts-Hoffmann, F., Leibundgut, M., Arpagaus, S., Ban, N., 2011. Crystal structure of the eukaryotic 60S ribosomal subunit in complex with initiation factor 6. *Science* 334, 941–948. <https://doi.org/10.1126/science.1211204>
- Knight, J.R.P., Garland, G., Pöyry, T., Mead, E., Vlahov, N., Sfakianos, A., Grosso, S., De-Lima-Hedayioglou, F., Mallucci, G.R., von der Haar, T., Smales, C.M., Sansom, O.J., Willis, A.E., 2020. Control of translation elongation in health and disease. *Dis Model Mech* 13, dmm043208. <https://doi.org/10.1242/dmm.043208>
- Könst, Z.A., Szklarski, A.R., Pellegrino, S., Michalak, S.E., Meyer, M., Zanette, C., Cencic, R., Nam, S., Voora, V.K., Horne, D.A., Pelletier, J., Mobley, D.L., Yusupova, G., Yusupov, M., Vanderwal, C.D., 2017. Synthesis facilitates an understanding of the structural basis for translation inhibition by the lissoclimides. *Nat Chem* 9, 1140–1149. <https://doi.org/10.1038/nchem.2800>
- Kozak, M., Shatkin, A.J., 1978. Migration of 40 S ribosomal subunits on messenger RNA in the presence of edeine. *J Biol Chem* 253, 6568–6577.
- Krause, K.M., Serio, A.W., Kane, T.R., Connolly, L.E., 2016. Aminoglycosides: An Overview. *Cold Spring Harb Perspect Med* 6, a027029. <https://doi.org/10.1101/cshperspect.a027029>
- Krokowski, D., Gaccioli, F., Majumder, M., Mullins, M.R., Yuan, C.L., Papadopoulou, B., Merrick, W.C., Komar, A.A., Taylor, D., Hatzoglou, M., 2011. Characterization of hibernating ribosomes in mammalian cells. *Cell Cycle* 10, 2691–2702. <https://doi.org/10.4161/cc.10.16.16844>
- Kuroda, D., Gray, J.J., 2016. Shape complementarity and hydrogen bond preferences in protein–protein interfaces: implications for antibody modeling and protein–protein docking. *Bioinformatics* 32, 2451–2456. <https://doi.org/10.1093/bioinformatics/btw197>
- Lefranc, F., Sauvage, S., Van Goietsenoven, G., Mégalizzi, V., Lamoral-Theys, D., Debeir, O., Spiegl-Kreinecker, S., Berger, W., Mathieu, V., Decaestecker, C., Kiss, R., 2009. Narciclasine, a plant growth modulator, activates Rho and stress fibers in glioblastoma cells. *Mol Cancer Ther* 8, 1739–1750. <https://doi.org/10.1158/1535-7163.MCT-08-0932>
- Leprivier, G., Remke, M., Rotblat, B., Dubuc, A., Mateo, A.-R.F., Kool, M., Agnihotri, S., El-Naggar, A., Yu, B., Prakash Somasekharan, S., Faubert, B., Bridon, G., Tognon, C.E., Mathers, J., Thomas, R., Li, A., Barokas, A., Kwok, B., Bowden, M., Smith, S., Wu, X., Korshunov, A., Hielscher, T., Northcott, P.A.,

- Galpin, J.D., Ahern, C.A., Wang, Y., McCabe, M.G., Collins, V.P., Jones, R.G., Pollak, M., Delattre, O., Gleave, M.E., Jan, E., Pfister, S.M., Proud, C.G., Derry, W.B., Taylor, M.D., Sorensen, P.H., 2013. The eEF2 Kinase Confers Resistance to Nutrient Deprivation by Blocking Translation Elongation. *Cell* 153, 1064–1079. <https://doi.org/10.1016/j.cell.2013.04.055>
- Li, W., Chang, S.T.-L., Ward, F.R., Cate, J.H.D., 2020. Selective inhibition of human translation termination by a drug-like compound. *Nat Commun* 11, 4941. <https://doi.org/10.1038/s41467-020-18765-2>
- Li, W., Ward, F.R., McClure, K.F., Chang, S.T.-L., Montabana, E., Liras, S., Dullea, R.G., Cate, J.H.D., 2019. Structural basis for selective stalling of human ribosome nascent chain complexes by a drug-like molecule. *Nat Struct Mol Biol* 26, 501–509. <https://doi.org/10.1038/s41594-019-0236-8>
- Liao, Y., Chu, H.-P., Hu, Z., Merkin, J.J., Chen, J., Liu, Z., Degenhardt, K., White, E., Ryazanov, A.G., 2016. Paradoxical Roles of Elongation Factor-2 Kinase in Stem Cell Survival. *J Biol Chem* 291, 19545–19557. <https://doi.org/10.1074/jbc.M116.724856>
- Liaud, N., Horlbeck, M.A., Gilbert, L.A., Gjoni, K., Weissman, J.S., Cate, J.H.D., 2019. Cellular response to small molecules that selectively stall protein synthesis by the ribosome. *PLOS Genetics* 15, e1008057. <https://doi.org/10.1371/journal.pgen.1008057>
- Liebschner, D., Afonine, P.V., Baker, M.L., Bunkóczi, G., Chen, V.B., Croll, T.I., Hintze, B., Hung, L.-W., Jain, S., McCoy, A.J., Moriarty, N.W., Oeffner, R.D., Poon, B.K., Prisant, M.G., Read, R.J., Richardson, J.S., Richardson, D.C., Sammito, M.D., Sobolev, O.V., Stockwell, D.H., Terwilliger, T.C., Urzhumtsev, A.G., Videau, L.L., Williams, C.J., Adams, P.D., 2019. Macromolecular structure determination using X-rays, neutrons and electrons: recent developments in Phenix. *Acta Cryst D* 75, 861–877. <https://doi.org/10.1107/S2059798319011471>
- Lin, J., Zhou, D., Steitz, T.A., Polikanov, Y.S., Gagnon, M.G., 2018. Ribosome-Targeting Antibiotics: Modes of Action, Mechanisms of Resistance, and Implications for Drug Design. *Annu Rev Biochem* 87, 451–478. <https://doi.org/10.1146/annurev-biochem-062917-011942>
- Ma, X.M., Blenis, J., 2009. Molecular mechanisms of mTOR-mediated translational control. *Nat Rev Mol Cell Biol* 10, 307–318. <https://doi.org/10.1038/nrm2672>
- Mantsyzov, A.B., Ivanova, E.V., Birdsall, B., Alkalaeva, E.Z., Kryuchkova, P.N., Kelly, G., Frolova, L.Y., Polshakov, V.I., 2010. NMR solution structure and function of the C-terminal domain of eukaryotic class 1 polypeptide chain release factor. *FEBS J* 277, 2611–2627. <https://doi.org/10.1111/j.1742-464X.2010.07672.x>
- Mattis, V.B., Rai, R., Wang, J., Chang, C.-W.T., Coady, T., Lorson, C.L., 2006. Novel aminoglycosides increase SMN levels in spinal muscular atrophy fibroblasts. *Hum Genet* 120, 589–601. <https://doi.org/10.1007/s00439-006-0245-7>
- Mattis, V.B., Tom Chang, C.-W., Lorson, C.L., 2012. Analysis of a read-through promoting compound in a severe mouse model of spinal muscular atrophy. *Neuroscience Letters* 525, 72–75. <https://doi.org/10.1016/j.neulet.2012.07.024>
- Matzov, D., Bashan, A., Yonath, A., 2017. A Bright Future for Antibiotics? *Annu Rev Biochem* 86, 567–583. <https://doi.org/10.1146/annurev-biochem-061516-044617>
- Mazumdar, P., Choudhury, D., 2022. Study of the alkyl- π interaction between methane and few substituted pyrimidine systems using DFT, AIM and NBO calculations. *Computational and Theoretical Chemistry* 1208, 113560. <https://doi.org/10.1016/j.comptc.2021.113560>
- McClary, B., Zinshteyn, B., Meyer, M., Jouanneau, M., Pellegrino, S., Yusupova, G., Schuller, A., Reyes, J.C.P., Lu, J., Guo, Z., Ayinde, S., Luo, C., Dang, Y., Romo, D., Yusupov, M., Green, R., Liu, J.O., 2017. Inhibition of eukaryotic translation by the antitumor natural product Agelastatin A. *Cell Chem Biol* 24, 605–613.e5. <https://doi.org/10.1016/j.chembiol.2017.04.006>
- Mei, H., Han, J., Fustero, S., Medio-Simon, M., Sedgwick, D.M., Santi, C., Ruzziconi, R., Soloshonok, V.A., 2019. Fluorine-Containing Drugs Approved by the FDA in 2018. *Chemistry* 25, 11797–11819. <https://doi.org/10.1002/chem.201901840>
- Melnikov, S., Ben-Shem, A., Garreau de Loubresse, N., Jenner, L., Yusupova, G., Yusupov, M., 2012. One core, two shells: bacterial and eukaryotic ribosomes. *Nat Struct Mol Biol* 19, 560–567. <https://doi.org/10.1038/nsmb.2313>
- Melnikov, S., Mailliot, J., Rigger, L., Neuner, S., Shin, B.-S., Yusupova, G., Dever, T.E., Micura, R., Yusupov, M., 2016. Molecular insights into protein synthesis with proline residues. *EMBO Rep* 17, 1776–1784. <https://doi.org/10.15252/embr.201642943>

- Michalak, S.E., Nam, S., Kwon, D.M., Horne, D.A., Vanderwal, C.D., 2019. A Chlorine-Atom-Controlled Terminal-Epoxy-Initiated Bicyclization Cascade Enables a Synthesis of the Potent Cytotoxins Haterumaimides J and K. *J. Am. Chem. Soc.* 141, 9202–9206. <https://doi.org/10.1021/jacs.9b04702>
- Milligan, R.A., Unwin, P.N.T., 1986. Location of exit channel for nascent protein in 80S ribosome. *Nature* 319, 693–695. <https://doi.org/10.1038/319693a0>
- Moazed, D., Noller, H.F., 1989. Intermediate states in the movement of transfer RNA in the ribosome. *Nature* 342, 142–148. <https://doi.org/10.1038/342142a0>
- Morimoto, T., Blobel, G., Sabatini, D.D., 1972a. Ribosome crystallization in chicken embryos. I. Isolation, characterization, and in vitro activity of ribosome tetramers. *J Cell Biol* 52, 338–354. <https://doi.org/10.1083/jcb.52.2.338>
- Morimoto, T., Blobel, G., Sabatini, D.D., 1972b. Ribosome crystallization in chicken embryos. II. Conditions for the formation of ribosome tetramers in vitro. *J Cell Biol* 52, 355–366. <https://doi.org/10.1083/jcb.52.2.355>
- Murray, J., Savva, C.G., Shin, B.-S., Dever, T.E., Ramakrishnan, V., Fernández, I.S., 2016. Structural characterization of ribosome recruitment and translocation by type IV IRES. *Elife* 5, e13567. <https://doi.org/10.7554/eLife.13567>
- Myasnikov, A.G., Afonina, Z.A., Ménétret, J.-F., Shirokov, V.A., Spirin, A.S., Klaholz, B.P., 2014. The molecular structure of the left-handed supra-molecular helix of eukaryotic polyribosomes. *Nat Commun* 5, 5294. <https://doi.org/10.1038/ncomms6294>
- Myasnikov, A.G., Kundhavai Natchiar, S., Nebout, M., Hazemann, I., Imbert, V., Khatter, H., Peyron, J.-F., Klaholz, B.P., 2016. Structure–function insights reveal the human ribosome as a cancer target for antibiotics. *Nat Commun* 7, 12856. <https://doi.org/10.1038/ncomms12856>
- Nair, J.J., van Staden, J., 2021. Cytotoxic Agents in the Minor Alkaloid Groups of the Amaryllidaceae. *Planta Med* 87, 916–936. <https://doi.org/10.1055/a-1380-1888>
- Nakou, I.T., Jenner, M., Dashti, Y., Romero-Canelón, I., Masschelein, J., Mahenthiralingam, E., Challis, G.L., 2020. Genomics-Driven Discovery of a Novel Glutarimide Antibiotic from *Burkholderia gladioli* Reveals an Unusual Polyketide Synthase Chain Release Mechanism. *Angew Chem Int Ed Engl* 59, 23145–23153. <https://doi.org/10.1002/anie.202009007>
- Nano differential scanning fluorimetry (nanoDSF / nDSF) [WWW Document], n.d. URL <https://www.coriolis-pharma.com/analytical-services/higher-order-structure-analysis/nano-differential-scanning-fluorimetry-nanodsf> (accessed 10.29.22).
- Neumann, C.S., Fujimori, D.G., Walsh, C.T., 2008. Halogenation Strategies In Natural Product Biosynthesis. *Chemistry & Biology* 15, 99–109. <https://doi.org/10.1016/j.chembiol.2008.01.006>
- Nissen, P., Ippolito, J.A., Ban, N., Moore, P.B., Steitz, T.A., 2001. RNA tertiary interactions in the large ribosomal subunit: The A-minor motif. *Proceedings of the National Academy of Sciences* 98, 4899–4903. <https://doi.org/10.1073/pnas.081082398>
- Ogle, J.M., Brodersen, D.E., Clemons, W.M., Tarry, M.J., Carter, A.P., Ramakrishnan, V., 2001. Recognition of cognate transfer RNA by the 30S ribosomal subunit. *Science* 292, 897–902. <https://doi.org/10.1126/science.1060612>
- Olsen, G.J., Woese, C.R., 1993. Ribosomal RNA: a key to phylogeny. *The FASEB Journal* 7, 113–123. <https://doi.org/10.1096/fasebj.7.1.8422957>
- Osterman, I.A., Wieland, M., Maviza, T.P., Lashkevich, K.A., Lukianov, D.A., Komarova, E.S., Zakalyukina, Y.V., Buschauer, R., Shiriaev, D.I., Leyn, S.A., Zlamal, J.E., Biryukov, M.V., Skvortsov, D.A., Tashlitsky, V.N., Polshakov, V.I., Cheng, J., Polikanov, Y.S., Bogdanov, A.A., Osterman, A.L., Dmitriev, S.E., Beckmann, R., Dontsova, O.A., Wilson, D.N., Sergiev, P.V., 2020. Tetracenomycin X inhibits translation by binding within the ribosomal exit tunnel. *Nat Chem Biol* 16, 1071–1077. <https://doi.org/10.1038/s41589-020-0578-x>
- Pak, B.S., Supantanapong, N., Vanderwal, C.D., 2021. The Recurring Roles of Chlorine in Synthetic and Biological Studies of the Lissoclimides. *Acc Chem Res* 54, 1131–1142. <https://doi.org/10.1021/acs.accounts.0c00866>
- Panigrahi, S.K., Desiraju, G.R., 2007. Strong and weak hydrogen bonds in drug-DNA complexes: A statistical analysis. *J Biosci* 32, 677–691. <https://doi.org/10.1007/s12038-007-0068-2>
- Pellegrino, S., Meyer, M., Könst, Z.A., Holm, M., Voora, V.K., Kashinskaya, D., Zanette, C., Mobley, D.L., Yusupova, G., Vanderwal, C.D., Blanchard, S.C., Yusupov, M., 2019. Understanding the role of

- intermolecular interactions between lissoclimides and the eukaryotic ribosome. *Nucleic Acids Res* 47, 3223–3232. <https://doi.org/10.1093/nar/gkz053>
- Pellegrino, S., Meyer, M., Zorbas, C., Bouchta, S.A., Saraf, K., Pelly, S.C., Yusupova, G., Evidente, A., Mathieu, V., Kornienko, A., Lafontaine, D.L.J., Yusupov, M., 2018. The Amaryllidaceae Alkaloid Haemanthamine Binds the Eukaryotic Ribosome to Repress Cancer Cell Growth. *Structure* 26, 416–425.e4. <https://doi.org/10.1016/j.str.2018.01.009>
- Perras, F.A., Marion, D., Boisbouvier, J., Bryce, D.L., Plevin, M.J., 2017. Observation of CH \cdots π Interactions between Methyl and Carbonyl Groups in Proteins. *Angewandte Chemie International Edition* 56, 7564–7567. <https://doi.org/10.1002/anie.201702626>
- Petersen, D.N., Hawkins, J., Ruangsiriluk, W., Stevens, K.A., Maguire, B.A., O’Connell, T.N., Rocke, B.N., Boehm, M., Ruggeri, R.B., Rolph, T., Hepworth, D., Loria, P.M., Carpino, P.A., 2016. A Small-Molecule Anti-secretagogue of PCSK9 Targets the 80S Ribosome to Inhibit PCSK9 Protein Translation. *Cell Chem Biol* 23, 1362–1371. <https://doi.org/10.1016/j.chembiol.2016.08.016>
- Pioletti, M., Schlünzen, F., Harms, J., Zarivach, R., Glühmann, M., Avila, H., Bashan, A., Bartels, H., Auerbach, T., Jacobi, C., Hartsch, T., Yonath, A., Franceschi, F., 2001. Crystal structures of complexes of the small ribosomal subunit with tetracycline, edeine and IF3. *EMBO J* 20, 1829–1839. <https://doi.org/10.1093/emboj/20.8.1829>
- Popp, M.W., Maquat, L.E., 2018. Nonsense-mediated mRNA Decay and Cancer. *Current Opinion in Genetics & Development, Cancer genomics* 48, 44–50. <https://doi.org/10.1016/j.gde.2017.10.007>
- Powers, K.T., Stevenson-Jones, F., Yadav, S.K.N., Amthor, B., Bufton, J.C., Borucu, U., Shen, D., Becker, J.P., Lavysh, D., Hentze, M.W., Kulozik, A.E., Neu-Yilik, G., Schaffitzel, C., 2021. Blasticidin S inhibits mammalian translation and enhances production of protein encoded by nonsense mRNA. *Nucleic Acids Res* 49, 7665–7679. <https://doi.org/10.1093/nar/gkab532>
- Prokhorova, I., Altman, R.B., Djumagulov, M., Shrestha, J.P., Urzhumtsev, A., Ferguson, A., Chang, C.-W.T., Yusupov, M., Blanchard, S.C., Yusupova, G., 2017. Aminoglycoside interactions and impacts on the eukaryotic ribosome. *Proc Natl Acad Sci U S A* 114, E10899–E10908. <https://doi.org/10.1073/pnas.1715501114>
- Prokhorova, I.V., Akulich, K.A., Makeeva, D.S., Osterman, I.A., Skvortsov, D.A., Sergiev, P.V., Dontsova, O.A., Yusupova, G., Yusupov, M.M., Dmitriev, S.E., 2016. Amicoumacin A induces cancer cell death by targeting the eukaryotic ribosome. *Sci Rep* 6, 27720. <https://doi.org/10.1038/srep27720>
- Punjani, A., Rubinstein, J.L., Fleet, D.J., Brubaker, M.A., 2017. cryoSPARC: algorithms for rapid unsupervised cryo-EM structure determination. *Nat Methods* 14, 290–296. <https://doi.org/10.1038/nmeth.4169>
- Pyronnet, S., Imataka, H., Gingras, A.C., Fukunaga, R., Hunter, T., Sonenberg, N., 1999. Human eukaryotic translation initiation factor 4G (eIF4G) recruits mnk1 to phosphorylate eIF4E. *EMBO J* 18, 270–279. <https://doi.org/10.1093/emboj/18.1.270>
- Ramesh, M., Woolford, J.L., 2016. Eukaryote-specific rRNA expansion segments function in ribosome biogenesis. *RNA* 22, 1153–1162. <https://doi.org/10.1261/rna.056705.116>
- Ramrath, D.J.F., Lancaster, L., Sprink, T., Mielke, T., Loerke, J., Noller, H.F., Spahn, C.M.T., 2013. Visualization of two transfer RNAs trapped in transit during elongation factor G-mediated translocation. *Proc Natl Acad Sci U S A* 110, 20964–20969. <https://doi.org/10.1073/pnas.1320387110>
- Ratje, A.H., Loerke, J., Mikolajka, A., Brünner, M., Hildebrand, P.W., Starosta, A.L., Dönhöfer, A., Connell, S.R., Fucini, P., Mielke, T., Whitford, P.C., Onuchic, J.N., Yu, Y., Sanbonmatsu, K.Y., Hartmann, R.K., Penczek, P.A., Wilson, D.N., Spahn, C.M.T., 2010. Head swivel on the ribosome facilitates translocation by means of intra-subunit tRNA hybrid sites. *Nature* 468, 713–716. <https://doi.org/10.1038/nature09547>
- Ribas, J., Cubero, E., Luque, F.J., Orozco, M., 2002. Theoretical Study of Alkyl- π and Aryl- π Interactions. Reconciling Theory and Experiment. *J. Org. Chem.* 67, 7057–7065. <https://doi.org/10.1021/jo0201225>
- Robert, F., Gao, H.Q., Donia, M., Merrick, W.C., Hamann, M.T., Pelletier, J., 2006. Chlorolissoclimides: New inhibitors of eukaryotic protein synthesis. *RNA* 12, 717–725. <https://doi.org/10.1261/rna.2346806>
- Robichaud, N., Sonenberg, N., Ruggero, D., Schneider, R.J., 2019. Translational Control in Cancer. *Cold Spring Harb Perspect Biol* 11, a032896. <https://doi.org/10.1101/cshperspect.a032896>

- Roy, M., Liang, L., Xiao, X., Feng, P., Ye, M., Liu, J., 2018. Lycorine: A prospective natural lead for anticancer drug discovery. *Biomed Pharmacother* 107, 615–624. <https://doi.org/10.1016/j.biopha.2018.07.147>
- Rozov, A., Khusainov, I., El Omari, K., Duman, R., Mykhaylyk, V., Yusupov, M., Westhof, E., Wagner, A., Yusupova, G., 2019. Importance of potassium ions for ribosome structure and function revealed by long-wavelength X-ray diffraction. *Nat Commun* 10, 2519. <https://doi.org/10.1038/s41467-019-10409-4>
- Scheuermann, T.H., Brautigam, C.A., 2015. High-precision, automated integration of multiple isothermal titration calorimetric thermograms: new features of NITPIC. *Methods* 76, 87–98. <https://doi.org/10.1016/j.ymeth.2014.11.024>
- Schmeing, T.M., Ramakrishnan, V., 2009. What recent ribosome structures have revealed about the mechanism of translation. *Nature* 461, 1234–1242. <https://doi.org/10.1038/nature08403>
- Schmidt, C., Becker, T., Heuer, A., Braunger, K., Shanmuganathan, V., Pech, M., Berninghausen, O., Wilson, D.N., Beckmann, R., 2016. Structure of the hypusinylated eukaryotic translation factor eIF-5A bound to the ribosome. *Nucleic Acids Res* 44, 1944–1951. <https://doi.org/10.1093/nar/gkv1517>
- Schneider-Poetsch, T., Ju, J., Eyler, D.E., Dang, Y., Bhat, S., Merrick, W.C., Green, R., Shen, B., Liu, J.O., 2010. Inhibition of eukaryotic translation elongation by cycloheximide and lactimidomycin. *Nat Chem Biol* 6, 209–217. <https://doi.org/10.1038/nchembio.304>
- Shao, S., Murray, J., Brown, A., Taunton, J., Ramakrishnan, V., Hegde, R.S., 2016. Decoding Mammalian Ribosome-mRNA States by Translational GTPase Complexes. *Cell* 167, 1229–1240.e15. <https://doi.org/10.1016/j.cell.2016.10.046>
- Shin, B.-S., Katoh, T., Gutierrez, E., Kim, J.-R., Suga, H., Dever, T.E., 2017. Amino acid substrates impose polyamine, eIF5A, or hypusine requirement for peptide synthesis. *Nucleic Acids Res* 45, 8392–8402. <https://doi.org/10.1093/nar/gkx532>
- Silvera, D., Formenti, S.C., Schneider, R.J., 2010. Translational control in cancer. *Nat Rev Cancer* 10, 254–266. <https://doi.org/10.1038/nrc2824>
- Spahn, C.M.T., Gomez-Lorenzo, M.G., Grassucci, R.A., Jørgensen, R., Andersen, G.R., Beckmann, R., Penczek, P.A., Ballesta, J.P.G., Frank, J., 2004. Domain movements of elongation factor eEF2 and the eukaryotic 80S ribosome facilitate tRNA translocation. *EMBO J* 23, 1008–1019. <https://doi.org/10.1038/sj.emboj.7600102>
- Steitz, T.A., 2008. A structural understanding of the dynamic ribosome machine. *Nat Rev Mol Cell Biol* 9, 242–253. <https://doi.org/10.1038/nrm2352>
- Svetlov, M.S., Koller, T.O., Meydan, S., Shankar, V., Klepacki, D., Polacek, N., Guydosh, N.R., Vázquez-Laslop, N., Wilson, D.N., Mankin, A.S., 2021. Context-specific action of macrolide antibiotics on the eukaryotic ribosome. *Nat Commun* 12, 2803. <https://doi.org/10.1038/s41467-021-23068-1>
- Svidritskiy, E., Ling, C., Ermolenko, D.N., Korostelev, A.A., 2013. Blastidicin S inhibits translation by trapping deformed tRNA on the ribosome. *Proceedings of the National Academy of Sciences* 110, 12283–12288. <https://doi.org/10.1073/pnas.1304922110>
- Sweeney, R., Chen, L., Yao, M.C., 1994. An rRNA variable region has an evolutionarily conserved essential role despite sequence divergence. *Mol Cell Biol* 14, 4203–4215. <https://doi.org/10.1128/mcb.14.6.4203-4215.1994>
- Taylor, D.J., Nilsson, J., Merrill, A.R., Andersen, G.R., Nissen, P., Frank, J., 2007. Structures of modified eEF2 80S ribosome complexes reveal the role of GTP hydrolysis in translocation. *EMBO J* 26, 2421–2431. <https://doi.org/10.1038/sj.emboj.7601677>
- Trendowski, M., 2015. Recent Advances in the Development of Antineoplastic Agents Derived from Natural Products. *Drugs* 75, 1993–2016. <https://doi.org/10.1007/s40265-015-0489-4>
- Tsai, A., Uemura, S., Johansson, M., Puglisi, E.V., Marshall, R.A., Aitken, C.E., Korlach, J., Ehrenberg, M., Puglisi, J.D., 2013. The impact of aminoglycosides on the dynamics of translation elongation. *Cell Rep* 3, 497–508. <https://doi.org/10.1016/j.celrep.2013.01.027>
- Unwin, P.N., Taddei, C., 1977. Packing of ribosomes in crystals from the lizard *Lacerta sicula*. *J Mol Biol* 114, 491–506. [https://doi.org/10.1016/0022-2836\(77\)90174-7](https://doi.org/10.1016/0022-2836(77)90174-7)
- Vázquez-Laslop, N., Mankin, A.S., 2018. How Macrolide Antibiotics Work. *Trends Biochem Sci* 43, 668–684. <https://doi.org/10.1016/j.tibs.2018.06.011>

- Vitrobot | Cryo EM Sample Preparation - FR [WWW Document], n.d. URL
<https://www.thermofisher.com/fr/fr/home/electron-microscopy/products/sample-preparation-equipment-em/vitrobot-system.html> (accessed 10.30.22).
- Wagner, K.R., Hamed, S., Hadley, D.W., Gropman, A.L., Burstein, A.H., Escolar, D.M., Hoffman, E.P., Fischbeck, K.H., 2001. Gentamicin treatment of Duchenne and Becker muscular dystrophy due to nonsense mutations. *Ann Neurol* 49, 706–711.
- Wan, F., Anderson, D.E., Barnitz, R.A., Snow, A., Bidere, N., Zheng, L., Hegde, V., Lam, L.T., Staudt, L.M., Levens, D., Deutsch, W.A., Lenardo, M.J., 2007. Ribosomal protein S3: a KH domain subunit in NF-kappaB complexes that mediates selective gene regulation. *Cell* 131, 927–939.
<https://doi.org/10.1016/j.cell.2007.10.009>
- Warner, J.R., 1999. The economics of ribosome biosynthesis in yeast. *Trends Biochem Sci* 24, 437–440.
[https://doi.org/10.1016/s0968-0004\(99\)01460-7](https://doi.org/10.1016/s0968-0004(99)01460-7)
- Warner, J.R., McIntosh, K.B., 2009. How common are extraribosomal functions of ribosomal proteins? *Mol Cell* 34, 3–11. <https://doi.org/10.1016/j.molcel.2009.03.006>
- Waskiewicz, A.J., Flynn, A., Proud, C.G., Cooper, J.A., 1997. Mitogen-activated protein kinases activate the serine/threonine kinases Mnk1 and Mnk2. *EMBO J* 16, 1909–1920.
<https://doi.org/10.1093/emboj/16.8.1909>
- Weisser, M., Schäfer, T., Leibundgut, M., Böhringer, D., Aylett, C.H.S., Ban, N., 2017. Structural and Functional Insights into Human Re-initiation Complexes. *Mol Cell* 67, 447-456.e7.
<https://doi.org/10.1016/j.molcel.2017.06.032>
- Wen, J., Lord, H., Knutson, N., Wikström, M., 2020. Nano differential scanning fluorimetry for comparability studies of therapeutic proteins. *Analytical Biochemistry* 593, 113581.
<https://doi.org/10.1016/j.ab.2020.113581>
- Wool, I.G., 1996. Extraribosomal functions of ribosomal proteins. *Trends Biochem Sci* 21, 164–165.
- Yusupova, G., Pellegrino, S., Terrosu, S., Yusupov, M., 2021. Inhibition of the Eukaryotic 80S Ribosome as a Potential Anticancer Therapy: A Structural Perspective. *Cancers* 13.
<https://doi.org/10.3390/cancers13174392>
- Yusupova, G., Yusupov, M., 2017. Crystal structure of eukaryotic ribosome and its complexes with inhibitors. *Philos Trans R Soc Lond B Biol Sci* 372, 20160184.
<https://doi.org/10.1098/rstb.2016.0184>
- Yusupova, G., Yusupov, M., 2015. Ribosome biochemistry in crystal structure determination. *RNA* 21, 771–773. <https://doi.org/10.1261/rna.050039.115>
- Zander, U., Cianci, M., Foos, N., Silva, C.S., Mazzei, L., Zubieta, C., de Maria, A., Nanao, M.H., 2016. Merging of synchrotron serial crystallographic data by a genetic algorithm. *Acta Cryst D* 72, 1026–1035.
<https://doi.org/10.1107/S2059798316012079>
- Zgadza, Y., Kolosova, O., Stetsenko, A., Wu, C., Bruchlen, D., Usachev, K., Validov, S., Jenner, L., Rogachev, A., Yusupova, G., Sachs, M., Guskov, A., Yusupov, M., 2022. E-site drug specificity of the human pathogen *Candida albicans* ribosome. *Science Advances* 8, eabn1062.
<https://doi.org/10.1126/sciadv.abn1062>
- Zhao, H., Piszczek, G., Schuck, P., 2015. SEDPHAT – a platform for global ITC analysis and global multi-method analysis of molecular interactions. *Methods* 76, 137–148.
<https://doi.org/10.1016/j.ymeth.2014.11.012>

Résumé en français suivi des mots-clés en français

La synthèse des protéines est un processus vital dans la cellule et son principal acteur est le ribosome. Il lit le code génétique, sous forme d'ARNm, et synthétise les protéines au cours d'un processus appelé traduction. La traduction est régulée pour assurer une croissance cellulaire adéquate. En raison du rôle central joué par le ribosome, il n'est pas surprenant que l'altération de sa fonction puisse être incompatible avec la vie. Ces dernières années, de nombreux inhibiteurs eucaryotes ont été identifiés. Avec une machinerie de traduction inhibée, le cancer ainsi que les pathogènes eucaryotes ne sont pas en mesure de synthétiser des protéines, ce qui entraîne leur mort. L'approbation du premier inhibiteur du ribosome pour le traitement de la leucémie myéloïde chronique a souligné le potentiel du ribosome comme cible pour le développement de médicaments anticancéreux. De nombreux inhibiteurs eucaryotes sont d'origine naturelle. La chimie médicale a permis d'élargir les possibilités, en apportant des modifications aux molécules naturelles, en améliorant leur puissance et en diminuant leurs effets secondaires. Dans cet article, l'interaction de huit inhibiteurs de ribosomes différents est examinée au niveau moléculaire dans le cadre de leur application comme traitement anticancéreux.

Mots clés : Rayon X, Inhibition de la traduction, Découverte de médicaments, Halogènes

Résumé en anglais suivi des mots-clés en anglais

Protein synthesis is vital process in the cell and its main actor is the ribosome. It reads the genetic code, in the form of mRNA, synthesizing proteins during a process called translation. Translation is regulated to ensure proper cell growth. Because of the central role played by the ribosome, it is not surprising that alteration of its function can be incompatible with life. During the last years many eukaryotic inhibitors have been identified. With an inhibited translation machinery, cancer along with eukaryotic pathogens are not able to synthesize proteins, encountering death. The approval of the first ribosome inhibitor for the treatment of Chronic Myeloid Leukaemia underlined the potential of ribosome as a target for the development of anticancer drugs. Many eukaryotic inhibitors are of natural origin. Medical chemistry allowed to widen the possibilities, introducing changes on naturally occurring molecules, improving their potency and decreasing their side effects. Herein the interaction of eight different ribosome inhibitors is discussed at the molecular level in the frame of their application as anticancer treatment.

Keywords : X-ray, Translation inhibition, Drug Discovery, Halogens